6-1-2015

Variation of surface properties of ceramic and composite nanostructures and their measurements by a novel approach using perichromic dyes

Amr Mohamed Tayel

The American University in Cairo
School of Science and Engineering

Variation of Surface Properties of Ceramic and Composite Nanostructures and their Measurements by a Novel Approach using Perichromic Dyes

A Thesis submitted to
Chemistry Graduate Program

In partial fulfillment of the requirements for
Degree of Master of Science in Chemistry

By Amr Mohamed Taha Tayel
BSc of Pharmaceutical Sciences

Under the supervision of

Prof. Adham R. Ramadan
Prof. Omar Abou El Seoud

Spring 2015

The American University in Cairo

Variation of Surface Properties of Ceramic and Composite Nanostructures and their Measurements by a Novel Approach using Perichromic Dyes

A Thesis submitted by

Amr Mohamed Taha Tayel

To the Chemistry Graduate Program

Spring 2015

In partial fulfillment of the requirements for

Degree of Master of Science in Chemistry

Has been approved by

Thesis Committee Supervisor /Chair: Prof. Adham R. Ramadan

Affiliation: Department of Chemistry, The American University in Cairo

Thesis Co-advisor: Prof. Omar Abou El Seoud

Affiliation: Institute of Chemistry, University of São Paulo

Thesis Internal Examiner: Prof. Tarek Madkour

Affiliation: Department of Chemistry, The American University in Cairo

Thesis External Examiner: Prof. Maged Antonious

Affiliation: Department of Chemistry, Faculty of Science, Ain Shams University

Thesis Committee Moderator: Dr. Mayyada El Sayed

Affiliation: Department of Chemistry, The American University in Cairo

Program Director Date Dean Date

TO MY DEAR WIFE

ACKNOWLEDGEMENTS

It is with immense gratitude that I acknowledge the support and help of my advisor Professor Adham Ramadan. This thesis would not have been possible unless his endless guidance, patience and help. He has made available his support in a number of ways and I'm grateful for him in both academic and personal attributes. I consider it a privilege to have the opportunity to work with him and learn the fundamentals of scientific research. I believe there are no words that can express my sincere appreciation for every single word he said to me.

I owe my deepest gratitude to Professor Omar Abou El Seoud whose help and support made this thesis possible. Sharing his time, laboratory and resources made many hard times to pass smoothly. His students and colleagues at the University of São Paulo represent a key factor in finishing this work.

I would like to acknowledge the financial support of the American University in Cairo through the graduate student research grant, the laboratory instruction graduate fellowship and the study abroad support grant.

I would also like to express my sincere thanks to Dr. Nahed Yacoub and my laboratory colleagues. Their help and understanding were indispensable. I've learned so much from Dr Nahed and I'm really indebted to her.

Last but not least, I am endlessly grateful to my dear wife and children. Their unconditional love, prayers, support and patience over the last couple of years made everything possible. Rasha, Basmala, Mohamed and Rody, thank you.

List of Abbreviations

2D	Two dimensional
^{31}P MAS NMR	^{31}P magic angle spinning nuclear magnetic resonance
AO7	Acid orange-7
BET	Brunauer-Emmett- Teller
BJH	Barrett-Joyner-Halenda
BSEs	Back scattered electrons
CB	Conduction band
CV	Cyclic voltammetry
CVD	Chemical vapor deposition
DI	Deionized water
DLS	Dynamic light scattering
DMSO	Dimethyl sulfoxide
DRS-UV	UV-Visible diffuse reflectance spectra
DSSC	Dye-sensitized solar cells
DTBSB	*o,o'*-di-*tert*-butylstilbazolium betaine
E_g	Band gap energy
EIS	Electrochemical impedance spectroscopy
EMR	Electromagnetic radiation
FESEM	Field emission scanning electron microscopy
FTIR	Fourier transform infrared spectroscopy
FTO	Fluorinated Tin oxide
G	Graphene
GO	Graphene oxide
GO-TiO_2 NRCs	GO-TiO_2 nanorods composites
HOMO	Highest occupied molecular orbital
HPLC/MS	High performance liquid chromatography/mass spectrometry
HT	Hydrothermal
IRMS-TPD	Infrared--mass spectrometry- temperature programmed desorption
LBL	Layer by layer

LEI	Lower secondary electron detector
LPD	Liquid phase deposition
LUMO	Lowest unoccupied molecular orbital
MB	Methylene blue
MWCNTs	Multi-wall carbon nanotubes
N,V–TiO_2–G	Nitrogen and Vanadium co-doped TiO_2-/G nanocomposites
NF	Nanofiltration
PMMA	Poly(methyl methacrylate)
POPs	Persistent organic pollutants
PTFE	Polytetrafluoroethylene
QCM-D	Quartz crystal microbalance with dissipation
RBEI	Retractable backscattered electrons detector
SA	Surface acidity
SEI	Upper secondary electron in-lens detector
SEM	Scanning electron microscopy
SEs	Secondary electrons
SG	Sol gel
ST	Solvothermal
TBOT	Tetra(1-butyl) orthotitanate
TBSB	*tert*-butylstilbazolium betaine
TBT	Tetra(1-butyl) titanate
TEA	Triethanolamine
TEM	Transmission electron microscopy
TGH	TiO_2-G nanocomposites hydrogel
TL	Large particle size TiO_2
TPD	Temperature programmed desorption
TS	Small particle size TiO_2
ttbp9	3,20-di-tert-butyl-2,2,21,21-tetramethyl-3,5,7,9,11,13,15,17,19-docosanonaene
UF	Ultrafiltration
VB	Valence band

WB	2,6-dichloro-4-(2,4,6-triphenylpyridinium-1-yl)phenolate
XPS	X-ray photoelectron spectroscopy
XRD	X-ray diffraction

ABSTRACT

TiO_2 as a model photocatalyst is gaining great interest due to good activity, stability, low toxicity and cost-effectiveness. The rapid recombination between the photogenerated electrons and the holes on the TiO_2 surface can be diminished by using carbon-TiO_2 composites, especially Graphene (G) and Graphene Oxide (GO), which improve the photocatalytic activity of TiO_2 and stability under UV-visible light illumination. The determination of surface properties including surface acidity, polarity and surface area of photocatalysts allows the control and enhancement in the photocatalytic efficiency. This study aims at investigating the surface properties of TiO_2-G and TiO_2-GO nanocomposites using independent techniques, correlating these surface properties and photocatalytic activity and studying the effect of particle size and the amount of G and GO on these surface properties. TiO_2 nanoparticles of different sizes were prepared using sol-gel methodology and varying the rate of hydrolysis of the TiO_2 precursor. The as-prepared TiO_2 nanoparticles were used to prepare TiO_2-G and TiO_2-GO nanocomposites by mixing followed by sonication and stirring. The variables in the prepared nanocomposites were the percentage of the added G or GO together with the different TiO_2 particle size. Characterization of the formed nanocomposites and the blank samples was performed by using different techniques. The surface acidity was measured using perichromic dyes and NH_3-TPD; both measurements are independent. Surface polarity and polarizability were investigated using perichromic dyes to study their impact on the photocatalytic activity. Textural properties were investigated by measuring the surface area and average pore diameter. The structural characteristics of the samples were evaluated using FTIR, Raman and XRD. DRS-UV was employed to measure the band gap energy change with the addition of G or GO. The photocatalytic degradation of methylene blue (MB) dye, as a model water pollutant, was used to evaluate the photocatalytic activity of the samples. The characterization results indicated that two methods of preparation gave two average sizes of 436 ±59 nm and 251 ±32 nm for the samples denoted TL and TS which corresponds to large particle size TiO_2 and small

particle size TiO_2, respectively. Addition of G and GO affected the structure, surface properties and photocatalytic activity of the sample. The results for the photocatalytic activity of the prepared samples, exhibited superior activity over the unmodified TiO_2 and the rate enhancement ranged from 9.2 to 69.2% for TS, and 18.8 to 237.5% for TL, showing the clear advantage of using nanocomposites as photocatalysts for pollutants. Photocatalytic activity of the samples is dependent on many factors such as surface acidity, surface area and, to a much lesser extent, the change in band gap energy and the overall effect is a complex combination of all these factors. The formation of Ti-O-C chemical bonds in the samples is evidenced by the Raman results and the addition of G or GO has no effect on the crystal structure of the sample as shown in XRD results. The increase in overall surface acidity in most samples is believed to be primarily due to Brønsted acidity as Lewis acidity is generally lower than the blank in most samples. However, possible stacking of G and GO at higher concentrations resulted in the decrease in overall acidity with the increase in G or GO contents in some of the samples. Surface polarizability, which measures primarily the van der Waals surface interactions, increased with the increase in G content as would be expected due to the hydrophobic nature of G. Further investigations are needed, however, to extend the use of perichromic probes for determination of surface polarizability of solid surfaces. The overall surface acidity of the TL containing samples is generally higher than the TS samples due to higher degree of cross-linking.

In conclusion, TiO_2-G and TiO_2-GO nanocomposites prepared by mixing and sonication were studied for the effects of changing TiO_2 particle size, and of the presence and amount of G and GO. It was found that smaller particle size and the presence of G or GO improved the photocatalytic activity of the samples through the change in sample surface properties. Increasing the amount of G or GO in the samples led to limitations in the enhancement of catalytic activity. This is believed to be primarily due to possible blockage of the photocatalytic active sites on the surface of TiO_2.

TABLE OF CONTENTS

LIST OF FIGURES

LIST OF TABLES

Chapter (1)

Introduction

1.1. Titanium dioxide (TiO_2):

The remediation of wastewater from organic contaminants has attracted increasing attention in the past few years due to increased awareness of the importance of environmental preservation, and global water shortage leading to the necessity of water reuse. In addition, the presence of these contaminants leads to critical health problems. New, environmentally friendly and efficient methods for the removal of these contaminants are needed [1], [2]. Different approaches are used to treat wastewater such as evaporation, ultrafiltration, reverse osmosis and solvent extraction. These approaches though separating the contaminants from the water, do not convert these contaminants to harmless end-products. On the other hand, the photocatalytic reactions provide a good remedial alternative with the chemical conversion of contaminants to harmless end-products such as carbon dioxide and water [3].

Heterogeneous photocatalysis using TiO_2 as a model photocatalyst is gaining importance due to good photocatalytic activity, stability, low toxicity and cost-effectiveness [4]. TiO_2 has been historically used in many fields such as cosmetics, pigments and paper industry. The revolutionary report by Fujishima et al. in 1972 [5] to use the photocatalytic activity of TiO_2 for water splitting into hydrogen and oxygen is considered the starting point for the use of TiO_2 as photocatalyst [2], [3]. TiO_2 mediated photocatalysis involves the absorption of light photons to produce photo-excited electrons and positive holes. Both the electrons and the positive holes are involved in the photo- reduction/oxidation steps of the photocatalytic degradation process [6]. However, multiple drawbacks affect the use of TiO_2 as photocatalyst such as the rapid recombination between the photogenerated electrons and the holes on the TiO_2 surface, which decreases the photocatalytic efficiency. The low photo-response under visible light irradiation due to wide band gap is another disadvantage of the use of TiO_2 as photocatalyst [7].

Many modifications are reported to prevent this recombination and to increase the photo-response in the visible region. These modifications include doping with transition metals such as V, Ni and Cr and doping with inorganic dopant such as sulfate anions, nitrogen (N) and sulfur (S). In addition, the carbon-TiO_2 composites, especially Graphene (G) and Graphene Oxide (GO), proved superior enhancement of the photocatalytic activity of TiO_2 and stability under UV-visible light illumination [8]–[10].

1.2. TiO_2- Graphene (G)/Graphene Oxide (GO) nanocomposites:

Graphene (G), a carbon allotrope, and Graphene oxide (GO) have unique properties. They have recently been the subject of different investigations in which they were combined with TiO_2 to form composite materials with enhanced photocatalytic performance. This is achieved through three main mechanisms:

1- G, GO with their two dimensional (2D) mat structures increase the surface area of the TiO_2 photocatalyst leading to an increase in the overall photocatalytic activity.
2- Strong π–π interaction between the contaminant and the aromatic network of G, GO leads to enhanced adsorption on the surface of the photocatalyst.
3- Due to the high electronic conductivity of G, GO, they act as electron sinks for the excited electrons on the surface of TiO_2. The high conductivity will decrease the recombination between the photogenerated electrons and the positive holes improving the photodegradation of the contaminant substrate using TiO_2- G/GO nanocomposites [11]–[14].

1.3. Perichromism:

The surface properties of metal oxides present an important aspect in different applications, particularly catalytic properties. Surface acidity, basicity, polarity and surface area play an important role in heterogeneous catalysis in general, and photocatalysis in particular. Their effective determination and manipulation allows the control and improvement of photocatalytic efficiency [15].

The term perichromism refers to the effect of the medium on the spectra, absorption or emission, of certain substances or "probes" whose intramolecular charge-transfer bands are especially sensitive to the properties of the medium. For liquids, the term solvatochromism is employed. This method provides an expedient, accurate and relatively simple method to determine the surface properties of different species. The adsorption of the perichromic probes onto the solid surfaces leads to measurable changes in the corresponding UV-visible spectra. These changes can then be correlated to the solid's surface properties such as acidity, basicity and empirical polarity.

The use of perichromism to probe the surface properties of solid materials presents a number of advantages such as the small amounts the dye needed, straightforward measurements using UV-visible spectrophotometers, reproducibility, high specificity, and versatility. Care should be exercised, however, in order to ensure the presence of monolayer of the dye on the surface. Pronounced "stacking" of the dye leads to false results because the upper layer of the probe is not sampling the solid surface [16].

1.4. Aim of the current work:

This study is aimed at investigating the effect of introducing G or GO on the photocatalytic activity of TiO_2, using the oxidation of methylene blue (MB) dye as a model reaction. A central part of this thesis is to investigate the surface properties of the produced TiO_2-G and TiO_2-GO nanocomposites by several *independent techniques*, because the catalytic efficiency is intimately linked to surface properties. The properties investigated are surface area and porosity, total surface acidity (Brønsted plus Lewis acidity), surface Lewis acidity, surface empirical polarity and polarizability, surface morphology and additional information on surface properties was obtained from the results of UV-Visible, FTIR, and Raman spectroscopy. The nanocomposites synthesized were tested as catalysts for the photo-oxidation of MB, and the results correlated with their composition, and compared to those obtained with unmodified TiO_2.

Chapter (2)

Literature Review

This chapter presents the main investigations of TiO_2-Graphene (G)/Graphene Oxide (GO) nanocomposites and their application for photocatalytic degradation. These investigations are grouped according to the synthesis methods used. In addition, the use of perichromic dyes to measure the surface properties of different solid surfaces will also be discussed.

2.1. Synthesis and applications of TiO_2-G/GO nanocomposites:

The synthesis methods used for the preparation of TiO_2-G/GO nanocomposites include hydrothermal (HT), solvothermal (ST), simple mixing and sonication, Liquid phase deposition (LPD) and sol-gel techniques. Other less employed methods have also been utilized, such as chemical vapor deposition (CVD), spin coating and electrospinning.

2.1.1. The hydrothermal (HT) method:

HT synthesis involves the use of controlled temperature and pressure usually using PTFE-lined autoclaves. The use of elevated pressure allows the use of low boiling point solvents such as water, above their boiling temperature in the synthesis of various inorganic solids. The use of low boiling point solvents is advantageous as most high boiling point solvents, such as dimethyl sulfoxide (DMSO), are either toxic or expensive. The elevated temperature is required to produce high quality single crystal of the required nanoceramic material. The ability to control the quality and composition of the formed crystal are among the advantages of the HT synthesis. On the other hand, the inability to observe the crystal growth and the high cost of the used autoclaves are the main disadvantages associated with this method [17]–[20]. The HT reaction helps in the formation of the TiO_2-G nanocomposites and in partially reducing the GO into G [21]. As a source of TiO_2 in the HT method, pristine TiO_2 nanoparticles may be used [22]. On the other hand, the addition of a TiO_2 precursor such as TiF_4, TiN, $(NH_4)_2TiF_6$, TBT (tetra (1-butyl) titanate), or Ti (IV) isopropoxide for example to give TiO_2 nanoparticles is the preferable way to better control the morphology and the properties of the formed TiO_2-G /GO nanocomposites [23].

Uniform distribution of TiO_2 nanoparticles on the surface of G sheets was achieved by Bai et al by using simple HT method. TiF_4 was used as a precursor and HI was used to

reduce GO to G and as a morphology controlling agent. The results were confirmed using SEM, TEM, FTIR and Raman spectroscopy. The formed TiO_2-G nanocomposites exhibited high stability under both UV (λ = 365 nm) and visible (λ = 400 nm) light irradiation. The higher photocatalytic degradation of bisphenol A (BPA), a common environmental pollutant, using TiO_2-G nanocomposites compared to pure TiO_2 was attributed to the decrease in the electron–hole recombination rates in the formed nanocomposites under both UV and visible light irradiation. Bai et al also studied the effect of the pH of the medium and found that increasing the pH value causes an increase in the photodegradation of BPA. X-ray photoelectron spectroscopy (XPS) was employed to study the degradation intermediates and to propose a degradation pathway for BPA [23].

$TiCl_4$ was used as a precursor by Sher Shah et al with GO in one step HT reaction. The reduction of GO to G and the hydrolysis of $TiCl_4$ to titania nanoparticles were achieved simultaneously. They reported the method as a "green method" due to the single step reaction without the use of toxic solvents or reducing agents. The formed TiO_2 nanoparticles were biphasic with both anatase and rutile phases. The reduction of GO was not complete as confirmed by the FTIR results and the effect of different G loading was studied. The nanocomposite with 2 wt% G showed higher photocatalytic degradation of rhodamine B dye and the colorless benzoic acid pollutants under visible light [21].

Nitrogen-doped anatase TiO_2 and G nanosheets were used to synthesize N-doped TiO_2-G nanocomposites with improved photocatalytic activity by a simple HT method. The solid powder of TiN was used as the source of the N-doped TiO_2 nanoparticles and GO was reduced during the HT reaction. The resulting nanocomposites showed improved photocatalytic degradation of MB dye under visible light irradiation and a mechanism for the improved photocatalytic activity was proposed [24]. Gu et al. reported the HT preparation of N-doped TiO_2-G and Nitrogen and Vanadium co-doped TiO_2-G (N,V–TiO_2–G) nanocomposites with higher visible light photocatalytic activity towards the degradation of acid orange-7 dye (AO7) than the blank TiO_2, N–TiO_2 and N,V–TiO_2 [25].

Amine functionalized TiO_2 nanoparticles with positively charged surface were used to improve the interaction with the negatively charged surface of GO. The reduction of GO

to G and the strong wrapping of TiO_2 with G is performed during the HT reaction [26], [27]. The same procedure, utilizing amine functionalized TiO_2 nanoparticles, was used to synthesize magnetically recyclable TiO_2-G nanocomposites using silica coated magnetic iron oxide nanoparticles. The recyclable TiO_2-G nanocomposites showed rapid degradation of the pharmaceutical compounds carbamazepine and caffeine and the recovery of the nanocomposites was done by simple exposure to magnetic field for *ca.* one minute[28].

HT method was used to deposit TiO_2-G nanocomposites on a polypropylene porous filter to give a modified photocatalytic filtering system for water treatment by Ariffin et al. Titanium (IV) isopropoxide, as a precursor, was added to triethanolamine (TEA) to produce TiO_2 ionic solution. This solution was then added to GO suspension in water/ethanol mixture (1:14) and stirred for 24 hours at room temperature. The mixture was placed in test tube with a porous filter for another 24 hours then placed in a PTFE-lined autoclave and heated to 120^{o}C for 24 hours. The modified filter exhibited high stability and improved photocatalytic degradation of MB than the original filter [29].

Recently, Nguyen et al. studied the effect of temperature on the crystal phase and surface area of the prepared TiO_2-G nanocomposites during HT synthesis. Their results showed that lower temperature led to amorphous samples with higher surface area while higher temperature led to the formation of the anatase crystalline phase and lower surface areas for the formed nanocomposites as confirmed by XRD, SEM, N_2 adsorption (BET), and Raman spectroscopy. The photocatalytic degradation of MB and orange II dyes were evaluated and the former dye was easier to be degraded than the latter one [30]. Facile one-pot HT reaction was used to synthesize TiO_2-G nanocomposites hydrogel (TGH) with three-dimensional interconnected channels by Zhang et al. The formation of three dimensional hydrogel was confirmed using SEM and the formed hydrogel showed improved activity as photocatalyst adsorbent and supercapacitor due to enhanced photocatalytic activities, increased adsorption capacities, and improved electrochemical capacitive performance in comparison with TiO_2 nanoparticles and pristine graphene hydrogels. The adsorption and photocatalytic performance were evaluated using the photodegradation of MB dye. On the other hand, Cyclic voltammetry (CV), electrochemical impedance spectroscopy (EIS) were employed for electrochemical

measurements [31]. The effect of varying the G content on the photocatalytic activity of TiO_2-G nanocomposites was studied by Li et al. TiO_2-G nanocomposites prepared with different G amounts by adding different content of commercial TiO_2 (P25) into GO dispersion in water. They obtained homogeneous suspension by stirring for 2 hours which was heated at 120^oC for 3 hours in a PTFE-lined autoclave. The reduction of GO and the loading of TiO_2 onto G was achieved simultaneously during the HT process. The obtained composites were centrifuged, washed with water and dried at 50^oC. The prepared TiO_2-G composites showed higher adsorption and photocatalytic efficiency for MB and reactive black 5 dyes removal than the blank TiO_2 nanoparticles [32].

TiO_2 nanotube-G nanocomposites were synthesized by an alkaline HT process using NaOH. This process was used to convert commercial TiO_2 (P90) to TiO_2 nanotubes and to reduce GO to G, simultaneously. The formed TiO_2-G nanocomposites with 10% G showed threefold increase in photocatalytic efficiency compared to pure TiO_2 nanotubes and increase the G content over 10% decreased the photocatalytic activity of the formed nanocomposites [22]. In the same context, TiO_2 nanowires prepared by Pan et al. by the mixing of KOH aqueous solution (10M) and commercial TiO_2 nanopartilcles (P25) followed by stirring for 30 minutes. The produced suspension was placed in a PTFE-lined autoclave at 200^oC for 24 hours. The obtained products were washed with HCl aqueous solution, deionized water (DI) and methanol then vacuum filtered and dried. The produced TiO_2 nanowires have more uniform distribution on the surface of G nanosheets with less agglomeration than the TiO_2 nanoparticles thus improving the adsorptive power and photocatalytic activity of the TiO_2 nanowire-G composites [33].

2.1.2. The solvothermal (ST) method:

The ST method of synthesis involves the main features of the HT synthesis with the exception of using non-aqueous solvents to yield the TiO_2-G nanocomposites. However, higher temperatures can be used in ST synthesis and different organic solvents can be used. The control over the crystallinity, shape and size distribution of the formed nanomaterials is usually much better in ST synthesis than HT method [18].

Wang et al. used a one-pot ST method for the preparation of novel G/CNT/T composites. They added GO, MWCNTs (multi-wall carbon nanotubes) to TBT, as a TiO_2 precursor,

in isopropanol. The formed nanocomposites showed high photocatalytic activity for MB degradation and chromium (VI) reduction [34].

In a study by Qian et al. titanium (IV) butoxide and G were added to ammonia solution in isopropanol followed by stirring. The ammonia solution was used as a nitrogen source and reaction medium. The reaction mixture was mixed in PTFE-lined autoclave at 180^{o}C to prepare N—doped TiO_2-G nanocomposites. Density functional theory (DFT) calculations were used to explain the enhancement in the photodegradation activity after adding the G to the N-doped TiO_2 [35].

Li et al. used two TiO_2 precursors, $TiCl_4$ and titanium (IV) isopropoxide, together with GO Pluronic P123, a Triblock copolymer based on poly(ethylene glycol)-poly(propylene glycol)-poly(ethylene glycol) and a non ionic surfactant, to form a sol which gave the desired TiO_2-G nanocomposites upon ST treatment at 150^{o}C for 24 hours. The formed nanocomposites were employed to degrade aqueous persistent organic pollutants (POPs) such as aldicarb, rhodamine B and norfloxacin under solar and visible light irradiation. HPLC/MS/MS was used to study the degradation intermediates of aldicarb and norfloxacin and a detailed degradation pathway was proposed [36].

Huang et al. reported that chemically bonded TiO_2-G nanocomposites prepared by dropwise addition of tetra(1-butyl) orthotitanate (TBOT) ethanol solution to G water dispersions containing specific amount of G. after 120 minutes stirring, the dispersion was placed in a PTFE-lined autoclave at 200^{o}C for 10 hours. The produced nanocomposites have superior photocatalytic properties compared to the TiO_2-G nanocomposites synthesized using mechanical mixing. The TiO_2-G nanocomposite with 2.5 wt% G showed the highest photocatalytic activity towards the photodegradation of formaldehyde in air [37].

Full reduction of GO to G could be achieved by adding glacial acetic acid during the ST process. Min et al. slowly added Titanium (IV) isopropoxide to GO dispersion in ethanol containing glacial acetic acid. After stirring for two hours the mixture was heated at 120^{o}C for 24 hours in a PTFE-lined autoclave. The complete reduction of GO and deposition of TiO_2 onto G were achieved during the ST reaction. The formed TiO_2-G nanocomposites showed high photocatalytic degradation of MB under both UV and visible light irradiation [38].

The control of the morphology of the formed TiO_2-G nanocomposites could be achieved using ethylene glycol as reported by Cai et al. G nanosheets were added to $TiCl_4$ solution in ethylene glycol and sonicated for 10 hours. PTFE-lined autoclave was used to heat the mixture at 180^{o}C for 12 hours. The formed TiO_2-G nanocomposites showed high lithium storage performance and so could be used as material for anodes in lithium ion batteries. The electrochemical performance of the formed composites was examined using coin-type cells versus metallic lithium in an enlarged potential window and high specific charge capacity was obtained and the formed composites exhibit excellent rate capability [39].

The morphology of the formed nanocomposites can also be controlled using HF as reported by Gu et al. who prepared anatase TiO_2 with exposed (001) facets G nanocomposites through a simple one pot ST route. The nanocomposites were prepared by adding TBT to GO solution in isopropanol and stirred for 30 minutes. HF was added and the mixture is heated at 180^{o}C for 12 hours in a PTFE-lined autoclave [40].

2.1.3. Simple mixing and sonication:

These methods are gaining greater attention due to their simplicity and the ease of controlling the reaction conditions. The method involves simply mixing the TiO_2 and G or GO (either pristine or functionalized), followed by sonication and stirring to ensure the proper contact between the nanocomposite components. UV irradiation, heat or chemical reducing agents may be employed to reduce GO to G during the process. The effect of sonication arises from acoustic cavitational collapse of bubbles producing intense local heat, high pressure and rapid heating-cooling rates [18].

TiO_2-GO nanocomposites were prepared by Gao et al. by simple mixing without further reduction of GO to G. The method involved the dispersion of GO in water followed by the addition of different types of TiO_2, either commercially available (P25) or prepared by heating TBT in isopropanol at 200^{o}C for 20 hours. The mixture was ultrasonicated for 30 minutes and stirred for 2 hours followed by centrifugation and vacuum drying to obtain the final TiO_2-GO nanocomposites. The products showed improved photodegradation of acid orange 7 (AO7) and disinfection of *Escherichia coli* (*E. coli*) under simulated solar light and the enhancement of the photocatalytic activity was

attributed to the improvement in the light absorption capacity and efficient electron-hole charge separation [41].

The improvement in the photodegradation of acid orange 7 (AO7) under UV irradiation and sterilization of *Escherichia coli* (*E. coli*) under simulated solar light irradiation, were also reported by Liu et al. Large scale production of GO-TiO_2 nanorods composites (GO-TiO_2 NRCs) was achieved using two phase water-toluene interface to deposit TiO_2 nanorods on the GO sheets. The oleic acid capped TiO_2 nanorods were prepared by mixing *tert*-butylamine in water with titanium (IV) isopropoxide in oleic acid and the mixture is placed in a PTFE-lined autoclave and heated at 180^{o}C for 6 hours. Oleic acid was used for better dispersion in toluene. The prepared oleic acid capped TiO_2 nanorods were then added to GO solution in DI water and the resultant mixture was stirred for 24 hours at room temperature to ensure good coordination between GO and TiO_2 nanorods. The formed GO-TiO_2 NRCs showed higher photocatalytic activity compared to blank TiO_2 nanorods and GO-TiO_2 nanoparticles composites. The higher photocatalytic activity of GO-TiO_2 NRCs was attributed to the more (101) facets available and the efficient anti-charge recombination [42].

The photodegradation of MB was enhanced using TiO_2-GO nanocomposites prepared by simple mixing in DI water and sonication for 90 minutes. The GO in the prepared composites increased the photocatalytic activity by acting as electron acceptors, adsorbents and photosensitizes. The increase in the GO content up to 10% was reported to increase the photodegradation activity of the formed nanocomposites. The interaction mechanism between GO and MB and enhancement in the photodegradation activity was proposed [43].

Carboxy functionalized G was prepared by thermal exfoliation of GO followed by chemical functionalization with carboxy groups using nitric acid and sulfuric acid under sonication. Titania nanoparticles were then decorated on the carboxy functionalized G matrix to result in the nanocomposites as confirmed by TEM, SEM, XRD, FTIR and Raman spectroscopy. The photodegradation of rhodamine B under solar light irradiation was investigated and the formed nanocomposites had superior activity compared to the blank titania nanoparticles and the non-functionalized TiO_2-G nanocomposites and the mechanism was proposed [44].

Ghasemi et al. prepared TiO_2-G nanocomposites by mixing TiO_2 and GO suspensions with sonication followed by UV light reduction of GO to G. X-ray photoelectron spectroscopy (XPS) was used to confirm the reduction of GO to G and the formation of Ti-C bonds. The formed TiO_2-G nanocomposites were then doped with noble metals (Pt and Pd) and the highest photocatalytic activity was observed for Pt-TiO_2-G nanocomposites. The photocatalytic degradation of two environmental pollutants (2,4-dichlorophenoxyacetic acid and Reactive Red 195) was evaluated under both UV and visible light irradiations [45].

Photocatalytic reduction of GO to G using UV light irradiation was also used to prepare G-coated TiO_2 together with the typical TiO_2-G composites. Photocatalytic production of hydrogen and the photocurrent generation were improved using the G-coated TiO_2 composites due to easier interfacial charge transfer between the TiO_2 and the G sheets coating them [46].

The TiO_2-G nanocomposites prepared by UV light reduction of GO to G was used to make films by drop coating onto conducting fluorinated tin oxide (FTO) slides. The nanocomposite films showed superior electron lifetime and photocurrent generation properties. The as-prepared TiO_2-G nanocomposites improved the performance of photovoltaic systems such as dye-sensitized solar cells (DSSC) [47].

Thermal treatment under inert atmosphere of TiO_2-GO composites was reported to reduce some of the surface oxygenated groups to produce TiO_2-G nanocomposites. The photocatalytic activity of the formed TiO_2-G nanocomposites was evaluated for the degradation of methyl orange and diphenhydramine anti-histaminic drug under near-UV/Vis irradiation. The thermal treatment increased the photocatalytic activity of the formed composites proving that the TiO_2-G nanocomposites had more efficient charge separation than the TiO_2-GO composites. Furthermore, the results showed that the increase in the GO content, after 1.4 wt% GO, decreased the photocatalytic performance of the prepared nanocomposites [48].

2.1.4. Sol-gel methods:

The sol-gel methods involve the hydrolysis of suitable titanium precursor, usually an alkoxide, followed by condensation in the presence of GO. The fact that high pressures and temperatures are not needed is an important advantage of sol-gel methods over the aforementioned methods. The development of Ti-O-Ti and Ti-O-C bonds is favored with low amounts of water, lower rates of hydrolysis and excess of the titanium precursor in the reaction mixture [18], [49]. The addition of TiO_2 precursor to the GO suspension leads to the formation of relatively stable oxo- and hydroxo- connections between their surfaces forming sols which upon further addition of GO gives gel like structures that yield the required nanocomposites upon drying or calcinations.

Štengl et al. used titania peroxo-complex as a precursor to fabricate TiO_2-GO nanocomposites with different GO content using one-pot simple sol-gel method. The hydrolysis of titanium oxysulfate ($TiOSO_4$) was achieved using NaOH under constant stirring in ice bath followed by the addition of hydrogen peroxide solution to produce titania peroxo-complex. The photocatalytic degradation of butane in the gas phase was evaluated under both UV and visible light irradiation [49].

Liu et al. used titanium (IV) isopropoxide as the TiO_2 precursor and G, chemically reduced from GO using hydrazine hydrate, to prepare TiO_2-G nanocomposites by a sol-gel method. The nanocomposites were prepared by dropwise addition of titanium (IV) isopropoxide into a mixture of G and cetyltrimethylammonium bromide in ethanol under stirring followed by addition of DI. The suspension was stirred for 8 hours, dried and annealed at 500^{o}C for 5 minutes. The as-synthesized composites exhibited high photocatalytic bleaching activity for MB under visible light (λ>430 nm) irradiation [50].

Titanium oxysulfate was used as TiO_2 precursor by Park et al. in a sol-gel procedure to produce novel CdS-G-TiO_2 composites with improved photodegradation of MB under visible light irradiation. The nanocomposites were prepared by adding Titanium oxysulfate to CdS-G composites, previously prepared by mixing $CdCl_2$, Na_2S and GO, followed by drying and heating at 500^{o}C. [51].

2.1.5. Liquid phase deposition (LPD):

The ability to synthesize organic/metal oxide hybrid materials under ambient conditions without the need to post-annealing process is the main advantage of LPD. This method is considered as a simple modification of sol-gel procedure, hence both share the main general features. Thus, Pastrana-Martínez et al. used LPD to deposit TiO_2 on the surface of G sheets using ammonium hexaflurotitanate (IV), $(NH_4)_2TiF_6$ as the TiO_2 precursor and GO thermally reduced at 200^oC to yield G sheets. The hydrolysis of the TiO_2 precursor and the formation of the TiO_2-G composites stabilized by H-bonds occur simultaneously. The photodegradation of diphenhydramine (DP) and methyl orange as model water pollutants was improved using the formed nanocomposites [52], [53]. Similarly, Jiang et al. used ammonium hexaflurotitanate (IV) and thermally reduced GO to prepare TiO_2-G nanocomposites by LPD and the prepared nanocomposites improved the photocatalytic reduction of chromium (VI) [54].

LPD methods were used to produce ultrafiltration membranes which combined the photodegradation properties of TiO_2-G/GO nanocomposites together with the filtration capacity. Athanasekou et al. used dip-coating technique to deposit TiO_2-GO nanocomposites, without further reduction, on the surface of different ceramic membranes. These membranes included silica nanofiltration (NF) single channel monoliths with nominal pore size of 1 nm and γ-alumina ultrafiltration (UF) single channel monoliths with nominal pore size of 5 and 10 nm. The performance of the novel hybrid photocatalytic/ultrafiltration system was evaluated for the removal of MB and methyl orange from aqueous solutions [55]. Moreover, antifouling hierarchical filtration membranes were synthesized using vacuum filtration of GO-TiO_2 composite dispersion in ammonia through polycarbonate filter membranes followed by vacuum filtration of TiO_2 suspension through the obtained GO-TiO_2 film. Ammonia was used to form stable dispersion, and the filtration and photodegradation of direct red 80 and direct blue 15 dye solutions in dark and under UV irradiation was evaluated [56].

2.1.6. Other methods:

Qin et al. used chemical vapor deposition (CVD) and aerosol technique to prepare TiO_2-G nanocomposites in presence of thioglycolic acid. The preparation involves the deposition of TiO_2, dispersed in water containing thioglycolic acid, on a poly(methyl methacrylate) (PMMA) support covered with a monolayer of G by aerosol technique to ensure high uniformity and low TiO_2 agglomeration. The thioglycolic acid was used to prevent TiO_2 aggregation, and subsequently removed in the vacuum oven. The photocurrent response for the formed composites were measured and evaluated for further applications in the fabrication of photoelectric devices [57].

Wojtoniszak et al. used CVD to produce TiO_2-G nanocomposites with high photocatalytic activity towards the phenol degradation. TiO_2-G nanocomposites were prepared by placing pristine TiO_2 powder in a horizontal furnace with a quartz tube reactor. Acetylene was used as the carbon source of G by heating at 400-500^oC in the presence of TiO_2 in the furnace. Shorter CVD time and higher temperature produce the highest photocatalytic activity among the synthesized samples [58].

Gao et al. used layer by layer (LBL) technique to pour TiO_2 suspension followed by GO suspension on a polysulfone base membrane to prepare a photocatalytic TiO_2-GO grafted filter membrane. UV irradiation was used to reduce the GO to G and the effectiveness of the LBL process to deposit TiO_2-GO on the membrane was determined by quartz crystal microbalance with dissipation (QCM-D). The TiO_2–GO membranes exhibited improved MB photodegradation under UV and simulated sunlight [59].

One-step microwave-assisted synthesis of TiO_2-G nanocomposites is reported by Yang et al. where the reduction of GO to G and the coating of TiO_2 on the G surface occur simultaneously. The TiO_2-G nanocomposites were prepared by mixing GO in water with commercial TiO_2 (P25) then this mixture was placed in focused microwave equipment and heated at 140^oC for 5 min. The TiO_2-G nanocomposites exhibited superior photocatalytic degradation of MB [60].

Self cleaning applications of TiO_2-G nanocomposites were studied by Anandan et al. after preparing the nanocomposites using spin-coating. They utilized titanium (IV) bis ammonium lactate dihydroxide together with G sheets in presence of glycerol to give a homogeneous film on a glass substrate, which was calcined at 400^oC before use. The

resulting structure showed improved enhanced photo activity under UV light irradiation [61].

Electro-spinning [62] was used to produce TiO_2-G nanocomposites with improved photocatalytic and photovoltaic properties as evaluated using photodegradation of methyl orange and dye-sensitized solar cells. The TiO_2-G nanocomposites were prepared by dissolving G in N,N-dimethyl acetamide containing polyvinyl acetate (PVAc), acetic acid, and TiO_2 followed by electrospinning and sintering at 450°C for 1 hour.

2.2. Determination of surface properties using perichromic dyes:

Ichimura et al. used nanohybrids of surface-modified silica nanoparticles and Riechardt's dye, 2,6-diphenyl-4-(2,4,6-triphenylpyridinium-1-yl)phenolate, mixed by dry bead milling to examine the effect of environmental conditions on the solid surface. The silica nanoparticles were initially treated with polysiloxane to make the surface more hydrophobic to allow better interaction with the dye. Riechardt's dye was employed since the dye's absorption maximum is affected by micro-environmental polarity. The color of the hybrid was greatly affected by the external atmospheric conditions where purple, bluish and greenish colors were obtained for the wet, ambient (as-prepared) and dry (in presence of calcium chloride as desiccant) conditions respectively. The results confirmed that perichromic dyes can be used to probe the surface polarity of solid metal oxide in different conditions [63].

Spange et al. used 3-(4-amino-3-methylphenyl)-7-phenyl-benzo1,2-b:4,5-b′difuran-2,6-dione dye to study its perichromic behavior in a set of solvents and solid acids such as silicas, aluminas and aluminasilicates. The observed positive perichromism of the dye (λ_{max} increases with increasing medium polarity) was associated with an increase in the basicity and dipolarity/polarizability of the medium [64]. The same group used 2,6-diphenyl-4-(2,4,6-triphenyl-1-pyridinio)phenolate and an eicosafluorine substituted derivative of the same dye as surface polarity indicators to measure the Reichardt's $E_T(30)$ empirical polarity values of different solid acids. The solid acids employed in this study included silicas, aluminas, aluminasilicates, titanium dioxides and alumina functionalized silica particles. $Fe(phen)_2(CN)_2$ [*cis*-dicyano-bis(1,10-phenanthroline)iron(II)] and Michler's ketone [4,4′-bis(*N*,*N*-dimethylamino) benzo-

phenone] were also used to measure the α (hydrogen-bond donor acidity) and π^* (dipolarity/polarizability) values of these acids. The results showed that the surface of these solid acids had solvent-like properties and the polarity values were strongly affected by the experimental conditions [65]. Their work was extended to other solid materials as synthetic polymers, copolymers and hybrid materials to suggest a general polarity scale for solid materials [66]. In addition, other perichromic dyes were used to examine the surface polarity of silica [67]–[73], alumina [74] and zeolites [75].

Spange et al. described the perichromic behavior of four merocyanine-type dyes derived from barbituric acid on different metals and metal oxides. The surface polarity of colored metal oxides as tungsten (VI) oxide and iron (III) oxide as well as the interaction with metals like aluminum and zinc were investigated. The perichromic behavior of these dyes is mainly dominated by the hydrogen bond donating ability and dipolarity/polarizability properties of the medium and they can be used for probing surface polarity of colored metal oxides [76].

The effect of various chain length of alkyl-functionalized silica particles on the surface polarity were studied using differently substituted Reichardt's dyes. The value of the surface polarity of the silica particle decreased with increasing the degree of surface functionalization of the silica particles with alkyl groups. However, the length of the alkyl groups presented no significant effect on the surface polarity. In addition, lower polarity values were obtained when a more sterically substituted dye was employed [77].

The surface of the metal oxides such as silica contains regions of different polarity and acidity. This result was concluded by Khristenko et al. using Riechardt's dye, and the structurally related Wolfbeis (WB dye) dye 2,6-dichloro-4-(2,4,6-triphenylpyridinium-1-yl)phenolate to probe the surface polarity of different types of silica particles [78].

El Seoud et al. used perichromic dyes to study the effect of varying the calcinations temperature on the surface properties of TiO_2 nanoparticles. The used perichromic probes were *cis*-dicyano-bis(1,10)-phenanthroline iron(II), $Fe(phen)_2(CN)_2$; Michler's Ketone; 2,6-dibromo-4-[(*E*)-2-(1-butylpyridinium-4-yl)ethenyl] phenolate; 3-(4-amino-3-methylphenyl)-7-phenylbenzo[1,2b:4,5b′]difuran-2,6-dione; and 2,6-diphenyl-4-(2,4,6-triphenyl- pyridinium-1-yl)phenolate. These dyes were used to measure empirical polarity; Lewis acidity; Lewis basicity; and dipolarity/polarizability at different

calcinations temperatures and these values were correlated to the Brønsted acidity and basicity.. The increase in the calcinations temperature would decrease the number of the surface hydroxyl groups leading to subsequent decrease in the Lewis acidity, Brønsted acidity and dipolarity/polarizability and slight increase in the Lewis basicity. Based on the obtained results and Monte Carlo (MC) simulations, the adsorption of the perichromic dye 2,6-dibromo-4-[(*E*)-2-(1-butylpyridinium-4-yl)ethenyl] phenolate was proposed to be perpendicular on the surface of the TiO_2 nanoparticles [16].

Chapter (3)

Theoretical Background

3.1. TiO_2 and photocatalytic applications:

The need for renewable energy sources, together with addressing environmental pollution present top priorities worldwide [79], [80]. Photocatalysis, which involves the use of solar energy to catalyze different processes, can provide a promising solution. Remediation of environmental pollution using photocatalysis is very promising in water/air purification [45], [49], filtration [55] and self cleaning applications [61]. In addition, the number of publications concerning water splitting for H_2 generation as a clean energy source [81], hydrocarbon fuel production [82], solar cells [83], incorporation in high performance Lithium ion batteries [84], [85], supercapacitors [31] and sensing applications [86], [87] using TiO_2 containing photocatalysts have increased tremendously in the past few years. Other photocatalysts such as ZrO_2, ZnO, Fe_2O_3, WO_3, CdS, $SrTiO_3$, Ag_3PO_4 and C_3N_4 have been reported in various applications [88].

TiO_2 is considered most suitable for industrial applications. High stability, superior photocatalytic efficiency and low cost are among the main characteristics of TiO_2 making it the most studied photocatalyst [89]. The history of TiO_2 can be tracked to the early twentieth century. Goodeve et al in 1938 reported the bleaching of dyes under UV light irradiation of TiO_2 surface due to the formation of active oxygen species. Goodeve et al refer to TiO_2 as "photosensitizer" [90]. The terminology TiO_2 photocatalyst can be traced to Kato and Mashio report in 1956 entitled "Auto-oxidation by TiO_2 as a photocatalyst" as reported by Hashimoto et al [89]. TiO_2 has 3 main crystal phases which are anatase, rutile and brookite with anatase having the highest photocatalytic activity among these phases [91]. However, only anatase and rutile are commonly utilized in photocatalytic applications. Anatase crystalline phase of TiO_2 has the highest photocatalytic activity but is thermodynamically unstable relative to rutile. However, the large band gap and the absorption of only ~4% of solar irradiation are major obstacles in the utilization of TiO_2 as photocatalyst [91], [92]. Typical photocatalytic reaction of TiO_2 shown in Figure (3-1) illustrates the main mechanistic steps for TiO_2 photocatalysis. The first step involves the absorption of a light photon with equal or higher energy than the band gap to excite electrons from the Valence Band (VB) to the Conduction Band (CB) leaving positive holes (h^+) behind. These photo-induced electrons and positive holes migrate to the surface to react with adsorbed species. Adsorbed oxygen reacts with the electrons in the

CB to form super oxide radical ($^{\bullet}O_2^-$) and hydroxyl radical ($OH^{\bullet}$) which are very strong oxidizing agents and the main intermediates in the degradation of organic pollutants into biodegradable products. This process is referred to as the photo-reduction phase. The photo-oxidation phase, on the other hand, involves the oxidation of the adsorbed water molecules and hydroxyl anions by the positive holes in the CB into hydroxyl radicals ($OH^{\bullet}$) that can degrade organic molecules (such as different pollutants) to harmless products [93], [94]. The main reactions involved in the photocatalysis of TiO_2 are summarized in equations (3-1) – (3-6).

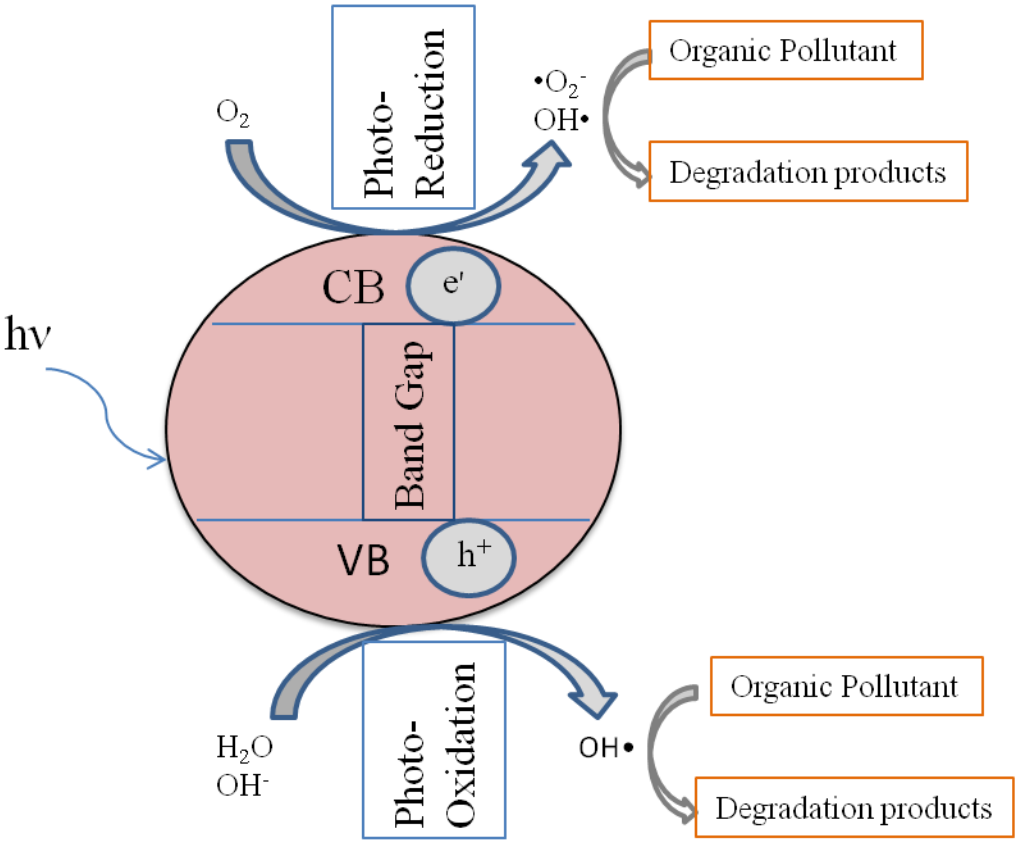

Figure (3.1): Principles of TiO_2 photocatalysis.

$$TiO_2 + h\nu \rightarrow TiO_2^* (e^- + h^+) \quad (3\text{-}1)$$

$$H_2O + h^+ \rightarrow HO^{\bullet} + H^+ \quad (3\text{-}2)$$

$$e^- + O_2 \rightarrow {}^{\bullet}O_2^- \quad (3\text{-}3)$$

$${}^{\bullet}O_2^- + H^+ \rightarrow HO_2^{\bullet} \quad (3\text{-}4)$$

$$H^+ + {}^{\bullet}O_2^- + HO_2^{\bullet} \rightarrow H_2O_2 + O_2 \quad (3\text{-}5)$$

$$H_2O_2 + h\nu \rightarrow 2\ HO^{\bullet} \qquad (3\text{-}6)$$

However, the rapid recombination between the photogenerated electrons and positive holes on the TiO_2 surface decreases the photocatalytic efficiency. Many modifications are reported to improve the charge separation, efficient light absorption, and the surface reactivity of TiO_2 in order to enhance the photocatalytic activity. These modifications include doping with transition metals such as V, Ni and Cr or inorganic dopant such as SO^{-4}, N and S. In addition, the carbon-TiO_2 composites, especially Graphene (G) and Graphene Oxide (GO), proved superior enhancement of the photocatalytic activity of TiO_2 and stability under UV light illumination [8]–[10]. Surface chemistry plays a crucial role in photocatalysis since most chemical and physical processes occur on the surface of the photocatalyst [88].

3.2. Graphene (G) and Graphene Oxide (GO):

Graphene is one of the carbon allotropes (along with carbon nanotubes, diamond, graphite, fullerene, etc.) which exists in one atom thick layers tightly arranged in a two dimensional (2D) honeycomb-like crystal lattice structure. Graphene has shown extraordinary electrical, thermal, catalytic, mechanical and optical properties giving rise to a wide variety of applications. The C-C bond length in graphene is ca. 0.142 nm. Graphene can stack in many layers to form graphite sheets having an inter-planar distance of 0.335 nanometers as shown in Figure (3-2).

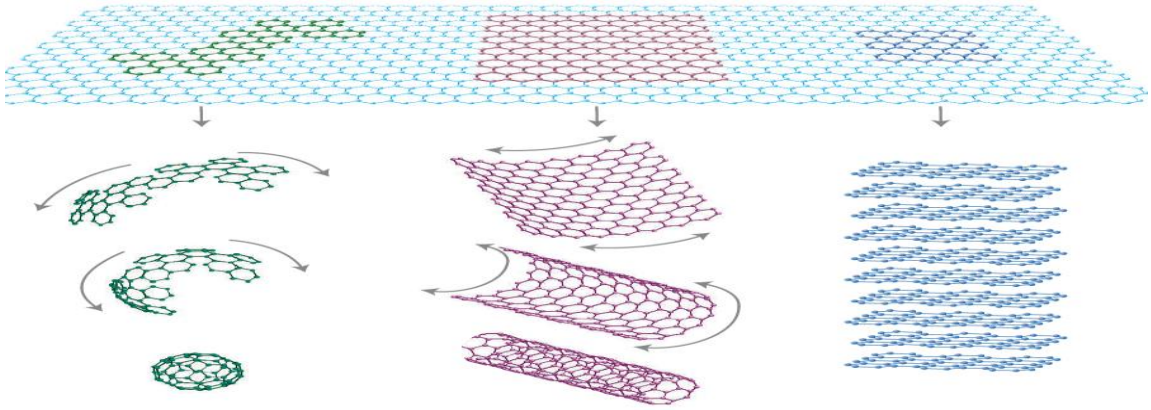

Figure (3-2): Graphene is the building block of many carbon allotropes; fullerenes, nanotubes and graphite, respectively [95].

In 2004, A. Geim and K. Novoselov used a very simple method to obtain graphene individual sheets, peeling a piece of graphite with an adhesive tape repeatedly till a single layer of graphene is obtained [96]. This opened the doors for a new era in nanotechnology. Graphene has matchless properties which make it fascinating for different applications. It is very thin, of high mechanical strength and flexibility, and is a transparent conductor. Its electrical conductivity may be modified either by the use of an electric field or by chemical doping. Graphene has very high electric mobility which makes it very useful in high frequency applications in electronics. Since graphene is considered one of the transparent conductors it can be utilized in applications as light panels, touch screens and solar cells. Flexible electronic devices, gas sensors and other biosensors are other possible applications [95], [97], [98].

In addition to the peeling process for obtaining graphene, different synthetic procedures have also been developed for its synthesis, including chemically modified graphene and graphene nanocomposites. Mechanical methods such as exfoliation of graphite in solutions can be divided into two main procedures; physical and chemical exfoliation. Physical exfoliation involves a simple peeling off process from graphite multi-layers using adhesive tape and relatively simple procedure. Alternatively, chemical oxidation of graphite with subsequent exfoliation can give rise to graphite oxide monolayer. Chemical treatment, however, can cause serious defects in the graphene structure; this can lead to disruption in the basic electronic structure of graphene changing it to a semiconductor material. Thus, physical exfoliation is preferable when it is required to maintain the graphene structure. Recent investigations have shown that defect-free graphene monolayer can be produced by the exfoliation of graphite in *N*-methyl-pyrrolidone as a solvent. Chemically synthesized G can be produced by the reduction of GO, using several reducing agents, Figure (3-3), [97], [98]. The reduction of GO to G can also be achieved by thermal or UV irradiation exposure. GO is produced by oxidation of graphite using different oxidants, e.g., nitric acid, concentrated sulfuric acid and potassium permanganate.. The G produced from reduction of GO is usually named reduced graphene oxide (RGO) which used in many publications interchangeably with the word Graphene [99].

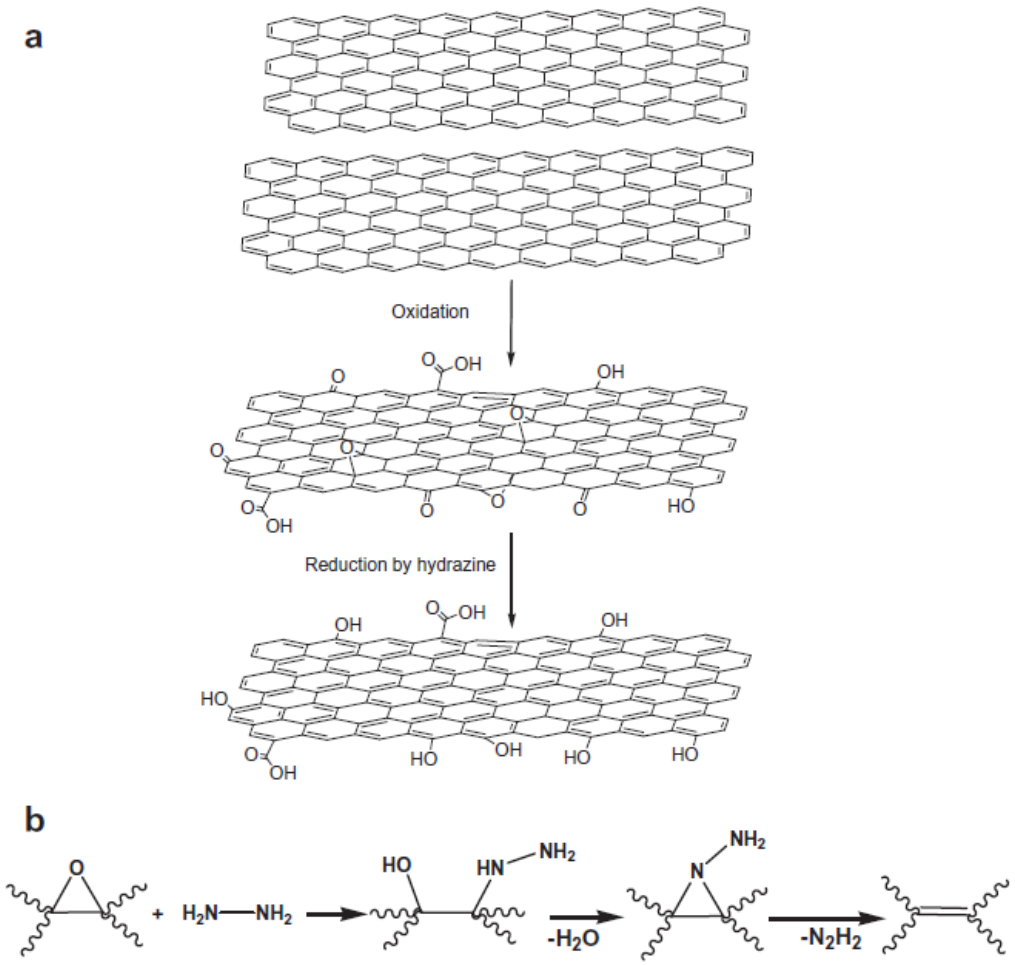

Figure (3-3): (a) Oxidation of graphite to form Graphene Oxide and its reduction back to Graphene. (b) A proposed mechanism for the reduction of GO using hydrazine [97].

On the other hand, Graphene Oxide (GO) can be used without further reduction due to its unique properties that are different than G. These properties include easy synthesis, matchless optical properties, high dispersability in a variety of solvents and the ability to attach different molecular species on its surface. The last two properties facilitate the deposition of different molecular structures on the surface of GO in solution with sufficient control over the formed structures. In addition, the cost of producing GO sheets is very small relative to the production of G and many other nanomaterials. These unique properties are highly advantageous in making nanocomposites of GO and metal oxides especially TiO_2-GO nanocomposites. The relatively higher hydrophilicity of GO, due to

the highly oxygenated surface, facilitates the dispersion of GO in the presence of an aqueous dispersion of TiO_2. This good dispersion is very difficult to achieve with G without adding a dispersant. Furthermore, the ability of the oxygenated functional groups of GO to chemically interact with the surface of TiO_2 leads to the formation of strong chemically bonded TiO_2-GO nanocomposites with superior properties [99], [100]. Regarding the structure of GO, it can simply be viewed as individual layers of G decorated with oxygen functionalities as ethers, hydroxyls, carboxyls, etc. The exact structure of GO is still uncertain due to the high hygroscopicity of dehydrated GO and the non-stoichiometric structure of GO. Various structural models of GO have been proposed over the past few years. These agree on the presence of oxygen containing functional groups on both the basal plane and edges of GO. Hydroxyl and epoxy functional groups are identifies to be the most abundant group on the surface of GO as illustrated in Figure (3-4) with minor amounts of other oxygenated functional groups as phenol, lactone, carboxy, carbonyl and quinones [99]–[103].

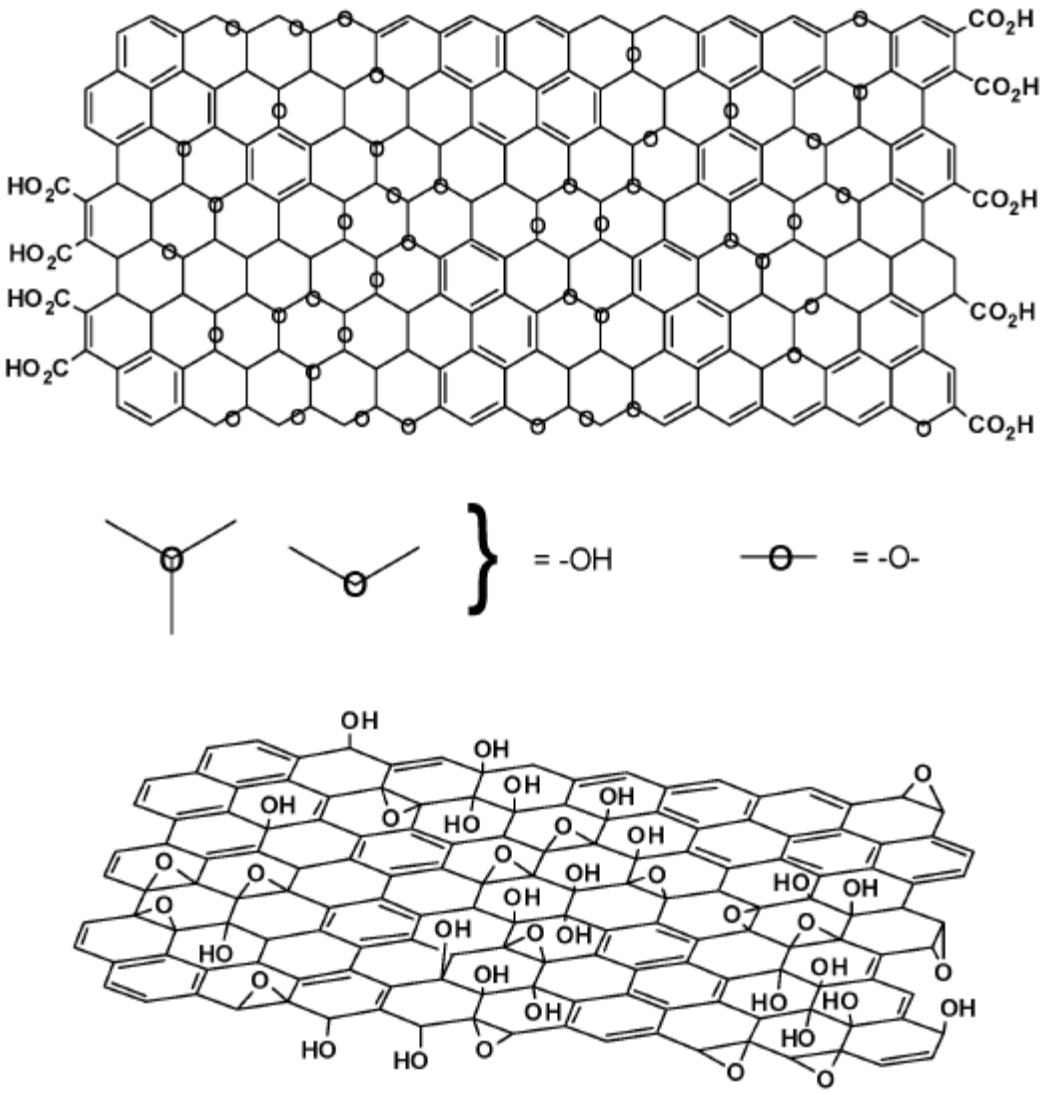

Figure (3-4) Different structural models for GO with carboxylic functional groups on the edges (above) and without the carboxylic groups (bottom) [100].

3.3. Perichromic probes:

Determining the surface properties of a catalytic material is relevant because these properties affect the adsorption/desorption processes on the catalyst surface, as well as the nature of the physicochemical processes taking place. In this respect, surface properties, such as the number, location and strength of acidic and basic sites on the surface, as well as surface polarity and surface polarizability play a crucial role in the activity of the catalyst and hence its applications [16], [64], [104]. A new technique

which is simple, reproducible, versatile and specific is the use of perichromic dyes usually referred as “probes” [16].

The ability to methodically determine the surface properties of a catalyst is a major challenge. Adsorption-desorption isotherms of different vapors such as NH_3, pyridine, CO and others are typically used to directly determine the acidic and basic sites on the catalyst surface. Other indirect methods include thermogravimetric analysis, X-ray spectroscopic techniques, Raman and FTIR, as well as acid/base titrations. Most of these methods require elaborate procedures, and most importantly do not allow direct determinations of surface empirical polarity and polarizability. A developing field for directly determining these properties is the use of perichromic probes.

Typically intramolecular charge transfer processes within these molecules are affected by the surrounding medium, this leads to change of the UV-visible absorption spectrum. The term solvatochromism is used to describe the effect of a solvent on the color of a certain probe.

However, this phenomenon is also observed with solids, therefore the general term perichromism is employed because it describes the effect of any medium on the probes’ color. There are two main types of perichromic phenomenon, positive and negative. Positive perichromism is observed when the dipole moment of the probe in the ground state is smaller than its dipole moment in the excited state. This will decrease the UV-Visible absorption energy causing a shift to longer wavelength as the surrounding medium polarity increases. On the other hand, the decrease in the wavelength of maximum absorption upon excitation of the probe with increase in the medium polarity is known as negative perichromism. Negative perichromism is attributed to the fact that the dipole moment of the probe in the ground state is larger than its dipole moment in the excited state [105]. The latter type is more common, as most perichromic dyes are zwitterions. The extension of perichromic probes to measure various surface properties is a recent, increasingly important application. It was found that the adsorption of the dyes onto surfaces leads to measurable changes in their UV-visible spectra. These changes could be correlated to the surface properties, including acidity, basicity, empirical polarity and polarizability. This approach represents a number of advantages such as the small amounts of the solids needed, simple measurement technique for UV-visible

spectral determination, reproducibility, high specificity, and versatility (the approach allows the determination of surface Lewis acidity, Lewis basicity, overall polarity and polarizability) [16], [106]. However, care must be taken to avoid the presence of surface impurities and to deposit a monolayer of the perichromic probe over the solid sample. Multi probe layers would lead to the probe molecules sampling each other not the sample surface [107]. Different perichromic probes are employed to determine surface properties. Among these probes, *tert*-butylstilbazolium betaine *(TBSB)*/*o,o'*-di-*tert*-butylstilbazolium betaine *(DTBSB)* homomorphic pair [108], [109] for determining surface Lewis acidity, 2,6-dichloro-4-(2,4,6-triphenylpyridinium-1-yl)phenolate (*WB)* [110] for determining surface polarity, and β-Carotene [111] for determining surface polarizability, have proven their efficiency, reproducibility and accuracy.

3.3.1. TBSB/DTBSB pair for determining surface acidity:

The medium can affect a chemical phenomenon (e.g., a reaction) by non specific interactions, as well as specific interactions, in particular hydrogen bonding. The medium acidity scale or hydrogen bond donor parameter can be evaluated using the visible spectrum of certain basic probes such as *tert*-butylstilbazolium betaine *(*TBSB*)* and its homomorph *o,o'*-di-*tert*-butylstilbazolium betaine *(*DTBSB*)* shown in Figures (3-5) and (3-6).

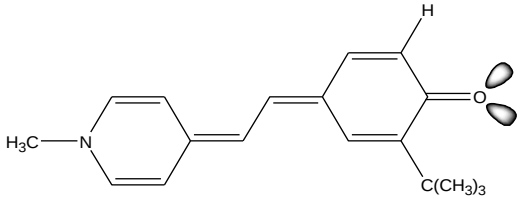

Figure (3-5) Chemical structure of *tert*-butylstilbazolium betaine (TBSB) [112].

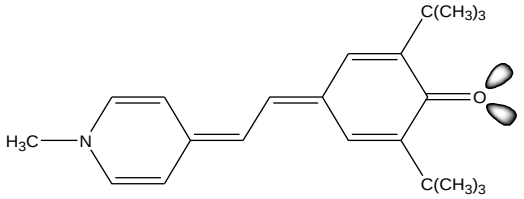

Figure (3-6) Chemical structure of *o,o'*-di-*tert*-butylstilbazolium betaine *(*DTBSB*)* [112].

TBSB is sensitive to medium acidity (due to H-bonding to the phenolate oxygen) as well as non-specific interactions. DTBSB on the other hand is sensitive only to non-specific interactions because H-bonding to its phenolate oxygen by the medium is sterically inhibited.

Catalàn et al used 50 non hydrogen bond donor solvents to correlate the absorption frequencies of TBSB and DTBSB in the form of equation (3-7) and used this correlation to determine the $\Delta\nu`$ of the sample using equation (3-8).

In order to normalize these values to obtain a surface acidity scale from zero to one, they assigned ethanol a value of 0.4 and derived the surface acidity (SA) parameter from equation (3-9).

However, all these data are obtained using solvents in the liquid state and another approximation is needed to fit the data to be applied in solid surfaces. The probe DTBSB and its homomorph TBSB can be used efficiently to measure the surface acidity of the medium provided that the phenolate oxygen is not protonated [108], [109], [112].

$$\nu'_{TBSB} = 1.4049\ \nu'_{DTBSB} - 6288.7 \qquad (3\text{-}7)$$

Where, ν'_{TBSB} and ν'_{DTBSB} is the absorption frequencies of TBSB and DTBSB, respectively.

The deviation in absorption frequencies from the straight line for any given sample, can be determined by:

$$\Delta\nu'_{sample} = \nu'_{TBSB} - (1.4049\ \nu'_{DTBSB} - 6288.7) \qquad (3\text{-}8)$$

Where $\Delta\nu`_{sample}$ is the deviation in absorption frequencies of TBSB and DTBSB, for any given sample, from the straight line equation (3-7).

$$SA = (\Delta\nu'_{sample}/\ \Delta\nu'_{ethanol}) * 0.4 = (\Delta\nu'_{sample}/1299.8) * 0.4 \qquad (3\text{-}9)$$

Where, SA is the normalized surface acidity and $\Delta\nu'_{ethanol}$ is the deviation in absorption frequencies of TBSB and DTBSB for ethanol.

Note that this treatment was developed for liquid solvents where, e.g., ethanol can be used as hydrogen-bond donor. This may be the case for solids, or a (solid) substance is needed as reference to measure surface acidity.

3.3.2. Determination of surface empirical polarity by WB:

The surface polarity of macromolecular structures plays a crucial role in their practical application. The interaction of two different materials as in the adsorption of macromolecules onto solid surfaces and the catalytic activity of metal oxides and composites materials depend mainly on the strength and nature of the intermolecular forces between the involved species. The term empirical polarity is typically used to explain these interactions. IUPAC defines polarity with regard to solvents as "all possible, nonspecific and specific, intermolecular interactions between solute ions or molecules and solvent molecules, excluding such interactions leading to definite chemical alterations" [113]. This definition can also be extended to solid surfaces. The empirical polarity is measured from UV-Visible spectra of the perichromic probe by converting the longest wavelength electronic transition of the probe to the corresponding intra-molecular charge-transfer energy (E_T) as calculated from equation (3-10).

$$E_T\,(\text{probe}),\ \text{kcal/mol} = 28591.5/\lambda_{max}\ (\text{nm}) \qquad (3\text{-}10)$$

Where, E_T (probe) is the intra-molecular charge-transfer energy of the perichromic probe, and λ_{max} is the wavelength of the maximum absorption of the perichromic probe.

2,6-dichloro-4-(2,4,6-triphenylpyridinium-1-yl) phenolate (*WB)* is one of the perichromic probes that can be used to measure the overall surface polarity. WB perichromism has been studied in pure solvents, solvent mixtures and solid surface. The presence of two chlorine atoms in the ortho position of the phenolate oxygen as presented in Figure (3-7), decreases its p*K*a to 4.78, thus the dye can still be used in the presence of traces of surface acidity. In addition, the lower hydrophobicity of WB makes it less prone to aggregate in solutions or at solid surfaces. This makes WB more suitable as a polarity probe in acidic environment than the corresponding diphenyl derivative, Reichardt's dye. The E_T values measured using WB dye is called $E_T(33)$ to differentiate it from the corresponding values measured by Reichardt's dye which is called $E_T(30)$. However, both are linearly correlated and both polarity scales can be used interchangeably [66], [107], [114]–[116].

The values of (E_T) of the perichromic probe are correlated to the specific and non-specific interactions of the medium as shown in equation (3-11),

$$E_T\,(\text{probe}) = \text{Constant} + a\alpha + b\beta + s(\pi^* + d\delta) \qquad (3\text{-}11)$$

Where, α value represents the acidity, the β value represents the basicity, the π^* value represents the dipolarity/polarizability effect of the medium, a, b, s are regression coefficient and dδ is a correction for π^*.

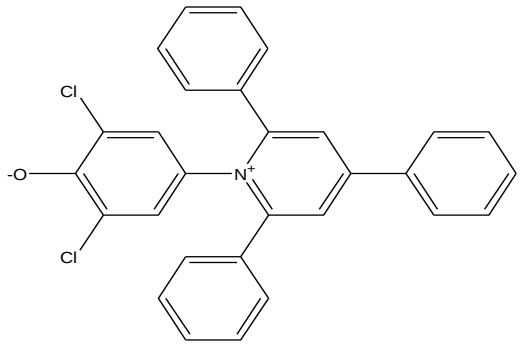

Figure (3-7) Chemical structure of 2,6-dichloro-4-(2,4,6-triphenylpyridinium-1-yl) phenolate (WB) perichromic probe.

3.3.3. Determination of surface polarizability by β-Carotene:

Solvent dipolarity/polarizability can be calculated from the perichromic behavior of different probes as shown in equation (3-11). However, the need to separate medium dipolarity from polarizability is very important in order to understand the van der Waals effects on various chemical interactions. Catalàn and Hopf used 3,20-di-tert-butyl-2,2,21,21-tetramethyl-3,5,7,9,11,13,15,17,19-docosanonaene (ttbp9), shown in Figure (3-8), to measure the solvent polarizability, and proceeded further to calculate the dipolarity term. The synthetic route to obtain ttbp9 is, however, a major synthetic undertaking, involving 15 steps! On the other hand, El Seoud et al proved that the natural dye β-Carotene can be employed for the accurate determination of the solvent polarizability. β-Carotene shown in Figure (3-9) has the same polyene part as ttbp9 hence can be used alternatively to study the same phenomenon. The availability, relatively low cost and accuracy in perichromic measurements suggest the use of β-Carotene to effectively measure the surface polarizability with high accuracy [111], [117]–[120].

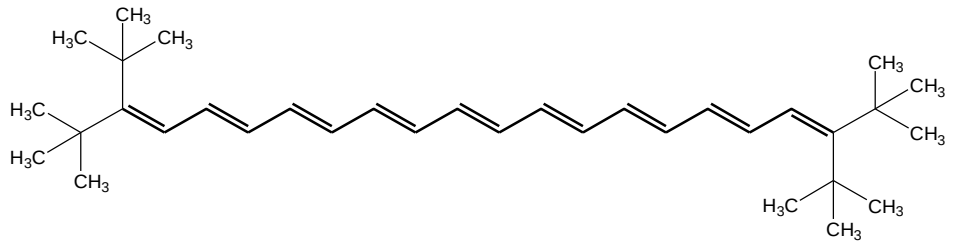

Figure (3-8) Chemical structure of ttbp9.

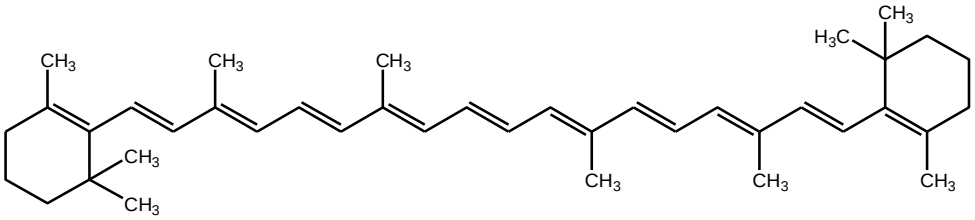

Figure (3-9) Chemical structure of β-Carotene.

3.4. Instrumentation:

3.4.1. NH_3-TPD (ammonia temperature programmed desorption) for determining surface acidity:

Temperature programmed desorption (TPD) is a chemisorption technique in which the adsorbing gas forms a chemical bond with its adsorption site. This type of interaction involves sharing of electrons between the adsorbing gas and the solid surface. The chemisorption process involves strong intermolecular interactions between the gas and the solid surface but the method is destructive for the sample. On the contrary, physisorption involves weak physical attraction, usually van der Waals forces, between the gas molecules and the solid surface with no detrimental impact on the structure or texture of the solid material. Physisorption is reversible so the solid sample can be recovered. Physisorption of nitrogen- or ammonia-TDP are the most frequent methods employed to determine surface area of solids by the BET (Brunauer-Emmett- Teller) method, see below. The number of adsorbed ammonia molecules is correlated to the number of acidic sites on the surface of the solid materials [121], [122]. A schematic diagram of NH_3-TPD instrument is shown in Figure (3-10).

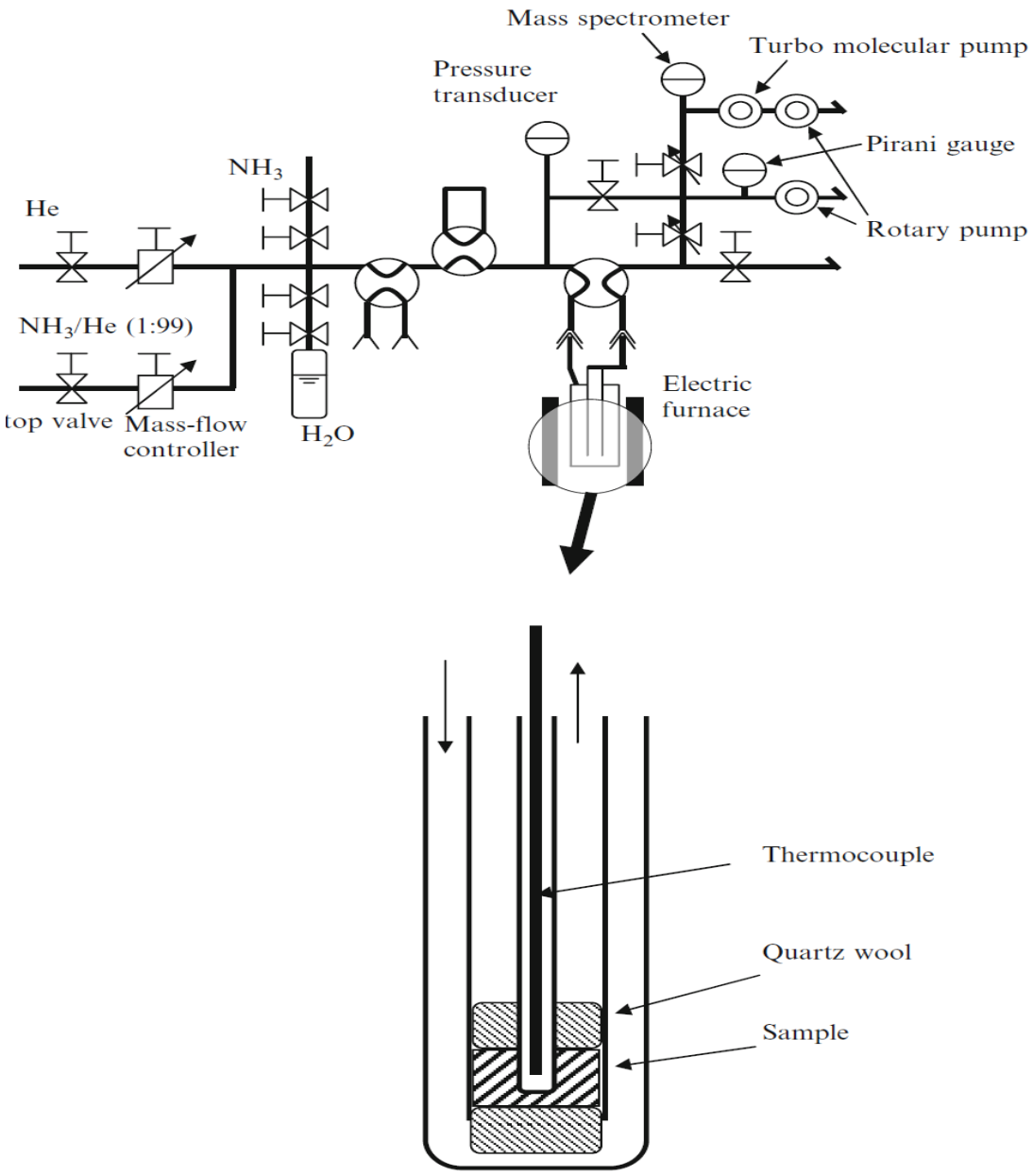

Figure (3-10) NH_3-TPD apparatus outline with illustration of sample cell composition [122].

NH_3-TPD can be used to measure the surface acidity of different metal oxides as TiO_2 and ZrO_2. However, it is not possible to discriminate between Lewis acidity and Brønsted acidity using NH_3-TPD only since NH_3 can interact with both acidic sites [62]. NH_3-TPD can be combined with other methods, to measure and quantify each type of acidity, such as FTIR, electron spin resonance (ESR) [62], ^{31}P magic angle spinning nuclear magnetic resonance (^{31}P MAS NMR) spectroscopy [63] and Infrared-Mass spectrometry (IRMS-

TPD). However, these methods are elaborate and their results in measuring surface acidity are questionable [64]. New, simple, accurate and reproducible method to determine Lewis and Brønsted acidity independently is crucial in the heterogeneous catalysis applications. Perichromic dyes provide these advantages in determining Lewis acidity.

3.4.2. Determination of surface area by the BET (Brunauer-Emmett-Teller) method:

In the physisorption of gaseous species onto solid surfaces, volume, temperature and pressure of the gaseous species play a role in the adsorption process together with the nature of adsorbent and adsorbate employed. The International Union of Pure and Applied Chemistry (IUPAC) classified pores according to their sizes into three types [123]:

A. Micropres: the pore width is less than 2 nm (20 A^o).
B. Mesopores: the pore width is between 2 nm and 50 nm.
C. Macropores: the pore width is more than 50 nm (500 A^o).

The adsorption isotherm is a plot between the amounts of adsorbate per gram of released adsorbent vs the relative vapor pressure P/P_o where, P is the vapor pressure of the adsorbent and P_o is the saturation pressure of pure adsorbent at the measurement temperature.

IUPAC classified the standard adsorption isotherms into six types which differ according to the gas-solid interaction as shown in Figure (3-11).

The reversible type I adsorption isotherm is exhibited by microporous solids with small external surfaces. It demonstrates that the pores are completely filled at relatively low pressure. The accessibility of the adsorbate molecules to the micropore volume controls the adsorption process.

The reversible type II adsorption isotherm is exhibited by macroporous or non-porous adsorbents. Unlimited monolayer-multilayer adsorption occurs. At B point, the monolayer adsorption is complete and the multilayer adsorption is about to start.

The reversible type III adsorption isotherm is typical of vapor adsorption on hydrophobic non porous materials as in the adsorption of water vapor on non-porous carbon. It is

characterized by the convexity throughout the isotherm relative to the pressure axis. In this case, the adsorbate- adsorbate interactions are much stronger than the adsorbent-adsorbate interactions.

The type IV adsorption isotherm is generally obtained for mesoporous solids. At low relative pressure, type IV isotherm takes the same shape as type II. The B point indicates that the monolayer adsorption is complete. The filling of the large pores by capillary condensation resulted in the appearance of the hysteresis loop associated to type IV isotherm.

The rare type V adsorption isotherm is similar to type III in that the adsorbate- adsorbate interactions are much stronger than the adsorbent-adsorbate interactions. Hysteresis loop is attributed to the capillary condensation of the large pores.

The type VI adsorption isotherm is given by uniform stepwise adsorption on a non-porous surface. The adsorption of argon on carbon black at -196^{o}C is an example of type VI adsorption isotherm [124], [125].

The identification of the type of the hysteresis loop is important to analyze the adsorption isotherms. Hysteresis loops are usually obtained from mesoporous solids due to capillary condensation. IUPAC classified the hysteresis loops into four main types as shown in Figure (3-12). Type H1 hysteresis loop is given by adsorbents with relatively uniform pores. The parallel and close adsorption-desorption branches is typical for type H1 hysteresis loop. (The) Type H2 hysteresis loop is associated with solids with complex pore structure of various shapes and sizes. The adsorption-desorption branches in type H2 hysteresis loop are wide with steep desorption and sloping adsorption branches. The adsorbed amount at any given relative pressure is always greater in desorption branch than the adsorption branch is common in both H1 and H2 hysteresis loops. Type H3 and H4 hysteresis loops are associated with slit-like pores and characterized by the absence of plateau at high relative pressure.

After measurement of the adsorption-desorption isotherm various mathematical models are used to calculate the surface area, pore volume and size distribution. Brunauer, Emmet and Teller (BET) developed an equation to calculate the specific surface area of solid materials. BET model assumes the multilayer adsorption of the gas molecules to be in a dynamic equilibrium where all the adsorption sites on the solid surface are equivalent

in energy and no lateral interactions exist between the gas molecules within the same layer [126], [127]. The specific surface area can be calculated using equation (3-12).

$$S_{BET} = n\, A_m\, N \qquad (3\text{-}12)$$

Where, $n = V_m/22414$ (V_m is the monolayer capacity), A_m is the molecular cross-sectional area occupied by the adsorbate monolayer per gram adsorbent and N is Avogadro's number.

The BET equation gives accurate values of the specific surface area in types II and IV isotherms. However, in types I and III isotherms the BET method cannot locate the B point and the actual surface area is not measured accurately.

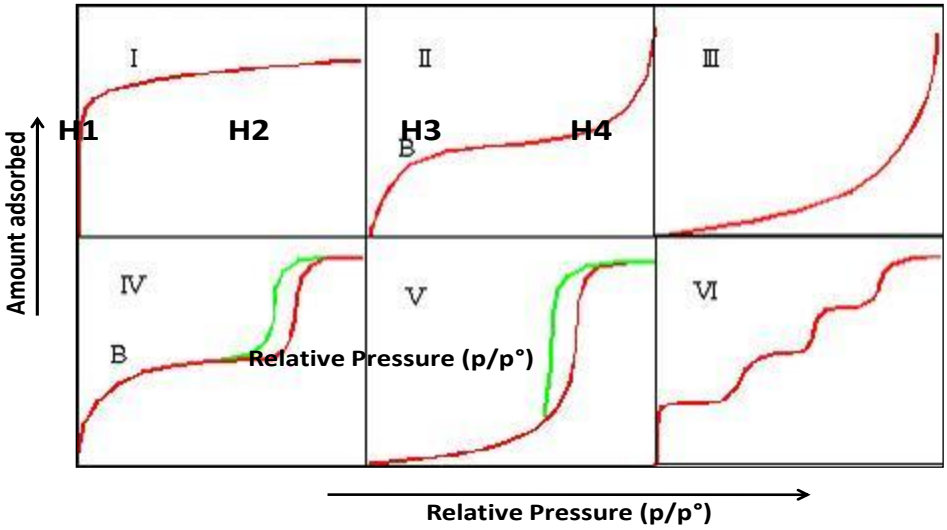

Figure (3-11) Different types of adsorption isotherms [125].

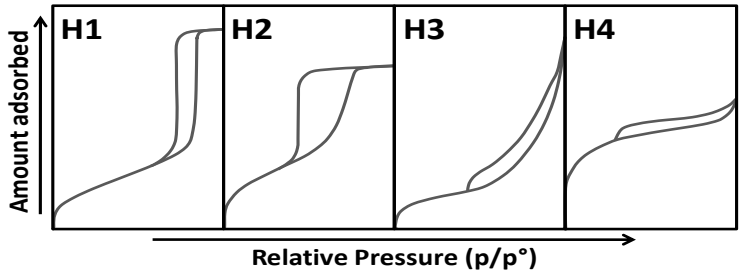

Figure (3-12) IUPAC types of hysteresis loops [124].

3.4.3. Spectroscopic methods to determine the chemical compositions, photocatalytic activity and intra-molecular charge transfer in the perichromic probes:

A- UV-Visible (UV-Vis) spectroscopy:

UV-Visible spectroscopy measures the absorption-reflectance of light in the UV-Visible region which involves electronic transitions from the highest occupied molecular orbital (HOMO) to the lowest unoccupied molecular orbital (LUMO) [128]–[130]. UV-Visible plots correlate the absorbance (A) of the radiation-absorbing species and the wavelength (λ). The wavelength at maximum absorption, λ_{max} can be used for qualitative identification of materials. The determination of the λ_{max} is required to calculate the intra-molecular charge transfer energies associated with the interaction of perichromic probes with different media, solid or liquid. On the other hand, quantitative determination of the sample concentration is calculated from the Beer-Lambert law, equation (3-13) [128]–[130].

$$A = \log I_o / I = abc \qquad (3\text{-}13)$$

Where, (A) is the absorbance, I_o and I are the intensities of incident and transmitted beam of light, respectively. In addition, (b) is sample path length in cm, (a) is the molar absorptivity in (l/mol.cm) and is constant for each compound under specific conditions.

This direct proportionality correlation between concentration (c) and absorbance (A) allows the determination of unknown concentrations of species based on calibration curves constructed using known concentrations. This direct proportionality is true only within a specific range of low concentrations. [128]–[130].

Irradiation of the UV-Visible radiation to a solid sample or film will cause the light to be reflected in all directions. The intensity of the reflected light can be measured and transformed to absorbance values using the Kubelka-Munk function. After identifying the reflectance wavelength, the same models can be used to obtain the sample concentration or transition energy. This is very useful in determining the reflectance values for solid

samples which can be used to calculate the band gap between reactive centers of metal oxide catalysts and their composites [131], [132].

B- Fourier transform infrared (FT-IR) spectroscopy:

The absorption of energy in the infrared region is ascribed to molecular vibrations and occurs at certain quantized frequencies. When the energy of these quantized frequencies matches the energy of the bond vibration within the molecule, energy is absorbed and the magnitude of the vibration is amplified. The absorption of the energy in the infrared region must be associated with change in the dipole moment of the molecule.

The vibrational frequency between two atoms is calculated from Hook's law, equation (3-14).

$$ύ = 1/2\pi c \sqrt{k/\mu} \qquad (3\text{-}14)$$

Where, ύ is the wavenumber in cm^{-1} , c is the velocity of light, k is the force constant and μ, is the reduced mass and is equal $(m_1+ m_2)/m_1 m_2$; m_1 and m_2 are the masses of two atoms.

According to Hook's law, the increase in bond strength increases the wavenumber i.e requires higher energy. This is exemplified in the triple bond absorption at 2300-2200 cm^{-1}, while the double bond absorbs at 1400-1600 cm^{-1}. In general, stretching vibrations requires higher energy and occurs at higher wavenumbers (shorter wavelengths) than the bending vibrations [128], [129].

C- Raman spectroscopy:

Raman spectroscopy is very powerful analytical tool in the qualitative and quantitative analysis of organic and inorganic materials. When a sample is irradiated with light of certain wavelength and polarization, typically in the visible or infrared regions, the light is scattered inelastically and the wavelength will shift with respect to the incident light beam. The inelastic (Raman) scattering of light will cause a change in the wavelength and intensity of light which is measured and analyzed to obtain the Raman spectrum [128]–[130].

The Raman spectrum is a plot between the wavenumbers corresponding to the Raman shifts and the relative intensities of interaction between light photons and the molecular vibration. If the Raman scattered photon exhibits lower energy than the incident light, the frequency decreases and known as *Stokes* emission. On the other hand, if the scattered photon exhibits higher energy than the incident light, the frequency increases and known as *anti-Stokes* emission as shown in Figure (3-13). The energy of the scattered photon (E) is calculated from equation (3-15).

$$E = h\upsilon_0 \pm \Delta E_\upsilon \qquad (3\text{-}15)$$

Where, h is Plank's constant, υ_o is the frequency of the incident radiation and ΔE_υ is the change in energy.

Raman scattering has number of limitations; the Raman signal is very weak compared to the intense Rayleigh scattered light which decreases the detection limit. In addition, photoluminescence interference may occur which can obscure the Raman signals. However, Raman signals are less susceptible to water interference which is a major drawback for the IR spectroscopy.

Raman spectrum may be used as fingerprint to identify unknown molecules. In addition, the sensitivity of Raman to surface structural change makes it very useful technique in the field of surface chemistry and in studying composite materials [128]–[130].

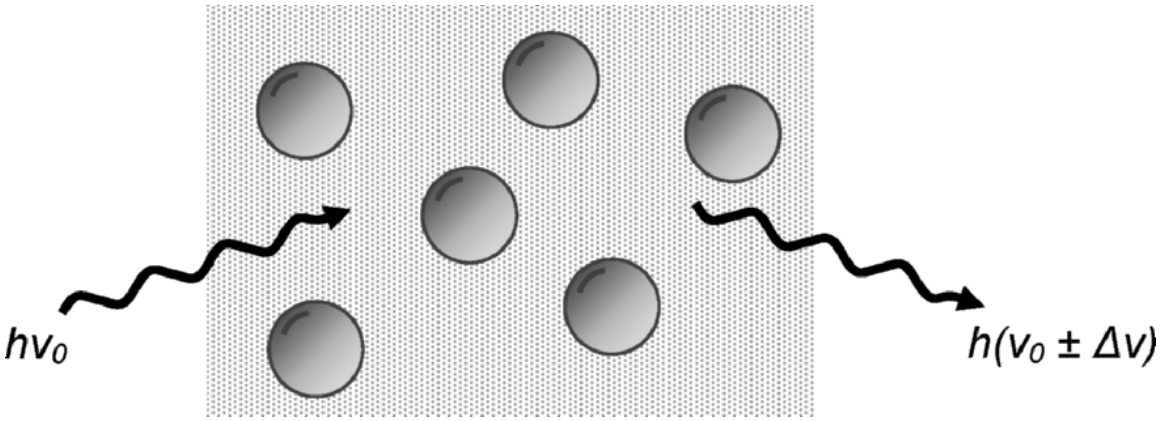

Figure (3-13) Raman scattering from solid particles where, $\Delta\upsilon$ is the change in frequency, $\upsilon_o - \Delta\upsilon$ represents the *Stokes* emission and $\upsilon_o + \Delta\upsilon$ is the *anti-Stokes* emission [130].

3.4.4. ***Crystal phase structure determination using X-Ray Diffraction (XRD):***

XRD is used for obtaining information about the crystal structure of materials. The technique involves the use of X-ray irradiation to interact with a crystalline sample to produce a diffraction pattern, which can then be used to elucidate the structure and phase of the crystalline material. X-ray wavelength values range from 0.1 to 10 nm which correspond to the distances between units in crystalline materials. When X-ray radiation falls on a crystalline sample, the radiation will be elastically or inelastically scattered in different directions and with different degrees of interference leading to constructive or destructive diffraction.

For the case of symmetrical arrangement of units in the crystal structure, these units are arranged in parallel planes with specific *d* distance between theses planes. Diffracted rays can then interfere constructively under certain geometric conditions expressed by Bragg, equation (3-16):

$$n\lambda = 2d \sin\theta \qquad (3\text{-}16)$$

Where, *n* is an integer, λ is the wavelength of the incident monochromatic X-ray beam, *d* spacing between crystal planes and θ is the incident angle.

This means that this constructive interference will produce a consolidated diffracted beam when the difference in light path length $2d\sin\theta$ equals an integer multiple of the wavelength as shown in Figure (3-14).

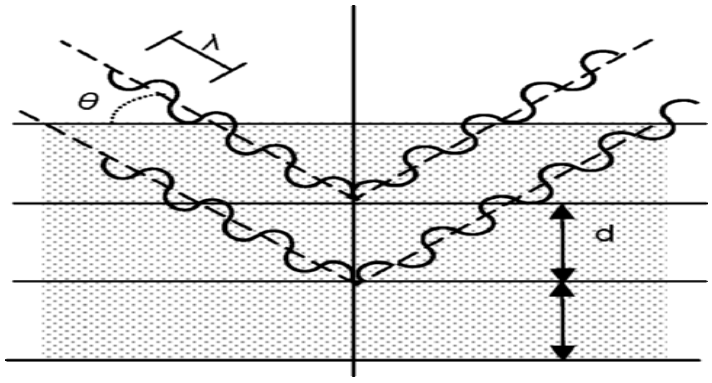

Figure (3-14) The main components of Bragg's law [130].

The resultant XRD diagram is a plot of diffraction intensities versus the angle 2θ giving the crystal diffraction pattern. Each peak indicates the spacing of specific set of crystal planes. Although XRD is widely used for structure determination of nanomaterials, it cannot be used for amorphous materials as XRD requires highly ordered crystal structure in order to extract useful information. In addition, mixture of phases with low symmetry will have large number of diffraction points leading to poor differentiation between the different phases [130].

TiO_2 has 3 main crystal phases which are anatase, rutile and brookite with anatase having the highest photocatalytic activity among these phases. XRD can successfully differentiate between these phases as shown in Figure (3-15) due to presence of different diffraction bands [91].

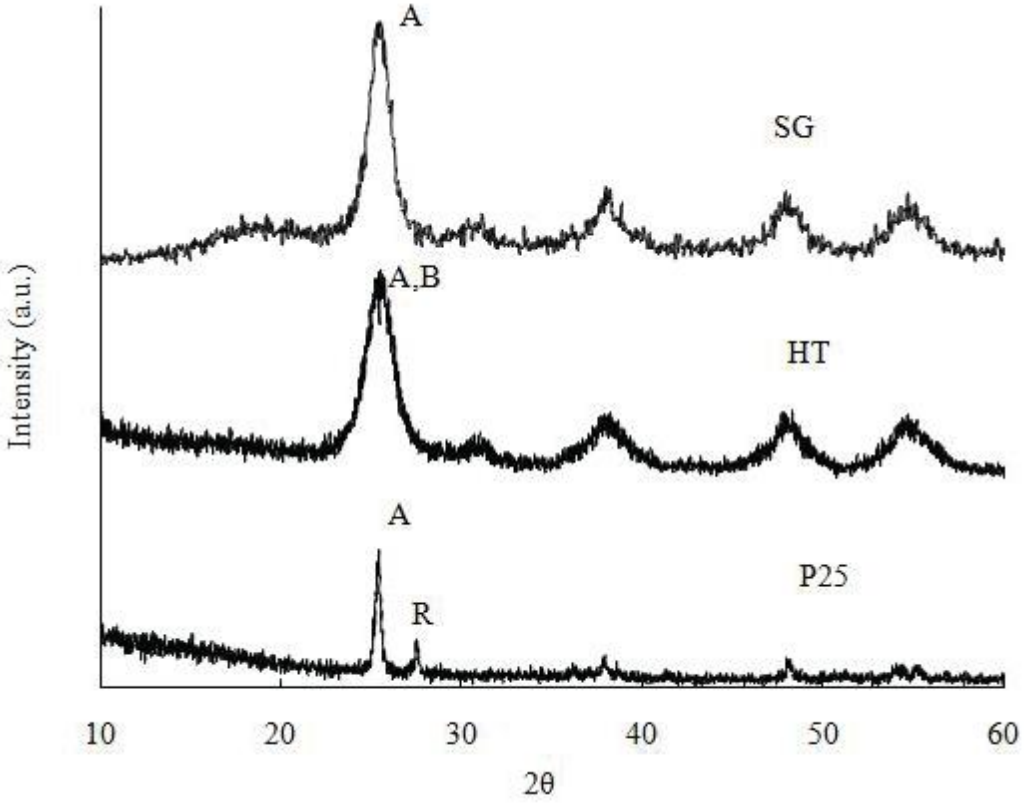

Figure (3-15) XRD spectra for TiO_2 from different sources SG (synthesized by sol-gel method), HT (synthesized by hydrothermal method) and P25 (commercial TiO_2) that have different crystal phases: A (anatase), B (brookite) and R (rutile) [91].

3.4.5. *Scanning Electron Microscopy (SEM) for Morphology determination:*

Electron microscopy relies on the interaction between matter and a beam of high energy electrons giving measurable signals which can be used to obtain information about chemical composition, topography, crystallographic structure and morphology. Hence, this technique is routinely used for characterization of solid surfaces [130].

Electron microscopes have the same principles as optical microscopes as they both consist of source of illumination and magnification lenses. However, electron microscopes utilize highly energetic electron beams that are focused using an electromagnetic field. Scanning Electron Microscopy (SEM) is one such technique, with the equipment typically composed of an electron beam source (an electron gun) with the produced electron beam focused towards the sample using a series of electromagnetic lenses to control the direction of the electron beam as shown in Figure (3-16) [130], [133], [134].

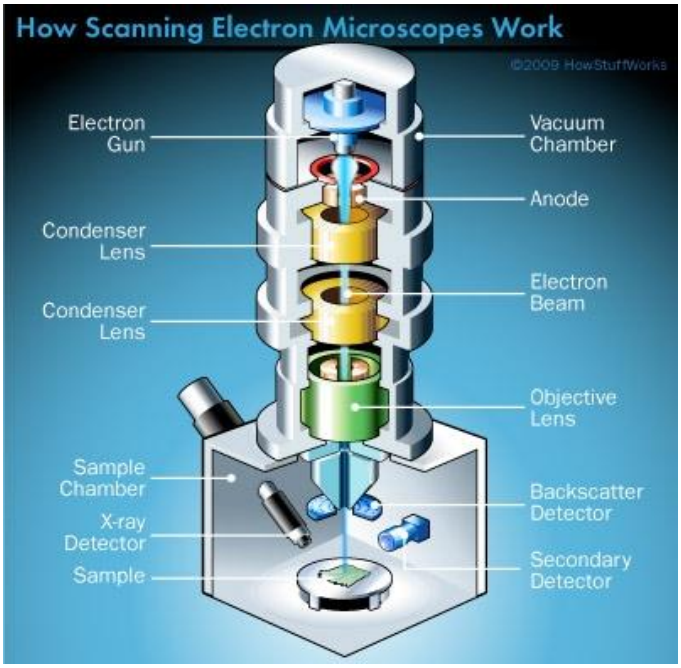

Figure (3-16) The basic components of SEM [133].

The produced electron beam will hit the sample placed in the sample chamber. Primary electrons, from the incident electron beam, will interact with the sample to produce secondary electrons (SEs) from the sample surface or back scattered electrons (BSEs) of lower energy which are detected and amplified to produce the image. SEs are usually used to obtain topographical data since they are primarily originate from the surface while, BSEs can detect difference in chemical compositions which is very useful for nanocomposites characterization. Hence, structural, compositional, topographical and crystallinity information can be obtained using SEM. Other signals produced from the primary electron beam include Auger electrons, X-ray and visible light photons as shown in Figure (3-17). On the other hand, transmitted electrons requires very thin sample to be observed which is utilized in Transmission Electron Microscope (TEM) [134].

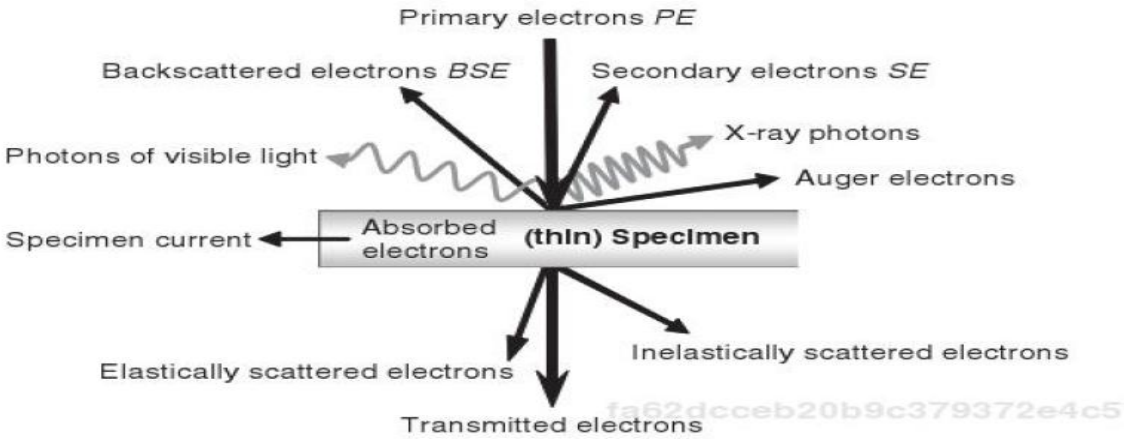

Figure (3-17) Some signals that are produced when a sample interacts with an electron beam [134].

The SEM sample must be clean and conductive or else, the charge accumulation within the sample will affect the image generation. Non conductive samples are covered with a thin layer of conductive material, e.g., gold or platinum. Other samples such as biological specimens may need further preparation as dehydration or freeze drying before they subjected to the electron beam [134]–[136]. Vacuum is needed during the production of electrons and through the whole SEM process to decrease the contamination and scattering of the produced electrons by the air particles.

SEM is very useful in the examination of nanoscale materials due to the high resolution of SEM images and the ability of examining objects with different magnifications. In addition, the three-dimensional images give better information about the sample due to greater depth of focus of the SEM. On the other hand, SEM has many drawbacks such as the limited size of sample and the inability to image samples that are destroyed in the high vacuum [136].

Chapter (4)

Materials and Methods

4.1. ***Materials:***

Titanium (IV) ethoxide [$Ti(OEt)_4$], TritonX-100, MB azo dye and absolute ethanol were purchased from Sigma-Aldrich. G and GO were obtained from ACS Material-USA. The G is single layer material with purity >99%, surface area = 650-750 m^2/g (BET), and lateral size = 0.5-5 μm. A 99% pure GO sample was employed: diameter: 1-5 μm, thickness: 0.8-1.2 nm, single layer ratio: 99% and C/O atomic ratio: 1.67.

The perichromic probes used to measure the surface properties of the composites were kindly provided by Prof. Omar A. El Seoud, Institute of Chemistry at the University of São Paulo. The used perichromic probes were synthesized as reported elsewhere and included 2,6-dichloro-4-(2,4,6-triphenylpyridinium-1-yl)phenolate (*WB)* [110] to determine surface empirical polarity, *tert*-butylstilbazolium betaine *(TBSB)*/*o*,*o'*-di-*tert*-butylstilbazolium betaine *(DTBSB)* pair [108], [109] to determine surface Lewis acidity, and β-Carotene [111] to determine surface polarizability. DI was produced from Millipore Milli-Q water purification system. All other materials were used as received.

4.2. ***Equipment:***

The following equipment was employed:

- Thermolyne type 48000 furnace for calcinations.
- Thermoscientific Heratherm oven for drying.
- Sonicator (VWR Int. – model P250HT).
- Centrifuge (Fischer Scientific Centric centrifuge – model 225).
- Dynamic light scattering (DLS, Ver. 6.32 Zetasizer of Malvern Instruments Ltd).
- X-ray Diffraction (XRD, D8 Bruker x-ray powder diffractometer).
- Field Emission Scanning Electron Microscope (FESEM, JEOL JSM-7401F).
- Fourier Transform Infrared Spectroscopy (FTIR, Thermo-scientific Nicolet 380).
- Raman Spectroscopy (ProRaman-L, Enwave Optronics, Inc.).
- N_2 physisorption porosity analyzer (Micromeritics ASAP 2020).
- UV–Visible Spectrophotometer (Shimadzu UV 2550).
- Spectronic 20D+ UV-Visible spectrophotometer (Thermoelectron Co.).

- Temperature Programmed Desorption (TPD, Micromeritics ChemiSorb 2750 pulse chemisorption system analyzer)

4.3. Sample preparation:

4.3.1. Large particle size TiO_2 nanoparticles:

TiO_2 nanoparticles were synthesized using a Sol-Gel method as reported elsewhere [137]. Absolute ethanol, 100 mL, was added to 20 mL of titanium ethoxide, and the mixture was stirred at 600 rpm for one hour. A volume of 50 mL of DI was then added to the previous mixture under vigorous stirring. After 16 hours under vigorous stirring the formed Sol was sonicated for 10 minutes, washed with DI several times, to remove ethanol, and filtered. The obtained filtrate was then dried at 80^{o}C to constant weight.

4.3.2. Small particle size TiO_2 nanoparticles:

A portion of the resulting sample was then subjected to careful grinding and sieving using a USA standard sieve series of 106μm mesh (Newark Wire Cloth Co.) with the aim of reducing the particle size and particle size distribution. The decrease in particle size and particle size distribution was confirmed using DLS. Both these samples were then calcinated at 300^{o}C for 3 hours.

4.3.3. TiO_2-G nanocomposites:

TiO_2-G nanocomposites were prepared by adding different amounts of G to the same mass of TiO_2. This was conducted as follows:

- The nonionic surfactant (TritonX-100; ethoxylated octylphenol) was sonicated with 50 mL DI, followed by the addition of G to form a G suspension.
- A mass of about 2 g of pre-calcined TiO_2 was added to 75 mL of DI and sonicated for 30 minutes. Both larger and smaller particle-sized pre-calcined TiO_2 were used.
- The formed TiO_2 suspension was then rapidly added to the G suspension and sonicated for another 30 minutes.

- The formed product was filtered and washed with 2 L of DI to remove excess surfactant. It was dried at 80^{o}C to constant weight and calcinated at 300^{o}C for 3 hours.

This procedure was used to prepare a series of TiO_2-G nanocomposites for each of the two TiO_2 samples, the large particle-sized and the small particle-sized. To this end, the mass of G and the volume of TritonX-100 used were varied to lead to samples with G weight content of 0.25%, 0.5%, 1%, 1.5%, 2% and 2.5%. In this respect, 5mg, 10mg, 20mg, 30mg, 40mg and 50 mg of Graphene were used respectively, with 2mL, 2mL, 3mL, 3mL, 4mL and 4mL of the surfactant.

4.3.4. TiO_2-GO nanocomposites:

TiO_2-GO nanocomposites were prepared by adding different amounts of GO to the same mass of TiO_2. This was conducted as follows:

- GO was sonicated with 75 mL DI, to form a suspension.
- A mass of about 2 g of pre-calcined TiO_2 was added to 50 mL of DI and sonicated for 30 minutes. Both larger and smaller particle-sized pre-calcined TiO_2 were used.
- The formed TiO_2 suspension was then rapidly added to the GO suspension, sonicated for another 90 minutes, followed by stirring at 600 rpm and room temperature for 18 hrs.
- The formed product was filtered then dried at 80^{o}C to constant weight, followed by calcination at 300^{o}C for 3 hours.

This procedure was used to prepare a series of TiO_2-GO nanocomposites for each of the two TiO_2 samples, the large particle-sized and the small particle-sized. To this end, the mass of GO used entailed 5mg, 10mg, 20mg, 30mg, 40mg and 50 mg to results in samples with GO weight content of 0.25%, 0.5%, 1%, 1.5%, 2% and 2.5% respectively.

4.3.5. Sample coding:

The samples prepared as explained above were coded. The codes consist of three parts: particle size of TiO_2, followed by the type of the added nanocarbon filler, then the % of these nanofillers. The particle size of TiO_2 is abbreviated TL for large particle-sized TiO_2

nanoparticles and TS for small particle-sized TiO_2. The sample codes are listed in Table (4-1).

Table (4-1) List of the samples codes

TiO_2 particle size	Nano filler	Amount of G/GO	Sample Code
Small Particle Size TiO_2	Graphene	0.25%	TS-G-0.25
		0.50%	TS-G-0.50
		1.00%	TS-G-1.00
		1.50%	TS-G-1.50
		2.00%	TS-G-2.00
		2.50%	TS-G-2.50
	Graphene Oxide	0.25%	TS-GO-0.25
		0.50%	TS-GO-0.50
		1.00%	TS-GO-1.00
		1.50%	TS-GO-1.50
		2.00%	TS-GO-2.00
		2.50%	TS-GO-2.50
Large Particle Size TiO_2	Graphene	0.25%	TL-G-0.25
		0.50%	TL-G-0.50
		1.00%	TL-G-1.00
		1.50%	TL-G-1.50
		2.00%	TL-G-2.00
		2.50%	TL-G-2.50
	Graphene Oxide	0.25%	TL-GO-0.25
		0.50%	TL-GO-0.50
		1.00%	TL-GO-1.00
		1.50%	TL-GO-1.50
		2.00%	TL-GO-2.00
		2.50%	TL-GO-2.50

4.4. Characterization of TiO_2 and TiO_2-G/GO nanocomposites:

Sample characterization was carried out as follows:

- The particle size of TiO_2 was measured using DLS using 12 mm square glass cell at 25^oC for 70 seconds.
- The crystal phase structure of the formed TiO_2 and TiO_2-G/GO nanocomposites was examined using X-ray Diffraction (XRD) operated at 40 kV and 30 mA using a copper (Cu) target with K_α, λ = 0.1542 nm. The XRD spectra of the pristine samples were obtained for a 2θ range between 3^o and 80^o (step size: 0.030^o and step time: 3 seconds).
- The morphology of the formed TiO_2-G/GO nanocomposites was determined by field emission scanning electron microscope (FESEM) providing ultra high resolution (1.5nm at 1kV) and employing a cold Tungsten single crystal conical electron gun and a conical highly excited magnetic field objective lens with low aberration. FESEM was equipped with three Electron Detectors and a digital camera: Upper secondary electron in-lens (SEI), Lower secondary electron (LEI), Retractable backscattered electrons detectors (RBEI) and IR camera.
- The structural characteristics of TiO_2 and TiO_2-G/GO nanocomposites were investigated using FTIR and Raman Spectroscopy, the latter using 532 nm excitation laser. FTIR samples were prepared using spectroscopic grade KBr to form pellets using a ratio of 1:100 (sample weight: KBr weight).
- BET (Brunauer-Emmett- Teller) surface area and the average pore diameter were measured using N_2 physisorption porosity analyzer. High purity (99.99%) nitrogen was used to measure nitrogen adsorption isotherms at 77.4 K. The samples were degassed below 50 μm Hg at 30°C for 30 min, and then heated at 30°C for TiO_2-GO and at 200°C for TiO_2-G, for 600 minutes.
- Double beam UV–Vis spectrophotometer (Shimadzu UV 2550) equipped with model IST-204A integrating sphere reflectance attachment was used to measure the diffuse reflectance (UV–Vis DRS) spectra of TiO_2 and TiO_2-G/GO nanocomposites.

- Surface acidity of the TiO_2 and TiO_2-G/GO nanocomposites was determined using Temperature Programmed Desorption (TPD) of ammonia gas (NH_3) as the basic probe molecule. A sample of ca. 0.1g was treated near its calcination temperature (280^oC) under helium flow (20 mL/min) for 60 minutes and then saturated with a 15% NH_3/He mixture flow for 30 minutes. After purging with the helium for 1 hour to remove weakly physisorbed NH_3, the sample was heated to 1100^oC at a rate of 10^oC/min under helium flow (20 mL/min). The amount of acidic sites in μmol/g of the sample surface was calculated from the desorbed amount of NH_3. For broad desorption peaks, the areas of sub-peaks were added to each other to calculate the total amount of acid sites after separating the main peak into many sub-peaks by using the Fityk program for peak fitting [138].

4.5. Characterization of TiO_2 and TiO_2-G/GO nanocomposites using perichromic probes/dyes:

Mixtures containing 0.025 g of the sample, and 1mL of a solution of the perichromic probe (WB, TBSB, DTBSB and β-Carotene) in acetone (2×10^{-3} mol L^{-1}, 1×10^{-3} mol L^{-1}, 1×10^{-3} mol L^{-1} and 2×10^{-3} mol L^{-1}, respectively) were prepared in glass vials equipped with screw-cap covers. Care was exercised in order to minimize the absorption of any atmospheric moisture by sealing the glass vials with Parafilm. The vials were closed and the mixtures were magnetically stirred at room temperature and 400 rpm for 1 hour. The probe-containing thin solid layers were prepared on 2 cm×2 cm quartz plates, carefully cleansed as described elsewhere [139], using a long-tip disposable pipette. The thin solid layers were dried for 30 min under reduced pressure, over P_4O_{10}, stored in a desiccator and thin solid layer reflectance was measured immediately. The reflectance was recorded at room temperature by using UV–Vis DRS. $BaSO_4$ was used as reference. A Shimadzu UV-Probe, version 2.21 program, was used for the conversion of the reflectance spectra into the corresponding absorption curves. Origin 6.0 software was used for the calculation of the values of λ_{max} from the first derivative of the spectra.

4.6. Photocatalytic decomposition of MB using TiO_2 and TiO_2-G/GO nanocomposites:

A weight of about 0.2g of the sample was stirred at 300 rpm in 200 mL of MB 5 ppm (1.57×10^{-5} mol L^{-1}) aqueous solution for 60 minutes in the absence of light to allow MB adsorption onto the sample surface and equilibrium be reached. The mixture was then irradiated at λ=365 nm, using a fluorescent F8T5/BLB (Blacklight Blue) lamp, with continuous stirring at 300 rpm to avoid settling of the sample particles and ensuring constant exposure to the radiation.

Analysis of the remaining MB in the solution was determined by taking aliquots at regular intervals from the solution, centrifuging them at 400 rpm for 5 minutes, then measuring the visible absorption spectra of the clear solutions at 664 nm, the main absorption peak of MB, using a Spectronic 20D+ UV-Visible spectrophotometer. The solution concentration was then determined using pre-constructed calibration curve included in Appendix II.

The concentration of the remaining MB in the solution was determined using the slope of the corresponding calibration curve as shown in equation (4-1) where, A is the absorbance at 664 nm and C is the standard dye concentration in mole L^{-1}. The calibration curves were constructed using the absorbance of fixed concentrations of MB dye solution. The zero order rate constants were calculated from the slope of the linear relationship between the remaining dye concentration (in mole L^{-1}) and the photocatalytic degradation time (in minutes) for each sample.

$$A = 0.0458^{*} C,\ r^2 = 0.9936 \qquad (4\text{-}1)$$

Chapter (5)
Results and Discussion

This chapter is discussing the findings of this work and each sample set is discussed separately. In order to facilitate the reading, each sample set is presented as "stand alone" item, so that the reader does not have to go back-and-forth between sections of the discussion in order to follow the argument. We hope that the repetitions resulting from this presentation style will be compensated by the comfort of reading.

5.1. Particle size determination:

The preparation of TiO_2 blank samples involved the addition of DI in the hydrolysis step. However, the addition rate of DI affected the average particle size and particle size distribution of the produced nanoparticles. Dropwise addition of DI resulted in the formation of nanoparticles with wider size distribution compared to the addition of DI instantaneously as confirmed by DLS. The dropwise addition of DI produced nanoparticles with 477 nm average particle size and 107 nm particle size distribution as shown in Figure (5-1). The immediate addition of DI produced nanoparticles with 436 nm average particle size and 59 nm particle size distribution as shown in Figure (5-2).
Additionally, sieving was successfully used to decrease the average particle size and size distribution of the TiO_2 blank samples. The particle size of the TiO_2 blank samples, determined using DLS and was found to be 436 ±59 nm and 251 ±32 nm for the TL and TS samples, respectively as shown in Figures (5-2) and (5-3).

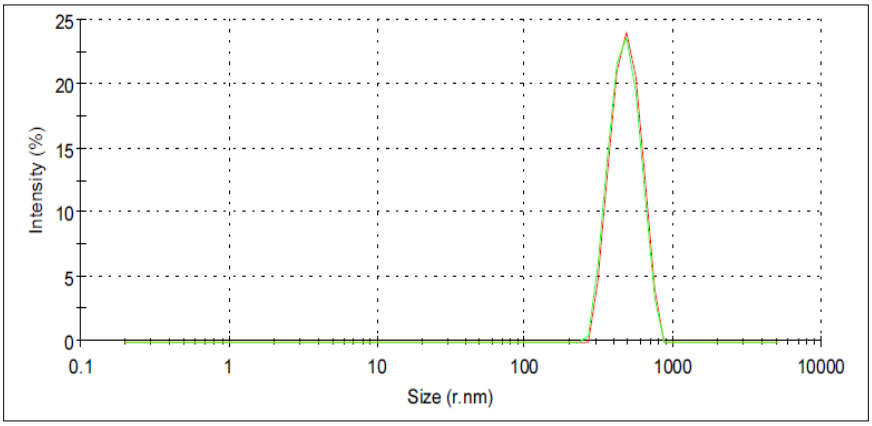

Figure (5-1) Average particle size and size distribution of the TiO_2 nanoparticles prepared by dropwise addition of DI as measured by DLS.

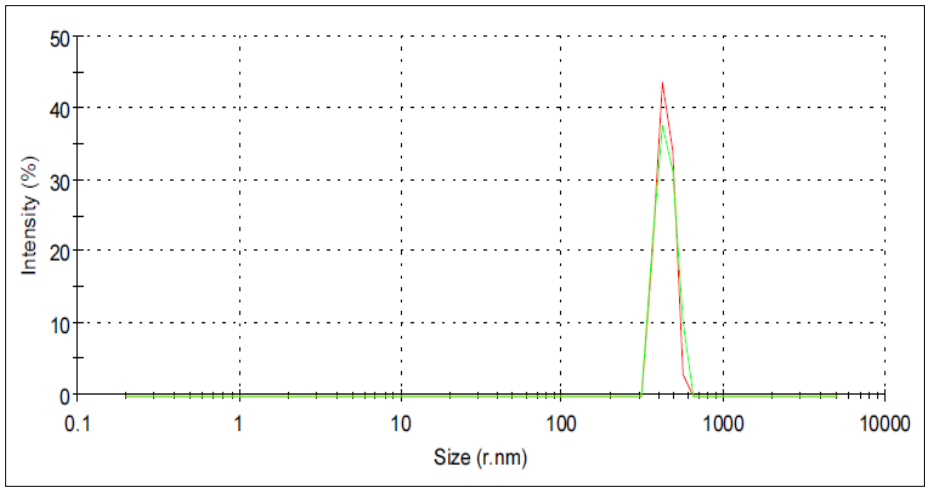

Figure (5-2) Average particle size and size distribution of the TL samples as measured by DLS.

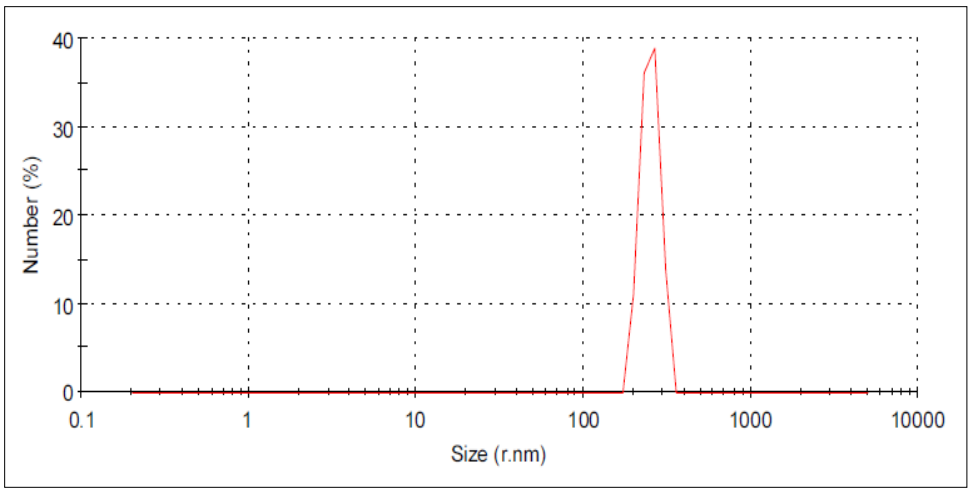

Figure (5-3) Average particle size and size distribution of the TS samples as measured by DLS.

5.2. T small-GO (TS-GO) nanocomposites:

5.2.1. Surface acidity:

J. Catalàn developed a solvent acidity SA scale based on the solvatochromism of the *o*-*tert*-butylstilbazolium betaine dye (TBSB)/*o*,*o*`-di-*tert*-butylstilbazolium betaine dye (DTBSB) homomorph pair, previously shown in Figures (3-5) and (3-6).

Equation (5-1) used to calculate the surface acidity using the TBSB/DTBSB perichromic pair developed by Catalàn where, ν` is the absorption maximum in cm^{-1} using UV/Vis spectroscopy.

$$\Delta\nu'_{sample} = \nu'_{TBSB} - (1.4049\ \nu'_{DTBSB} - 6288.7) \quad (5\text{-}1)$$

However, this equation is developed using 121 solvents and compared to other acidity parameters previously reported as α of Kamlet and Taft and acceptor number AN of Gutamann to show that TBSB/DTBSB pair can be used to measure the solvent acidity [112]. A similar approach can be used to estimate the surface acidity of solids since the TBSB/DTBSB dye pair is sensitive to Lewis acidic sites provided that the dye is adsorbed on the solid surface as monolayer to avoid the interaction between the dye molecules. This means that the main factor that will affect the change in λ_{max} of the dyes is the surface Lewis acidic sites on the surface of the solid [112], [140].

There are two types of acidic sites on the surface of TiO_2. The first is Lewis acidic sites which are attributed to the Ti^{+n} cations present on the surface of the TiO_2 nanoparticles. The other type is the Brønsted acidic sites which is explained by the presence of surface hydroxyl groups usually bridged between Ti atoms in the form of Ti-O(H)-Ti [141]. Harima et al reported that the blank TiO_2 contain high number of Lewis acidic sites [141]. This is relevant to our results represented in Figure (5-4) which shows that the blank TS have higher Lewis acidic sites than TS-GO samples. This behavior can be attributed to the formation of Ti-O-C covalent bonds between TiO_2 and GO in the formed nanocomposites as proved by DRS-UV, FTIR and Raman spectroscopy results. The Ti-O-C bonds will decrease the number of Ti^{+n} cations on the surface of the nanocomposites leading to overall decrease in the number of Lewis acidic sites. The increase in the GO amount will further decrease the number of Ti available Lewis acidic sites leading to linear decrease in the Lewis acidity, as measured using the perichromic dyes, with

increasing GO content in the nanocomposites. The slight increase in the Lewis acidic sites associated with TS-GO-2.50 sample may be due to stacking of GO layers in higher concentrations [43] leaving more surface Ti^{+n} atoms available for interaction as Lewis acidic sites.

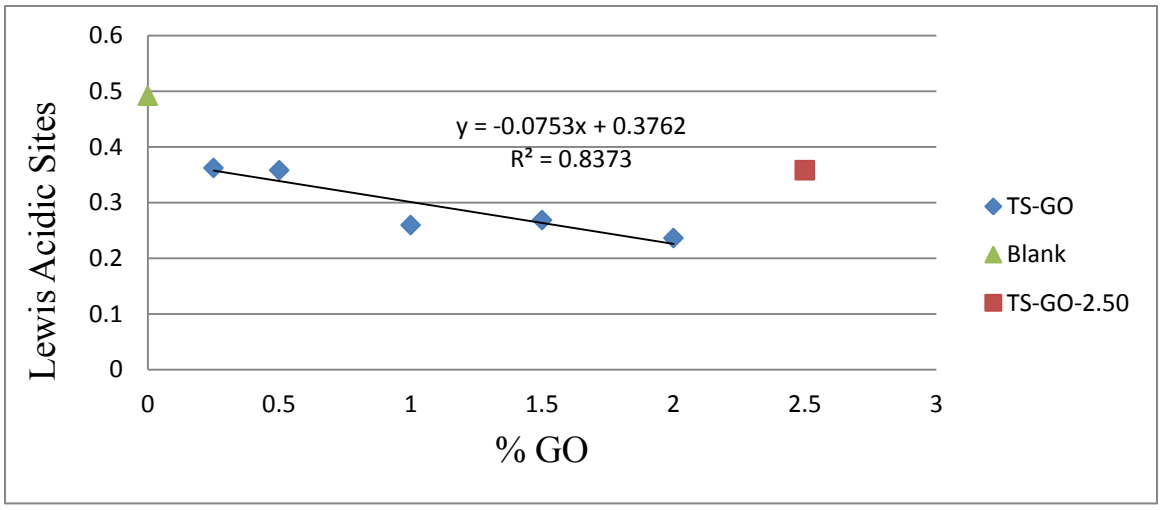

Figure (5-4) Variation of surface Lewis acidic sites of TS-GO samples measured by perichromic TBSB/DTBSB pair with percentage content of GO.

NH_3-TPD results for overall surface acidity are shown in Figure (5-5). All TS-GO samples were found more acidic than the blank sample and the acidity generally decreases with the increase in GO content linearly from 0.5-2%. This can be attributed to the highly oxygenated surface of GO which contains alcoholic, phenolic, epoxy, carboxyl and other oxygenated groups, and which therefore contributes to the values of sample surface acidity measured by ammonia adsorption/desorption. These groups primarily increase Brønsted acidity in agreement with previous work by Morales-Torres et al. [48], [142]. On the other hand, the decrease in the number of acidic sites with the increase in the GO content can be attributed to the formation of Ti-O-C bonds in the nanocomposite samples, thus reducing the availability of these groups for interaction with the ammonia probe [21].

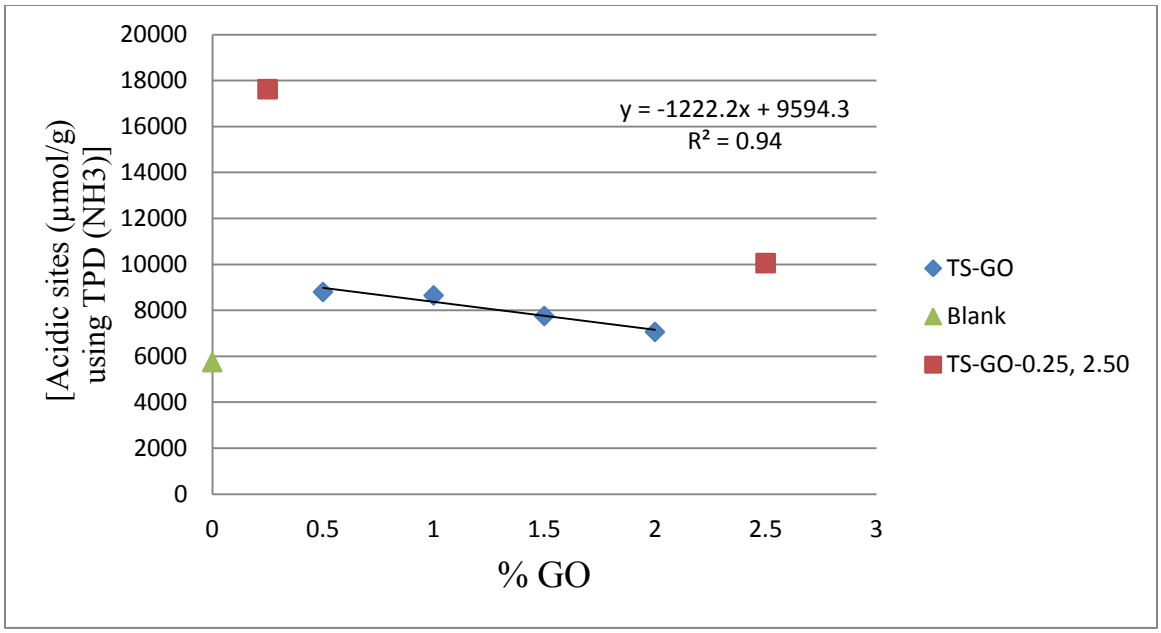

Figure (5-5) Variation of overall surface acidity of TS-GO samples measured by NH_3-TPD with percentage content of GO.

Figure (5-6) shows the presence of linear relationship between the Lewis acidity measured by the perichromic TBSB/DTBSB pair and the surface acidity measured by NH_3-TPD. Linearity indicates that perichromic dyes can be used to elucidate surface acidity (Lewis acidic sites).

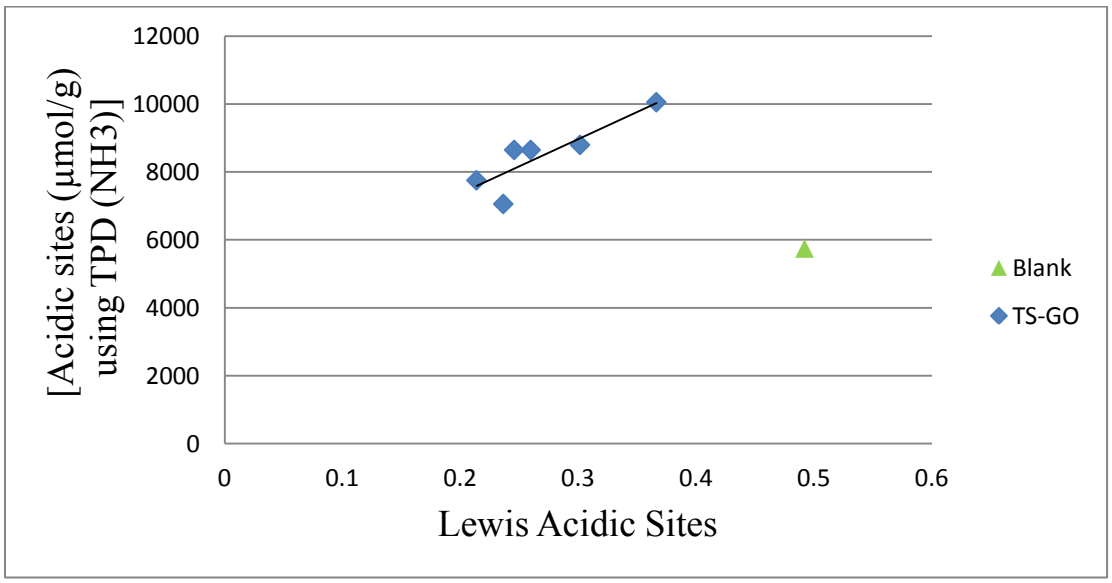

Figure (5-6) Linear relationship between the overall surface acidity measured by NH_3-TPD and the Lewis acidity measured by the perichromic TBSB/DTBSB pair for TS-GO samples.

5.2.2. Surface Polarity and Polarizability:

Surface polarity of TS-GO samples which is measured by WB perichromic dye shows that all samples are generally more polar than the blank and the polarity increases with increase in GO content as shown in Figure (5-7). The higher polarities than the blank is attributed to the oxygenated functional groups on the surface of GO which will increase the polarity of the nanocomposites. Increasing the GO will consequently increase the polarity of the formed nanocomposites. The increase in GO content is associated with the formation of more Ti-O-C bonds; this reduces the number of Ti^{+n} cations and acidic protons in the surface hydroxyl groups of TS-GO samples while the number of oxygen containing functional groups remains unaffected. Consequently, the formation of Ti-O-C bonds will not affect the surface polarity which increases with the increase in GO content.

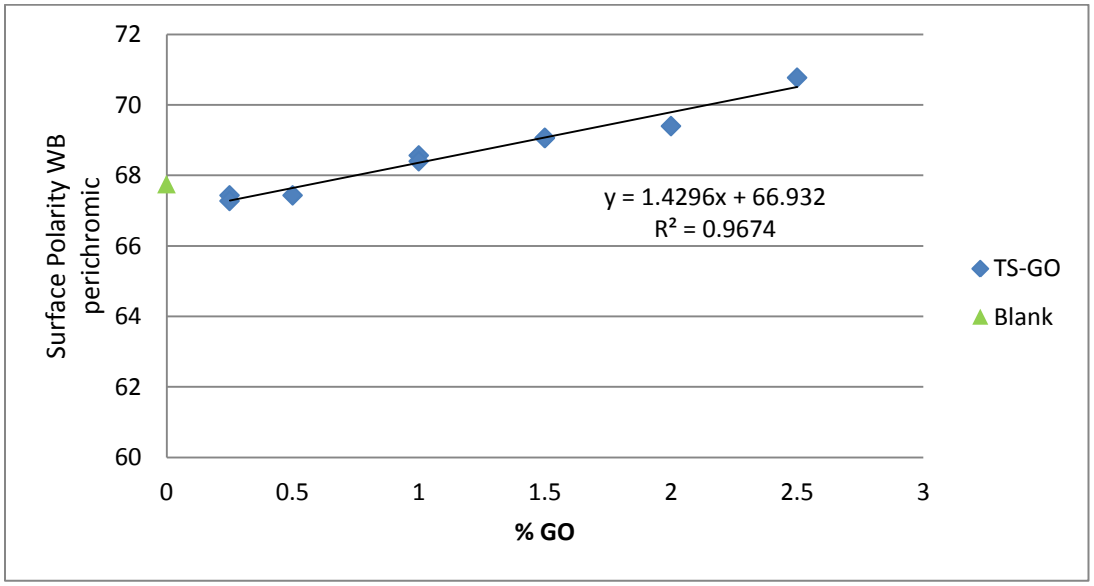

Figure (5-7) Variation of surface polarity of TS-GO samples as measured by WB perichromic dye with percentage content of GO.

On the other hand, the surface polarizability measured using β-Carotene perichromic dyes decreases with the increase in GO content. Surface polarizability measure mainly the van der Waals forces between the perichromic dye and the nanocomposites which arise mainly from the surface non-polarity [111], [119], [143]. Hence increasing the GO

content with highly oxygenated surface will decrease the surface polarizability of the formed TS-GO nanocomposites. However, values obtained, though showing the expected trend, are negative, hence not shown here. The reason for obtaining negative values is not clear, and will be examined later.

5.2.3. BET surface area and average pore diameter:

Figures (5-8, 5-9 and 5-10) confirm that all TS-GO samples have lower surface area than the blank sample and the change in the GO content does not result in a systematic trend for the surface area. The average pore diameter decreases slightly with the increase in the GO amount, and this is probably due to the formation of more Ti-O-C cross-links in the structure. However, the average pore diameter per surface area is almost constant and all points are more than the blank due to lower surface area of the samples. Table (5-1) contains the BET surface area, the average pore diameter and the average pore diameter per surface area as measured using the N_2 physisorption porosity analyzer for TS-GO samples. N_2 adsorption isotherms of TS-GO samples are presented in Appendix (I).

Table (5-1) BET surface area, average pore diameter and average pore diameter per surface area data of TS-GO samples.

% GO	Surface area (m^2/g)	BJH Adsorption average pore diameter (nm)	BJH Adsorption average pore diameter/surface area ($nm\ g/m^2$)
0	153	6.6	0.0429
0.25	132	6.7	0.0510
0.50	130	6.9	0.0536
1.00	141	6.6	0.0465
1.50	138	6.5	0.0471
2.00	138	6.7	0.0482
2.50	136	6.4	0.0475

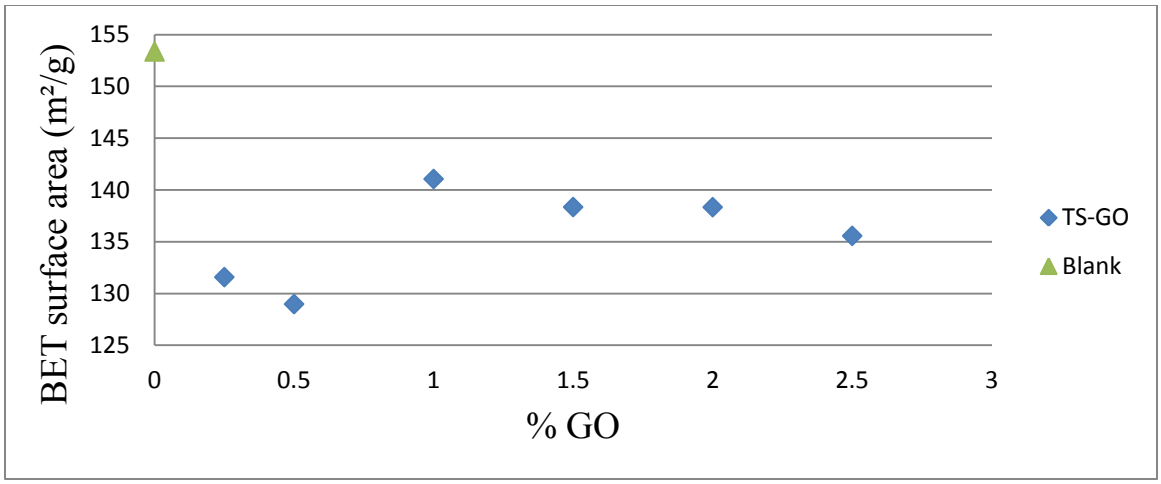

Figure (5-8) Variation of BET surface area of TS-GO samples with percentage content of GO.

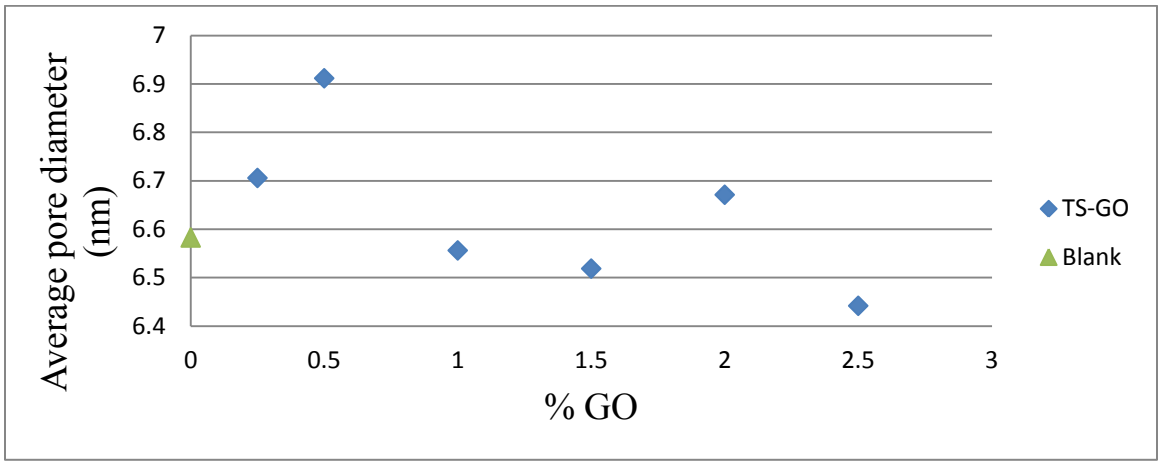

Figure (5-9) Variation of average pore diameter of TS-GO samples with percentage content of GO.

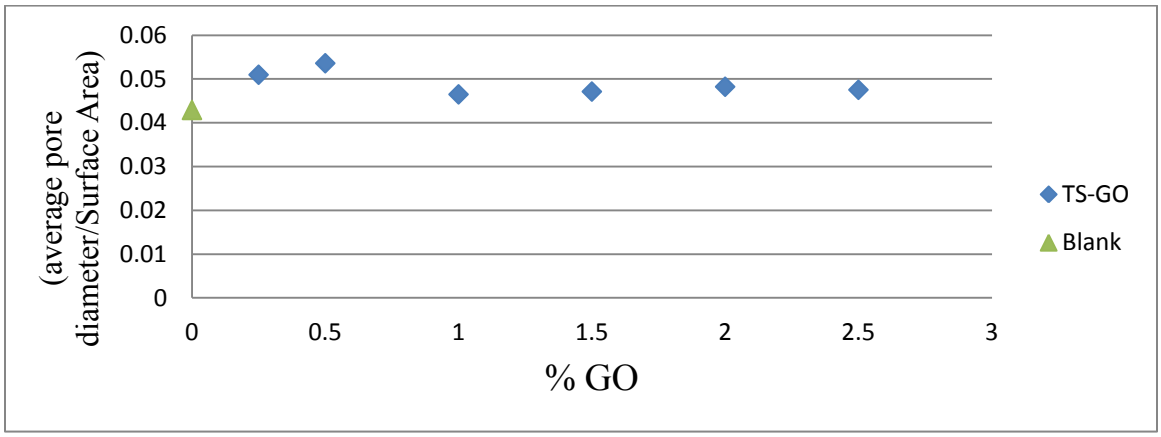

Figure (5-10) Variation of average pore diameter per surface area of TS-GO samples with percentage content of GO.

5.2.4. Band gap values for different TS-GO samples:

UV–Vis DRS spectra shown in Figure (5-11) demonstrate a bathochromic shift in all TS-GO samples and this red shift slightly increases with the increase in GO content. The band gap energy (E_g) can be calculated using transformed Kubelka–Munk function: $E_g = 1240/\lambda_g$ where, λ_g is the band gap wavelength and obtained from a plot of the sample maximum absorbance versus the wavelength in nm. The *x*-axis intercept of the tangent to the plot represents λ_g. Table (5-2) presents the E_g values for the different samples. The variation of the GO amount in the formed nanocomposites does not lead to a noticeable change in the band gap energy which may be attributed to the complex nature of the nanocomposites' surfaces. These results demonstrate that the change in band gap energy has a minimal effect on the photocatalytic degradation rate of MB (please refer to section 5.2.5).

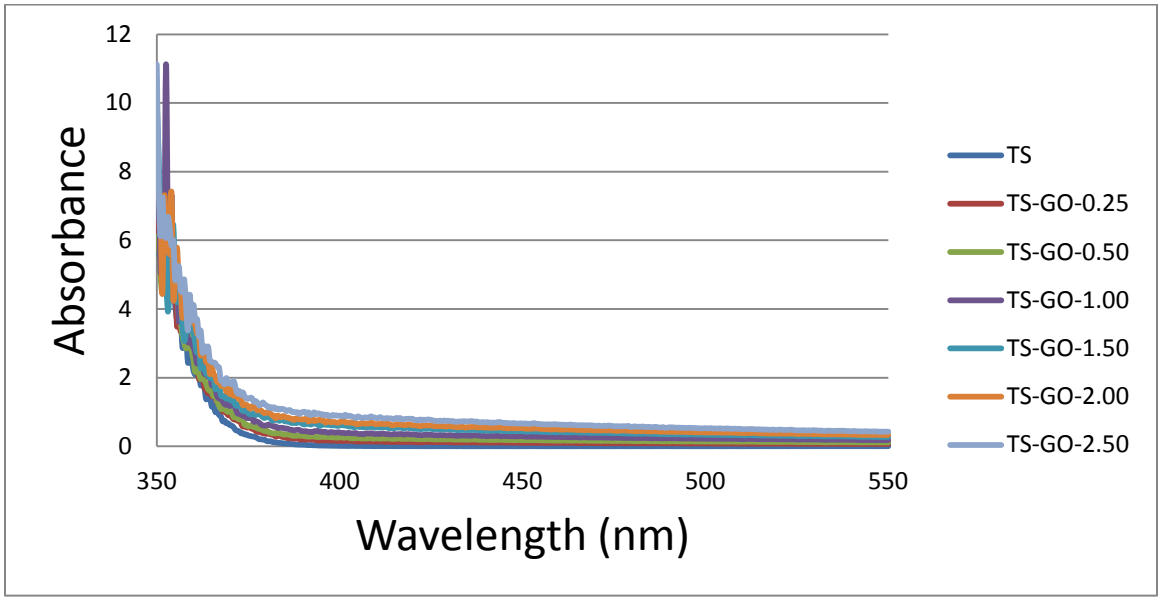

Figure (5-11) UV–Vis DRS spectra of TS-GO samples.

Table (5-2) Band gap values for different TS-GO samples.

Sample	**TS**	**TS-GO 0.25**	**TS-GO 0.50**	**TS-GO 1.00**	**TS-GO 1.50**	**TS-GO 2.00**	**TS-GO 2.50**
Band gap energy (eV)	3.354	3.349	3.343	3.342	3.337	3.323	3.321

5.2.5. Photocatalytic activity:

All TS-GO samples demonstrated higher photocatalytic activity for the decomposition of MB than the blank as presented in Table (5-3). The photocatalytic activity decreases linearly with increase in GO content as presented in Figure (5-12). The kinetics of the photocatalytic degradation reaction exhibits zero order behavior, meaning the reaction rate is controlled by factor(s) other than MB concentration, most certainly the surface properties of the solids. The presence of GO can possibly have a number of different effects. GO can act as an electron sink for the photogenerated electrons causing a decrease in the electron-pair recombination rate and GO itself can play a role as a photocatalyst in the decomposition of MB [12], [144]. On the other hand, increasing the GO content may possibly block the photocatalytic active sites on the surface of TiO_2 limiting their accessibility to the reacting species, and leading to a decrease in photocatalytic activity [21]. The results demonstrate that the latter effect is more prominent, with the decrease in photocatalytic activity of the nanocomposites with increasing GO content. These results are consistent with overall surface acidity values determined by NH_3-TPD. This demonstrates that overall surface acidity plays the primary role in the photodegradation of MB by these nanocomposite samples. The linear relationship between surface acidity and photocatalytic activity of TiO_2 or TiO_2 nanocomposites has been reported in prior investigations [142]. However, the photocatalytic activity of TS-GO nanocomposites seems to be dependent on the combined effect of a number of factors such as surface acidity, surface area, as well as band gap values.

Table (5-3) Zero order rate constants for the photocatalytic degradation of MB using TS-GO samples.

Sample	Rate constant *10^{-8} (mole L^{-1} min^{-1})
TS	2.04
TS-GO-0.25	3.00
TS-GO-0.50	3.14
TS-GO-1.00	2.73
TS-GO-1.50	2.73
TS-GO-2.00	2.26
TS-GO-2.50	2.23

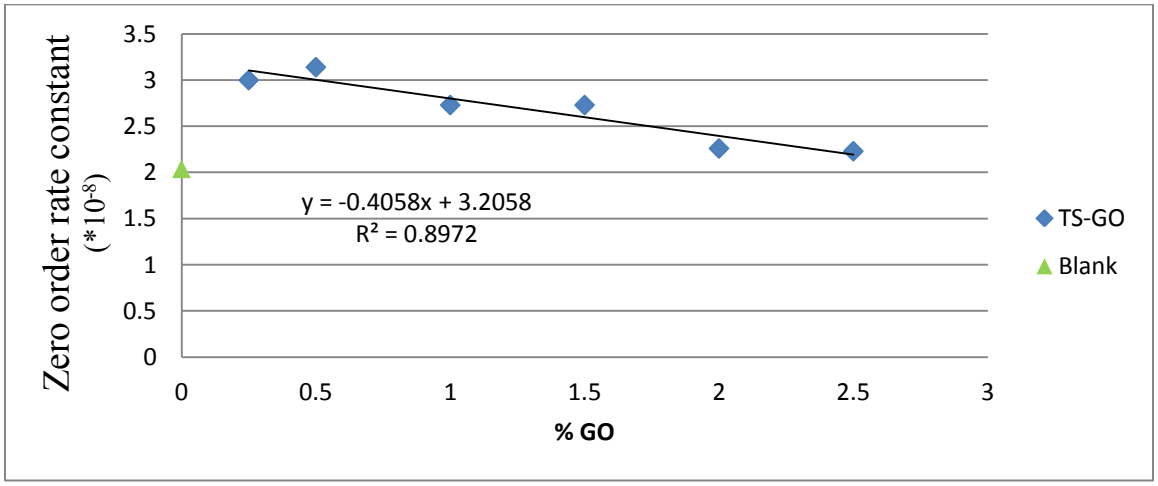

Figure (5-12) A plot of the zero order rate constants versus percentage content of GO for the photodegradation of MB using TS-GO samples.

5.2.6. Structural and compositional characteristics:

A- XRD:

XRD results reveal that the anatase crystalline phase of TiO_2 is the predominant phase and the crystalline structure of TiO_2 is not affected by the addition of GO as demonstrated in Figure (5-13). XRD peaks located at 2-theta values of 25.3°, 38°, 48°, 55° and 64° can be attributed respectively to (101), (004), (200), (105) and (204) crystal

planes of anatase TiO_2 [23]. The main characteristic peak of G at 24.5° is usually not observed due to masking effect of the strong anatase peak at 25.3° [32]. The small peak at 11°, attributed to the diffraction of GO, is not observed due to its low diffraction intensity and the disruption of GO exfoliation sheets in the formed nanocomposites samples. This has indeed been reported before [43], [49]. In addition, the presence of XRD peak at 31° indicates the presence of small amounts of Brookite [145], [146]. This indicates that the TS containing samples have mixed anatase/ brookite crystalline phases and this mixed phase photocatalysts generally have a higher photocatalytic activity than that of either phase alone because of the improved quantum efficiency of the mixed phase [36]. Furthermore, the absence of XRD peak at 27° of rutile TiO_2 crystal phase confirms that the main TiO_2 crystalline phase present in the TS-GO nanocomposites is the anatase phase with high photocatalytic activity [43].

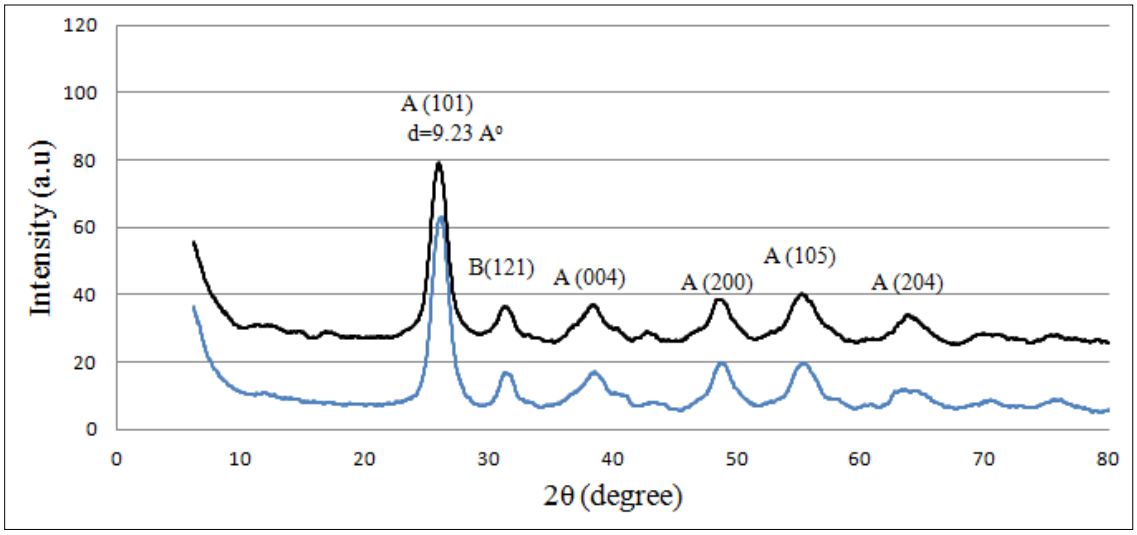

Figure (5-13) XRD spectra of TS (blue) and TS-GO-1.50 (black) as representative nanocomposite sample where, A and B are the Anatase and Brookite crystalline phases of TiO_2 respectively.

B- FTIR:

FTIR spectra for TS-GO nanocomposites show a strong band at ca. 600 cm^{-1} attributed to Ti-O-Ti and Ti-O-C bonds. The strong and broad band at ca. 3450 cm^{-1} is associated with the stretching vibration of surface hydroxyl groups on the TiO_2 surface. The presence of surface hydroxyl groups is further confirmed by the bending hydroxyl vibration at around

1640 cm $^{-1}$. The peak at 1640 cm^{-1} is assigned also to the bending vibration of molecular water, which would be present in the sample due to the water vapor from the atmosphere, and the aromatic ring vibration within the GO structure is located within the same region. Figure (5-14) shows the main absorption bands in the FTIR of TS-GO samples. The absence of the signal at 1720 cm^{-1} can show that the oxygenated surface of GO contains mainly hydroxyl group rather than ketonic or carboxyl groups [11], [43], [44].

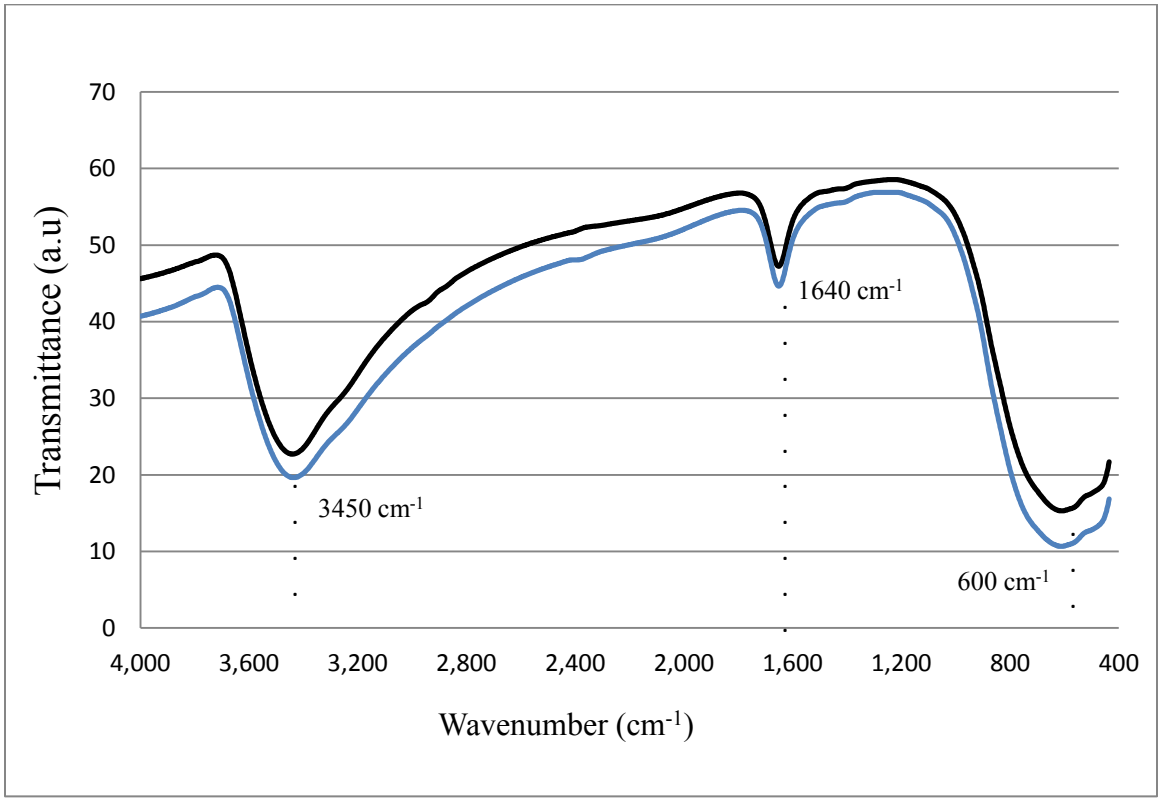

Figure (5-14) FTIR spectra of TS (black) and TS-GO-1.50 (blue) as representative nanocomposite sample.

*C- **Raman spectroscopy:***

Raman results presented in Figures (5-15) and (5-16) confirm the predominance of anatase crystal phase of TiO_2 and the formation of TS-GO nanocomposites. The Raman shift is plotted against normalized values because the intensity of the blank is much higher than the TS-GO samples. The anatase phase of TiO_2 is confirmed by the presence of vibration modes at ca. 142 cm^{-1} (E_g), 398 cm^{-1} (B_{1g}), 512 cm^{-1} (B_{1g} +A_{1g}) and 626 cm^{-1}

(E_g) in all samples. The loss of fine structure in the TS-GO nanocomposites samples and the small shift in the 142 cm^{-1} (E_g) band may be attributed to the formation of Ti-O-C on the surface of the nanocomposites. The presence of GO in the nanocomposites is confirmed by the presence of G band (the E_{2g} mode of sp^2 carbon atoms) at 1590 cm^{-1} and the D band (the symmetric A_{1g} mode) at 1360 cm^{-1}. The G band at 1590 cm^{-1} confirms the presence of in-plane vibrations of sp^2 carbon structure and the D band at 1360 cm^{-1} is attributed to sp^3 defects in the GO structure. The comparable ratio between the G and D bands indicates the presence of GO with oxygenated sp^3 carbon structure [147]. The previous results confirmed the incorporation of TiO_2 and GO in the formed nanocomposites [12], [23], [25], [27], [38], [44], [49].

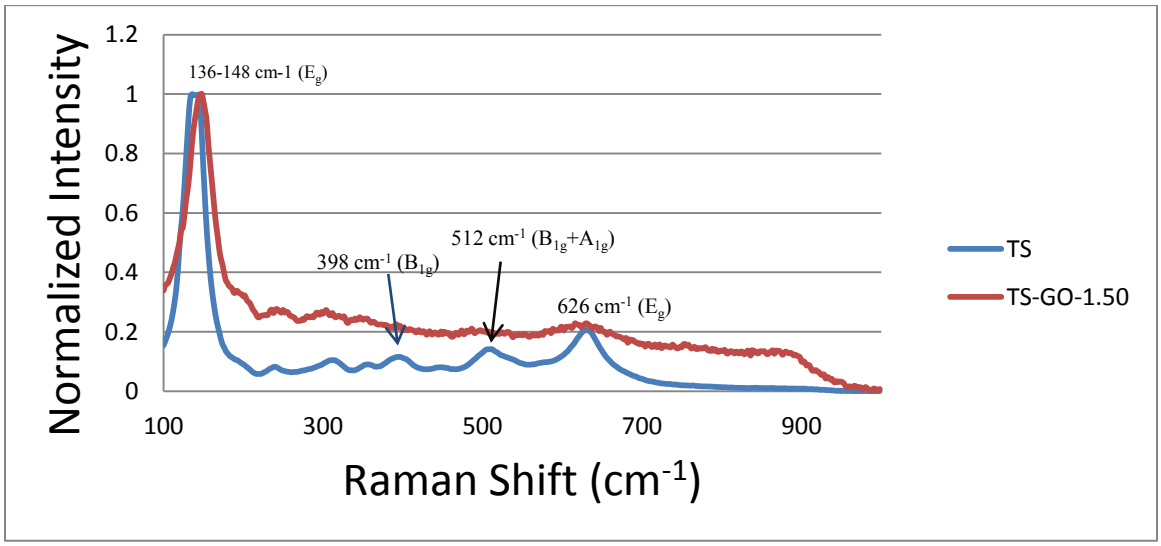

Figure (5-15) Raman spectra of TiO_2 in TS (blue) and TS-GO-1.50 (red) as representative nanocomposite sample.

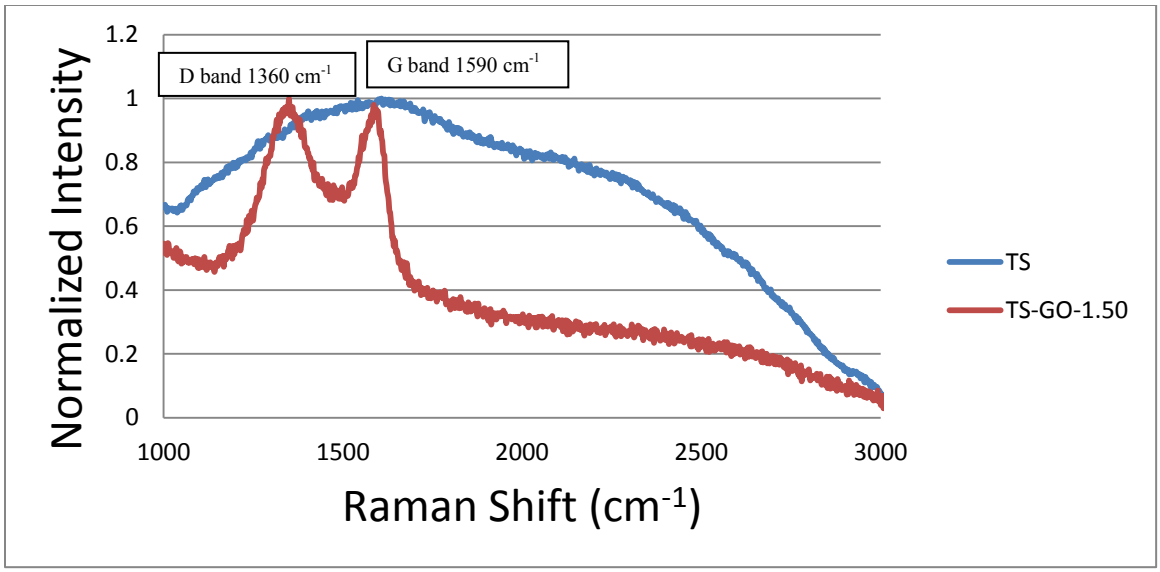

Figure (5-16) Raman spectra of carbon species in TS (blue) and TS-GO-1.50 (red) as representative nanocomposite sample.

5.3. *T small-G (TS-G) nanocomposites:*

5.3.1. *Surface acidity:*

Figure (5-17) shows that surface acidity of the TS-G nanocomposite samples are lower than the blank TiO_2 sample. This can be attributed to the formation of Ti-O-C covalent bonds which would lead to a decrease in the number of Ti^{+n} cations available on the surface of the nanocomposites. This results in the overall decrease in the number of Lewis acidic sites. However, the increase in G content has no significant effect on the Lewis surface acidity measured by perichromic dyes.

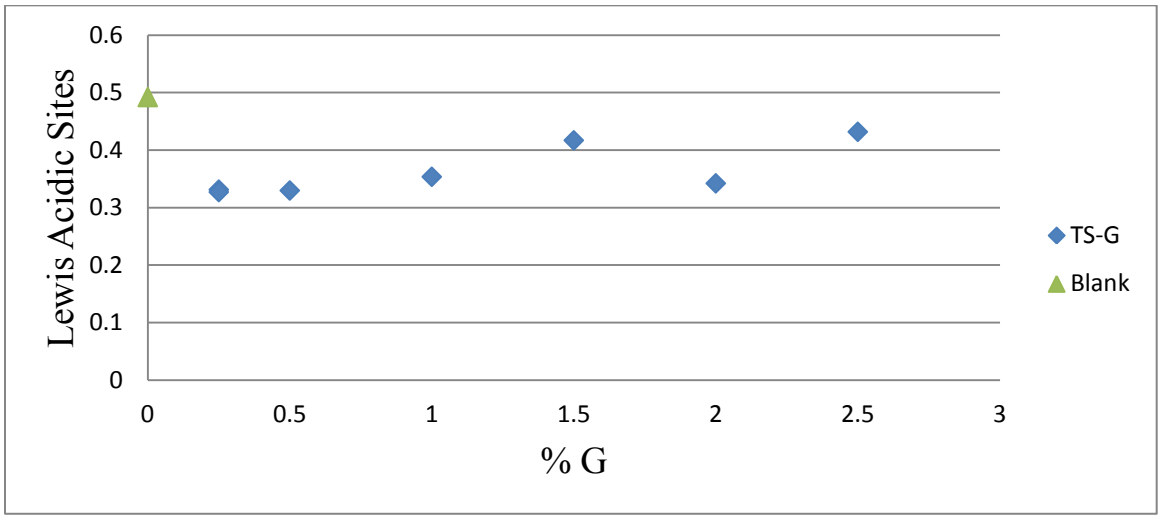

Figure (5-17) Variation of surface Lewis acidic sites of TS-G samples measured by perichromic TBSB/DTBSB pair with percentage content of G.

For NH_3-TPD, Figure (5-18) shows that all TS-G samples are more acidic than the blank and the acidity slightly decreases with the increase in G content linearly. The increase in surface acidity can be attributed to strong chemical interaction between TiO_2 and G leading to the availability of more acidic hydrogen of TiO_2 (as Brønsted acidic sites) on the surface of the formed nanocomposites. The increase in Brønsted acidic sites would increase the overall acidity of the formed nanocomposites despite the decrease in the number of Lewis acidic sites, with respect to the blank, as measured by perichromic dyes. These results demonstrate that, for our samples, Brønsted acidity exhibits higher contribution to overall surface acidity compared to Lewis acidity as reported by Katada et

al [148]. On the other hand, the increase in G content causes stacking of G nanosheets on the surface of TiO_2 nanoparticles as reported by Štengl et al [149] with subsequent slight decrease in the overall surface acidity.

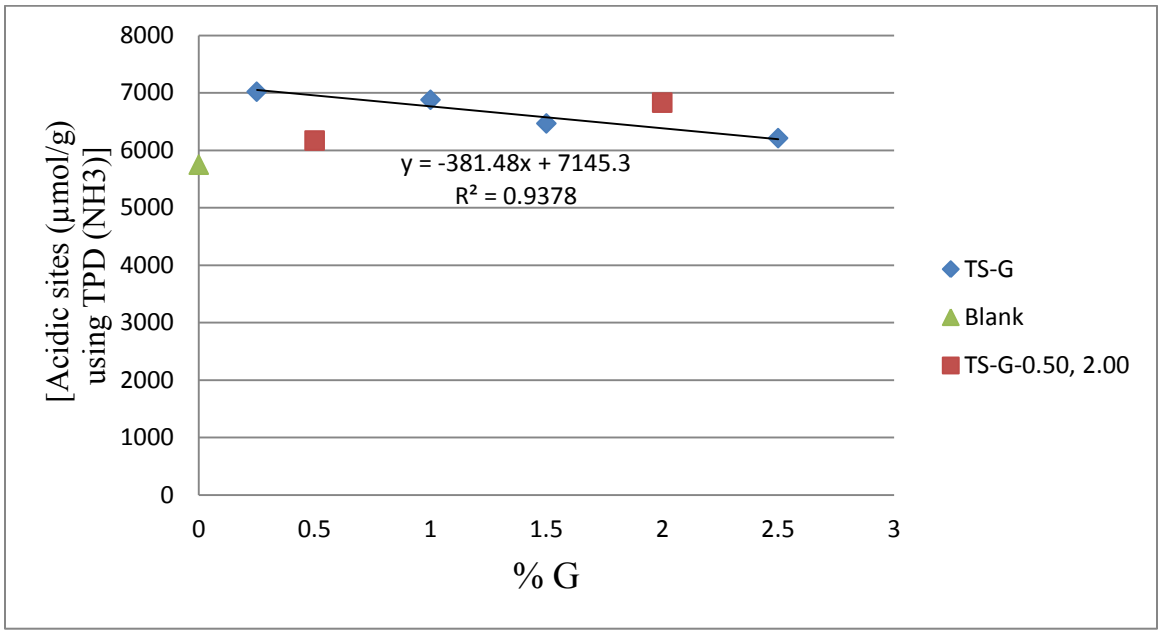

Figure (5-18) Variation of overall surface acidity of TS-G samples measured by NH_3-TPD with percentage content of G.

Figure (5-19) shows the presence of linear relationship between the Lewis acidity measured by the perichromic TBSB/DTBSB pair and the surface acidity measured by NH_3-TPD. Linearity indicates that perichromic dyes can be used to elucidate surface acidity (Lewis acidic sites).

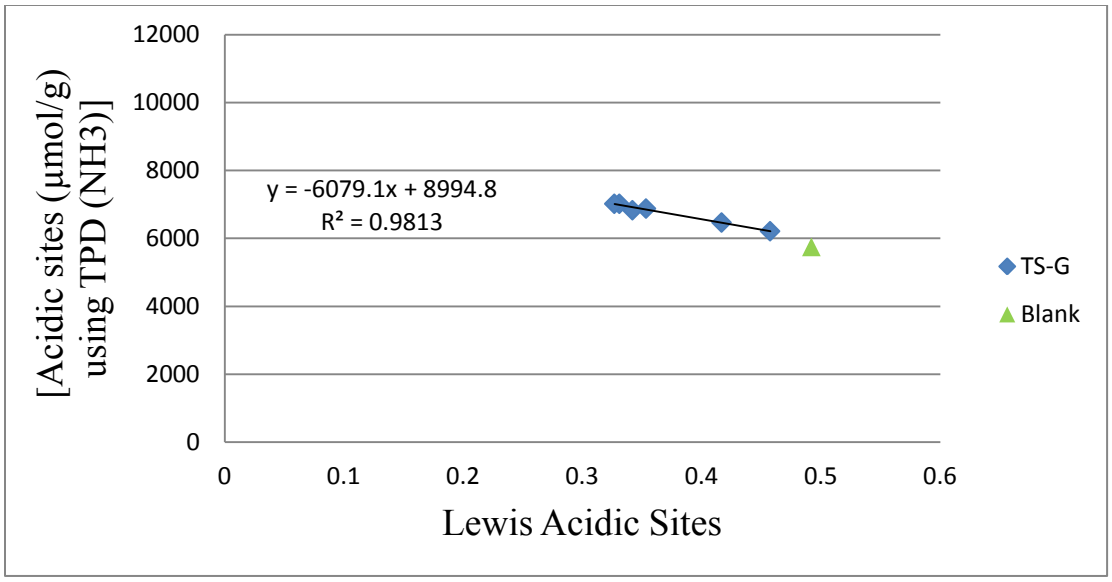

Figure (5-19) Linear relationship between the overall surface acidity measured by NH_3-TPD and the Lewis acidity measured by the perichromic TBSB/DTBSB pair for TS-G samples.

5.3.2. Surface Polarity and Polarizability:

The trend in surface polarity for the TS-G samples is a complex one, as presented in Figure (5-20), with decreasing from G content of 0.25% till 1.00%, after which the polarity increases. The full elucidation of this trend would need further detailed investigations such as photoluminescence spectroscopy (PL) x-ray photoelectron spectroscopy (XPS). The hydrophobic nature of G decreases the surface polarity of TS-G samples with the increase in G content as reported by Basheer et al [150]. However, the stacking of G nanosheets could be leading to restoring some surface polar groups so the surface polarity increases beyond the TS-G-1.00 sample.

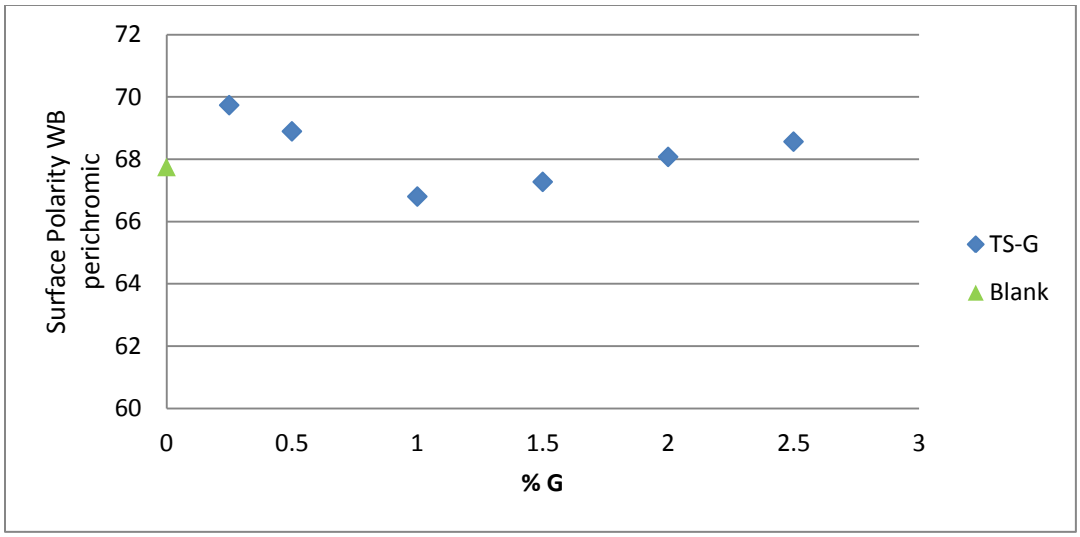

Figure (5-20) Variation of surface polarity of TS-G samples as measured by WB perichromic dye with percentage content of G.

On the other hand, the surface polarizability measured using β-Carotene perichromic dyes of all samples is higher than the blank and the surface polarizability increases linearly with the increase in G content as presented in Figure (5-21). Surface polarizability measures mainly the van der Waals forces between the perichromic dye and the nanocomposites which arise mainly from the surface non-polarity [111], [119], [143]. This means that the higher the G with its aromatic π-π skeleton, the higher the surface polarizability of the formed nanocomposites.

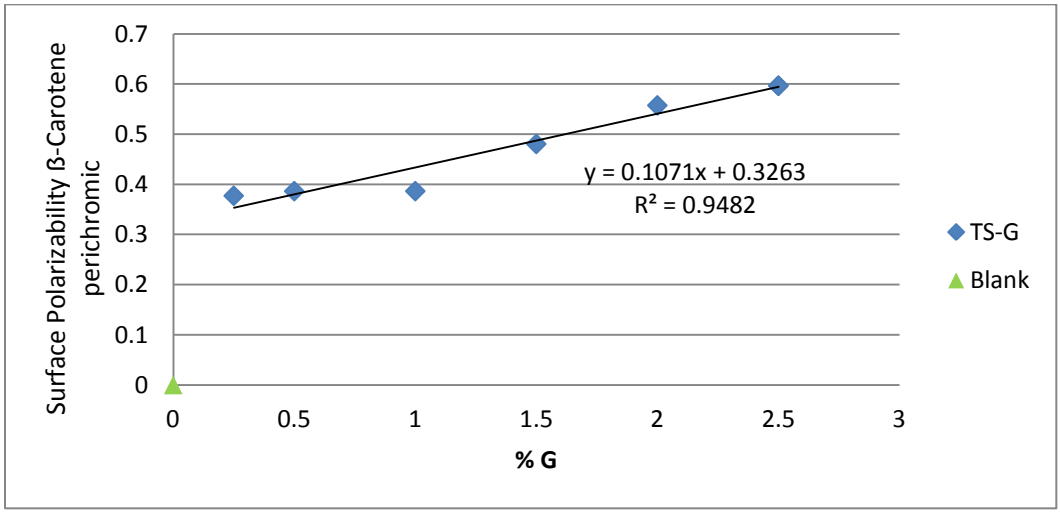

Figure (5-21) Variation of surface polarizability of TS-G samples as measured by β-Carotene perichromic dye with percentage content of G.

5.3.3. BET surface area and average pore diameter:

Figures (5-22, 5-23 and 5-24) confirm that all TS-G samples are about the same in surface area as the blank and the changing in the G content has almost no effect on the surface area. This can be attributed to the formation of more Ti-O-C bonds with the increase in G content. The average pore diameter is almost constant and slightly lower than the blank. However, average pore diameter per surface area is almost constant. Table (5-4) contains the BET surface area, the average pore diameter and the average pore diameter per surface area for the TS-G samples. N_2 adsorption isotherms of TS-G samples are presented in Appendix (I). These results indicate that the addition of G to TiO_2 has little effect on sample surface area and porosity.

Table (5-4) BET surface area, average pore diameter and average pore diameter per surface area data of TS-G samples.

% G	Surface area (m^2/g)	BJH Adsorption average pore diameter (nm)	BJH Adsorption average pore diameter/surface area ($nm\ g/m^2$)
0	153	6.6	0.0429
0.25	163	5.7	0.0350
0.50	142	5.8	0.0409
1.00	172	5.6	0.0325
1.50	169	5.7	0.0336
2.00	170	5.8	0.0340
2.50	167	5.6	0.0336

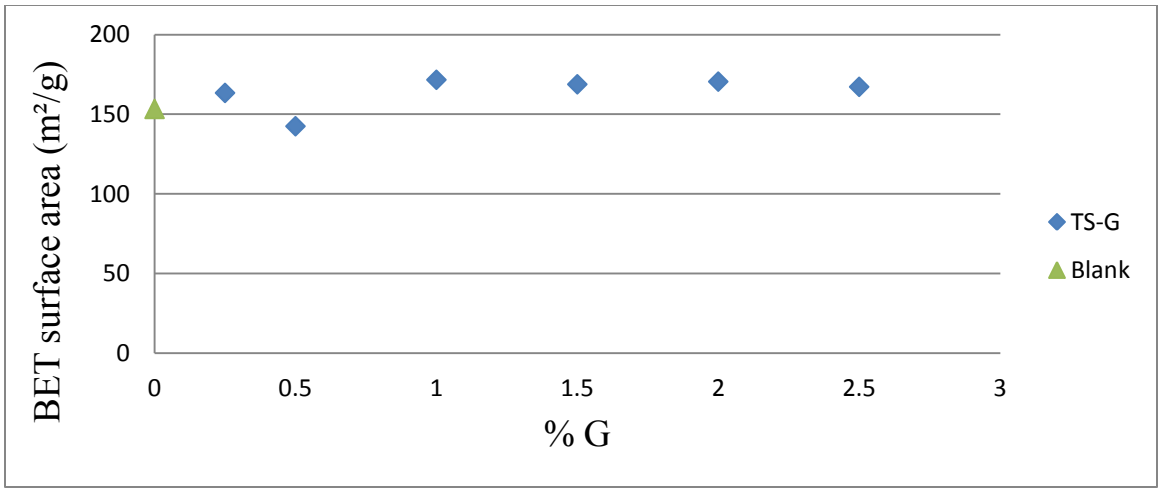

Figure (5-22) Variation of BET surface area of TS-G samples with percentage content of G.

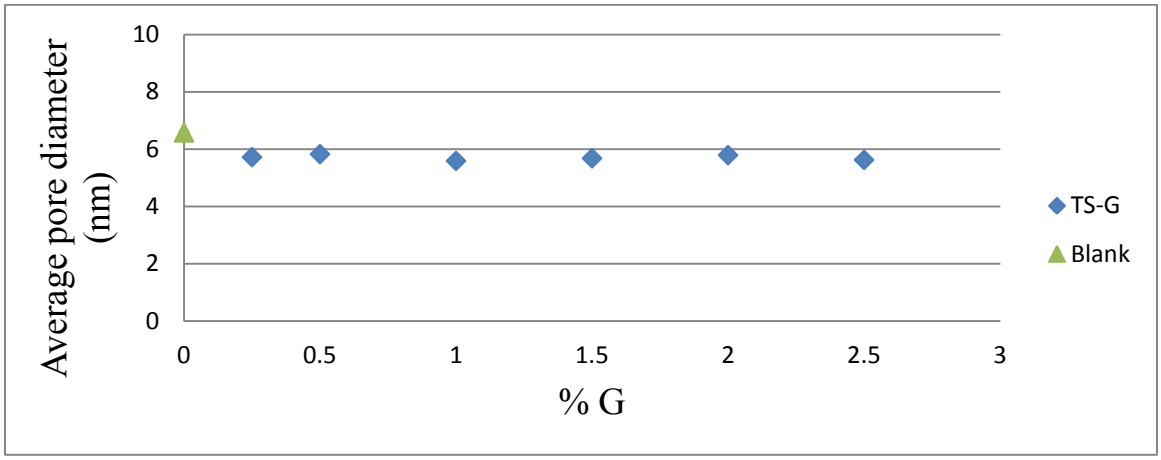

Figure (5-23) Variation of average pore diameter of TS-G samples with percentage content of G.

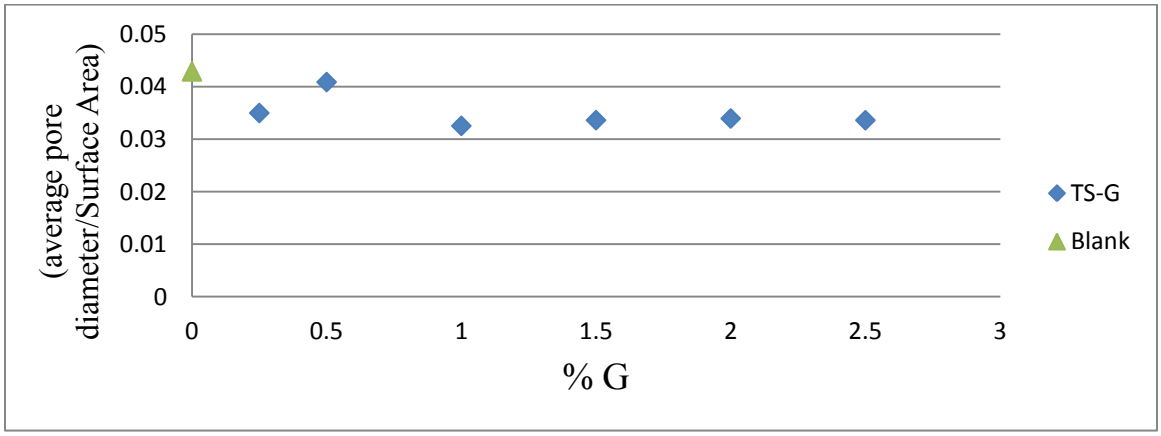

Figure (5-24) Variation of average pore diameter per surface area of TS-G samples with percentage content of G.

5.3.4. Band gap values for different TS-G samples:

UV–Vis DRS spectra shown in Figure (5-25) demonstrates a bathochromic shift in all TS-G samples and this red shift slightly increases with the increase in G. The band gap energy (E_g) can be calculated using transformed Kubelka–Munk function: $E_g = 1240/\lambda_g$ where, λ_g is the band gap wavelength and obtained from a plot of the sample maximum absorbance versus the wavelength in nm. The *x*-axis intercept of the tangent to the plot represents λ_g. Table (5-5) presents the E_g values for the different samples. However, the variation of the G amount in the formed nanocomposites does not lead to a noticeable change in the band gap energy as discussed before.

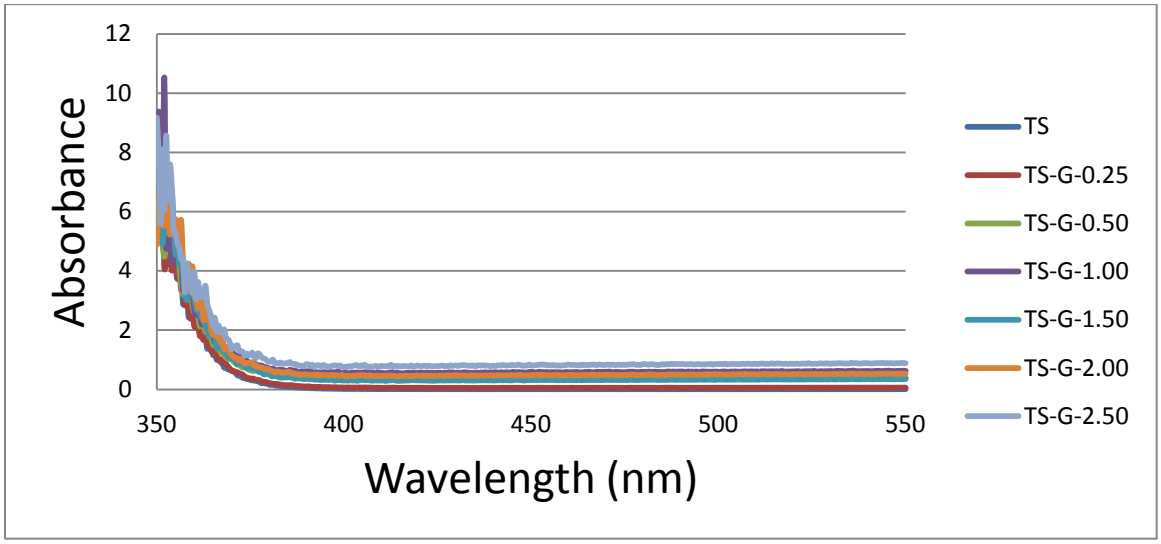

Figure (5-25) UV–Vis DRS spectra of TS-G samples.

Table (5-5) Band gap values for different TS-G samples.

Sample	**TS**	**TS-G-0.25**	**TS-G-0.50**	**TS-G-1.00**	**TS-G-1.50**	**TS-G-2.00**	**TS-G-2.50**
Band gap energy (eV)	3.354	3.354	3.338	3.330	3.342	3.330	3.329

5.3.5. Photocatalytic activity:

All TS-G samples demonstrated higher photocatalytic activity for the decomposition of MB than the blank as presented in Table (5-6). The photocatalytic activity decreases linearly with increase in G content except 2% as presented in Figure (5-26). The kinetics of the photocatalytic degradation reaction exhibits zero order kinetics. The explanation is similar to that given in 5.2.5, i.e., addition of G to TiO_2 leads to the increase of the photocatalytic degradation of MB due to the enhanced adsorption of the dye molecules by the aromatic skeleton of G. In addition, G acts as electron sink for the photogenerated electrons causing a decrease in the electron-pair recombination rate and G itself can play an important role as a photocatalyst in the photodegradation of MB [12], [144]. However, increasing the G content may block the photocatalytic active sites on the surface of TiO_2 leading to overall decrease in the photodegradation activity [21]. The results demonstrate that the latter effect is more prominent, with the decrease in photocatalytic activity of the nanocomposites with increasing G content. These results are consistent with overall surface acidity values determined by NH_3-TPD.

Table (5-6) Zero order rate constants for the photocatalytic degradation of MB using TS-G samples.

Sample	**Rate constant $*10^{-8}$ (mole L^{-1} min^{-1})**
TS	2.04
TS-G-0.25	3.45
TS-G-0.50	3.42
TS-G-1.00	3.10
TS-G-1.50	2.98
TS-G-2.00	1.29
TS-G-2.50	2.41

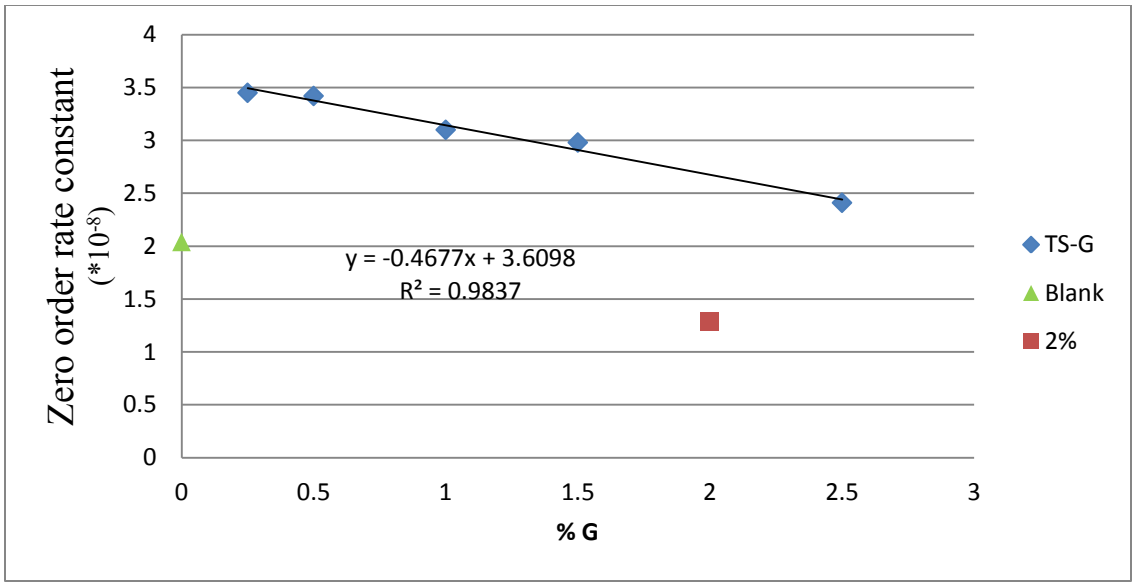

Figure (5-26) A plot of the zero order rate constants versus percentage content of G for the photodegradation of MB using TS-G samples.

5.3.6. Structural and compositional characteristics:

A- XRD:

XRD results reveal that the anatase crystalline phase of TiO_2 is the predominant phase and the crystalline structure of TiO_2 is not affected by the addition of G as demonstrated in Figure (5-27). XRD peaks located at 2-theta values of 25.3°, 38°, 48°, 55° and 64° can be attributed respectively to (101), (004), (200), (105) and (204) crystal planes of anatase TiO_2 [23]. The main characteristic peak of G at 24.5° is usually not observed due to masking effect of the strong anatase peak at 25.3° [32]. The small peak at 11°, attributed to the diffraction of G, is not observed due to its low diffraction intensity and the disruption of G exfoliation sheets in the formed nanocomposites samples. This has indeed been reported before [43], [49]. In addition, the presence of XRD peak at 31° indicates the presence of small amounts of Brookite [145], [146]. This indicates that the TS containing samples have mixed anatase/ brookite crystalline phases and this mixed phase photocatalysts generally have a higher photocatalytic activity than that of either phase alone because of the improved quantum efficiency of the mixed phase [36]. Furthermore, the absence of XRD peak at 27° of rutile TiO_2 crystal phase confirms that the main TiO_2

crystalline phase present in the TS-G nanocomposites is the anatase phase with high photocatalytic activity [43].

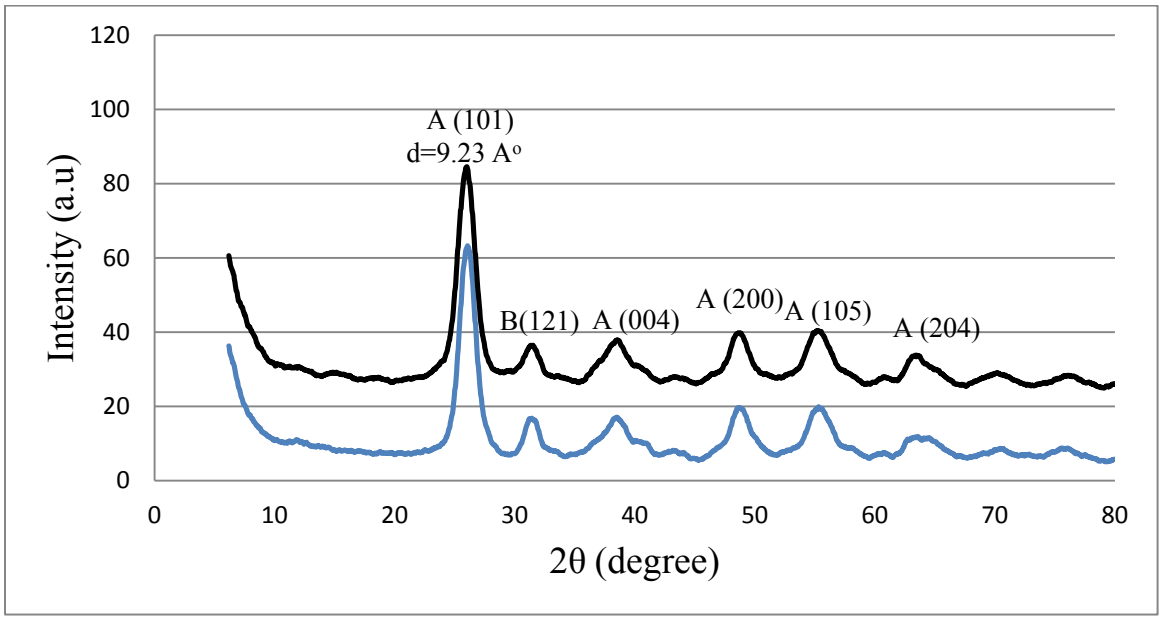

Figure (5-27) XRD spectra of TS (blue) and TS-G-1.50 (black) as representative nanocomposite sample where, A and B are the Anatase and Brookite crystalline phases of TiO_2 respectively.

B- FTIR:

FTIR spectra for TS-G nanocomposites show a strong band at ca. 600 cm^{-1} attributed to Ti-O-Ti and Ti-O-C bonds. The strong and broad band at ca. 3450 cm^{-1} is associated with the stretching vibration of surface hydroxyl groups on the TiO_2 surface. The presence of surface hydroxyl groups is further confirmed by the bending hydroxyl vibration at around 1640 cm^{-1}. The peak at 1640 cm^{-1} is assigned also to the bending vibration of molecular water, which would be present in the sample due to the water vapor from the atmosphere, and the aromatic ring vibration within the G structure is located within the same region. Figure (5-28) shows the main absorption bands in the FTIR of TS-G samples. The absence of the signal at 1720 cm^{-1} can show that the surface of G contains no carbonyl functional groups [11], [43], [44]

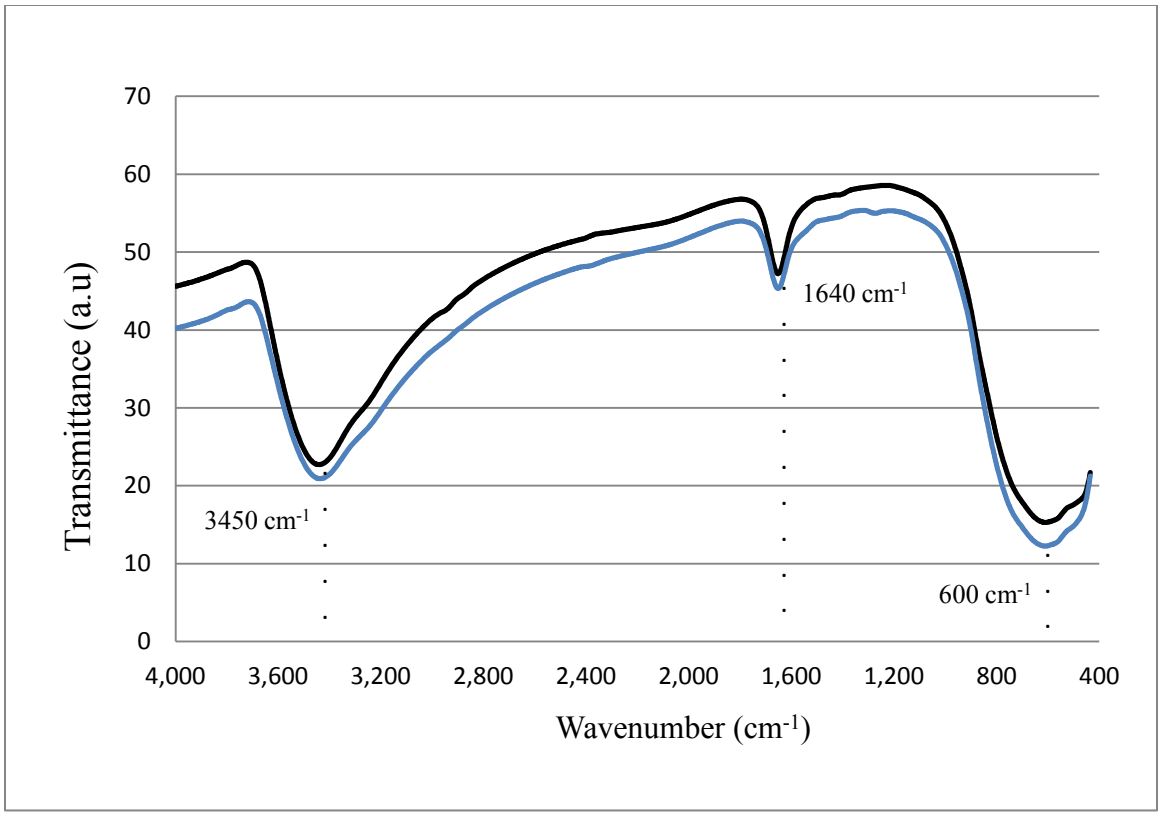

Figure (5-28) FTIR spectra of TS (black) and TS-G-1.50 (blue) as representative nanocomposite sample.

*C- **Raman spectroscopy:***

Raman results presented in Figures (5-29) and (5-30) confirm the predominance of anatase crystal phase of TiO_2 and the formation of TS-G nanocomposites. The Raman shift is plotted against normalized values because the intensity of the blank is much higher than the TS-G samples. The anatase phase of TiO_2 is confirmed by the presence of vibration modes at ca. 142 cm^{-1} (E_g), 398 cm^{-1} (B_{1g}), 512 cm^{-1} (B_{1g} +A_{1g}) and 626 cm^{-1} (E_g) in all samples. The loss of fine structure in the TS-G nanocomposites samples and the small shift in the 142 cm^{-1} (E_g) band may be attributed to the formation of Ti-O-C on the surface of the nanocomposites. The presence of G in the nanocomposites is confirmed by the presence of G band (the E_{2g} mode of sp^2 carbon atoms) at 1590 cm^{-1} and the D band (the symmetric A_{1g} mode) at 1360 cm^{-1}. The G band at 1590 cm^{-1} confirms the presence of in-plane vibrations of sp^2 carbon structure and the D band at 1360 cm^{-1} is attributed to sp^3 defects in the G structure. The high ratio between the D and G bands can

be attributed to the higher defect density present in the TS-G samples [22]. These defects can interfere with the efficient photogenerated electron transfer on the surface of G with subsequent decrease in the photocatalytic activity with the increase in G content as confirmed by our results. The previous results confirmed the incorporation of TiO_2 and G in the formed nanocomposites [12], [23], [25], [38], [44], [49].

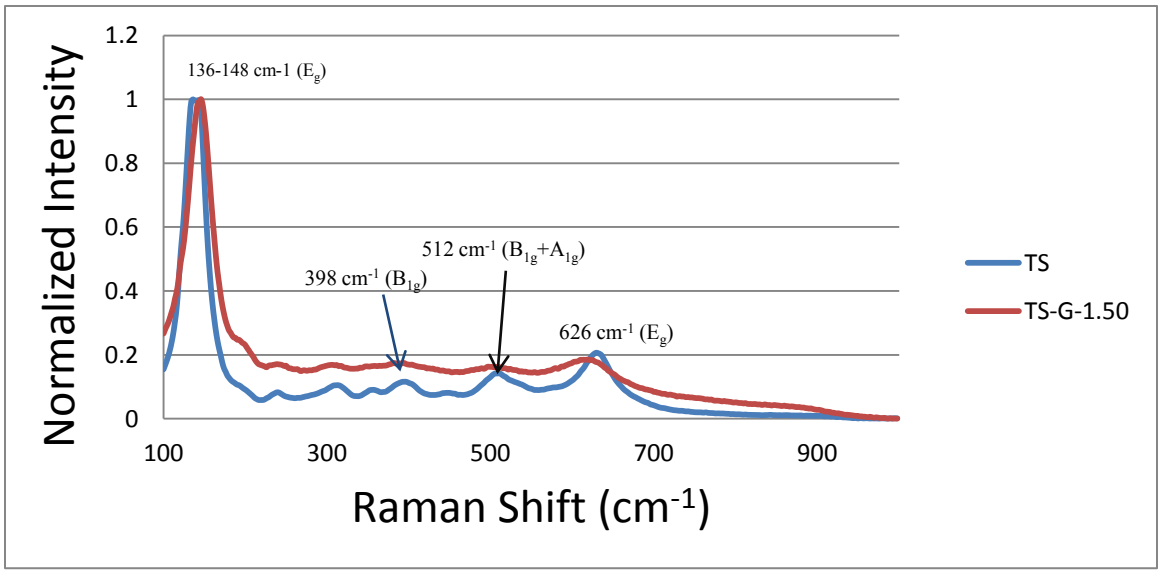

Figure (5-29) Raman spectra of TiO_2 in TS (blue) and TS-G-1.50 (red) as representative nanocomposite sample.

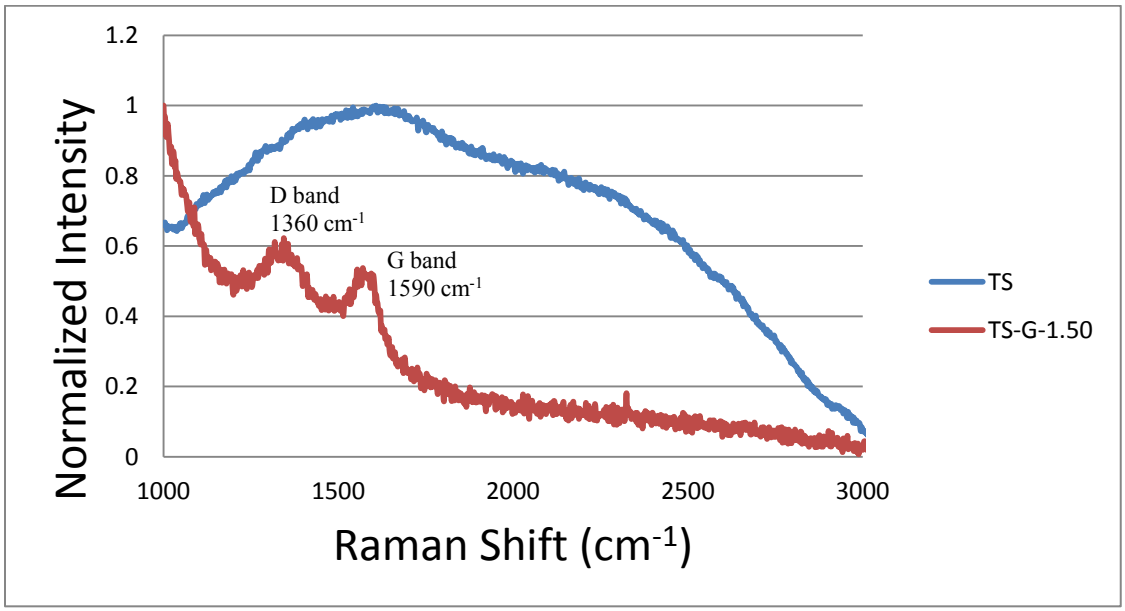

Figure (5-30) Raman spectra of carbon species in TS (blue) and TS-G-1.50 (red) as representative nanocomposite sample.

5.4. TS-GO versus TS-G Samples:

Lewis surface acidity measured using perichromic TBSB/DTBSB pair shows that both types of nanocomposites exhibit lower Lewis acidity than the blank sample and this can be attributed to the formation of Ti-O-C bonds which lead to this observed decrease [141]. On the other hand, TS-GO samples show lower Lewis acidity compared to TS-G samples as the oxygenated surface of GO will allow more Ti-O-C bonds to be formed. However, the trend of Lewis acidity variation with GO or G contents is different for each type of nanocomposites: As GO content increases, Lewis acidity is found to decrease, while the increase in G content has no significant effect on Lewis acidity. This difference is due to possible stacking of G nanosheets in the higher G content TS-G samples, which limits the formation of Ti-O-C bonds relative to the TS-GO samples, leading to limited change in the Lewis acidity [43].

As for overall acidity, determined by NH_3-TPD, both types exhibit higher overall surface acidity than the blank TS. In addition, TS-GO samples show higher overall surface acidity and a more significant variation with GO content, than is the case with TS-G samples. This is expected due to the highly oxygenated surface of GO [48], [142]. The overall surface acidity in both types of nanocomposites linearly decreases with the increase in GO/G content [21].

Linear correlation exists between both types of measurement of surface acidity (perichromic dyes and NH_3-TPD) in both samples with TS-G samples having a better linear correlation. This is an indication that perichromism can be used to elucidate the surface Lewis acidity of both TS-GO and TS-G nanocomposites.

Determination of surface polarity using WB dye shows that both TS-GO and TS-G samples have higher surface polarity than the blank. The surface polarity is directly proportional to the amount of GO or G in the sample. However, TS-GO samples have higher values of surface polarity and more significant variation with GO content than TS-G. This is expected due to the oxygenated surface of GO [142].

On the other hand, surface polarizability as measured using β-Carotene of TS-GO samples is generally lower than the blank and decreases linearly with the increase in the GO content, which is due to the increase in surface polarity associated with GO. On the contrary, addition of G increased surface polarizability and the increase is linear with the

amount of added G. This is due to the increase in overall surface hydrophobicity associated with the presence of G [111], [119].

The effect of G on the BET surface area is much more significant than GO since TS-GO samples have lower BET surface area values than the blank and TS-G samples while TS-G samples have higher BET surface area values than the blank. However, no clear effect of changing the GO or the G content on the surface area values is observed. This difference in values of surface areas of the two groups of samples is believed to be due to the increased interaction between the GO and the TiO_2 with the formation of Ti-O-C bonds [43]. This would increase the cross linking in the samples reducing the surface area. However for G, the interaction with TiO_2 might be less with consequent increase in the surface area.

The bathochromic shifts observed in the UV-Visible DRS spectra confirm the decrease in the band gap energy (E_g) after the addition of GO and G. however, this decrease is unnoticeable. TS-GO and TS-G samples have higher photocatalytic degradation rates of MB dye compared to the blank and the photocatalytic activity decreases with the increase in GO or G content. However, TS-GO samples have lower values of photocatalytic degradation rate compared to TS-G which imparts the importance of surface area effects on the photodegradation rate. The higher BET surface area values of TS-G samples have a more prominent effect on the photocatalytic degradation of MB dye compared to TS-GO samples with lower surface area. In addition, the presence of oxygenated functional groups on the surface of GO exhibits high defect density that can disrupt the electron transport properties of GO making it less efficient as electron sink for the photogenerated electrons of TiO_2 with overall decrease in the photocatalytic degradation rates as reported by Qian et al [35].

Structural and compositional data measured using XRD, FTIR and Raman spectroscopy confirm the formation of the nanocomposites between TiO_2 and GO or G. FTIR spectra show almost the same characteristic peaks with a minor increase in intensity in the TS-GO samples compared to TS-G samples denoting the presence of more surface oxygenated functional groups [44]. Furthermore, the difference between TS-GO and TS-G samples can be clearly observed using Raman spectroscopy. The loss of fine structure in the Raman spectrum after the addition of GO or G is attributed to the formation of Ti-

O-C bonds. The low frequency region (100-900 cm^{-1}) shows a blue shift to a higher frequency after the addition of GO or G confirming the formation of chemical bonds between TiO_2 and GO or G. The higher frequency region (1000-3000 cm^{-1}) confirms the presence of GO or G through the G and D bands [23], [25]. TS-G samples have lower intensity for the G and D bands than the TS-GO samples confirming the presence of GO in the TS-GO samples as reported by Štengl et al [149]. The higher ratio between D and G bands intensity in the TS-G samples indicates less stacking than the TS-GO samples and higher photocatalytic activity [22].

Anatase is the prominent crystalline phase of TiO_2 present in the samples and the crystalline structure is not greatly affected by the addition of GO or G as confirmed using XRD [23].

5.5. *T large-GO (TL-GO) nanocomposites:*

5.5.1. *Surface acidity:*

Figure (5-31) shows lower Lewis acidic sites in the TL-GO nanocomposites than blank TiO_2. This behavior can be attributed to the formation of Ti-O-C covalent bonds between TiO_2 and GO in the formed nanocomposites as proved by DRS-UV, FTIR and Raman spectroscopy results. The Ti-O-C bonds will decrease the number of Ti^{+n} cations on the surface of the nanocomposites leading to overall decrease in the number of Lewis acidic sites. The increase in the GO amount leads to the further decrease of the number of Ti^{+n} available for Lewis acidity, leading to the observed linear decrease.

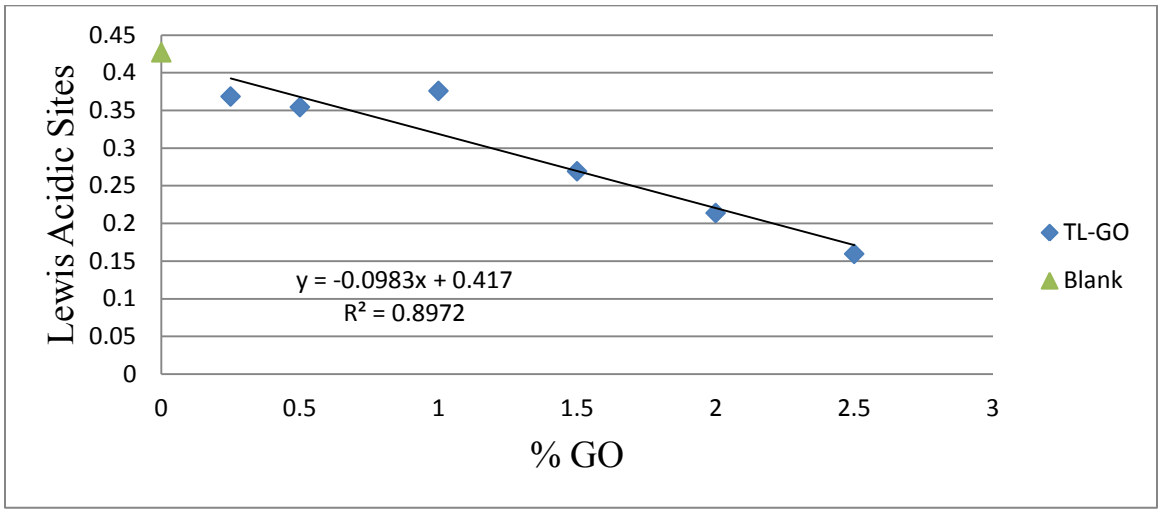

Figure (5-31) Variation of surface Lewis acidic sites of TL-GO samples measured by perichromic TBSB/DTBSB pair with percentage content of GO.

Figure (5-32) shows the correlation between the surface acidity measured by NH_3-TPD and the GO content where the acidity increases with the increase in GO content till 1% then decreases again with 2.5% GO. The surface of GO is highly oxygenated. The present groups will lead to increase in the overall acidity of the TL-GO nanocomposites than the blank TiO_2 due to larger number of acidic groups on the GO surface which are mainly Brønsted acidic sites. This is in agreement with previous work by Morales-Torres et al. [48], [142]. On the other hand, the decrease in the number of acidic sites with increase in the GO content may be due to formation of Ti-O-C bonds in the formed nanocomposites.

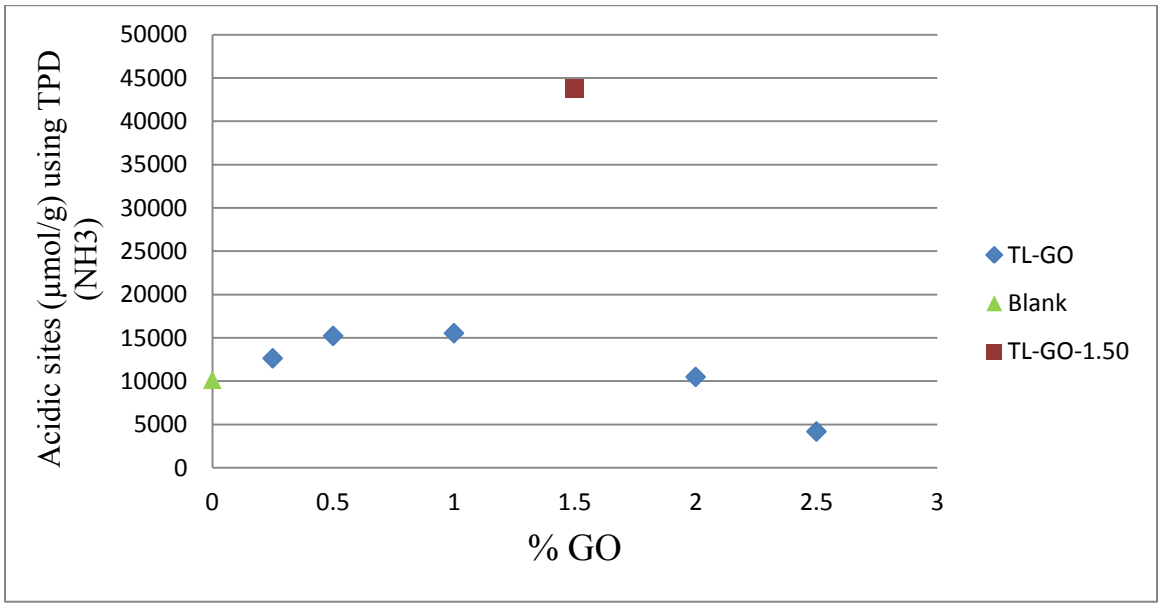

Figure (5-32) Variation of overall surface acidity of TL-GO samples measured by NH_3-TPD with percentage content of GO.

No clear correlation is observed between the Lewis acidity measured by the perichromic TBSB/DTBSB pair and the surface acidity measured by NH_3-TPD, see Figure (5-33), probably due to surface heterogeneity.

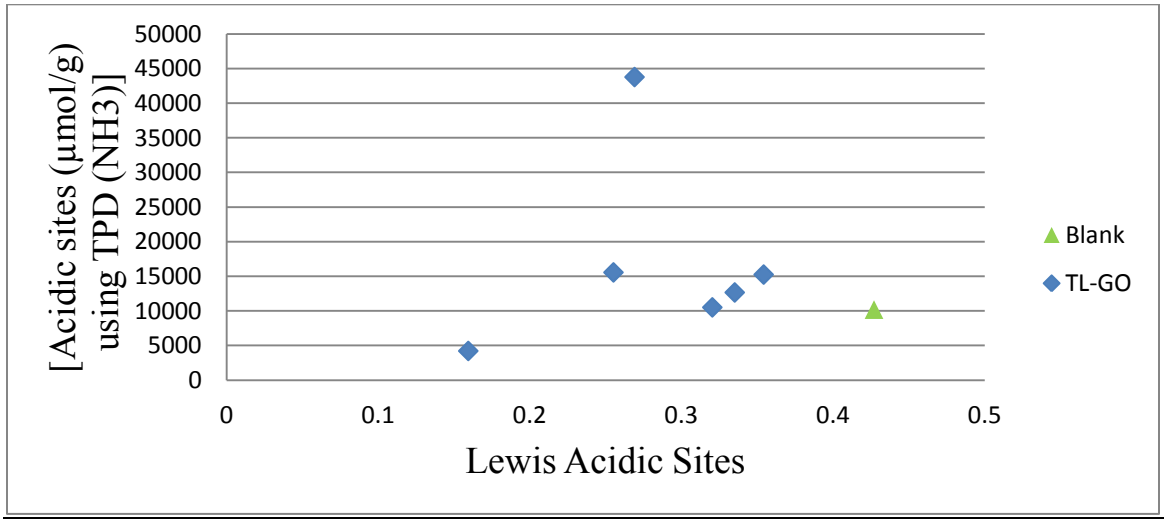

Figure (5-33) Relationship between the overall surface acidity measured by NH_3-TPD and the Lewis acidity measured by the perichromic TBSB/DTBSB pair for TL-GO samples.

5.5.2. ***Surface Polarity and Polarizability:***

Surface polarity of TL-GO samples which is measured by WB shows a complex variation with GO content, as presented in Figure (5-34). The reason for this requires further investigation, however it is believed that the large particle size distribution of the sample has a significant impact on its homogeneity, and the lack of the latter would lead to this complex variation.

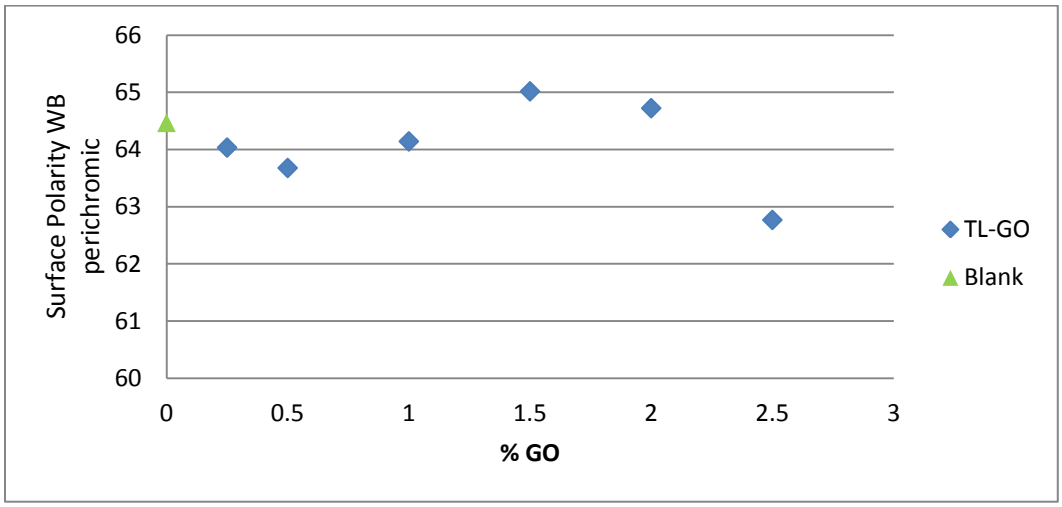

Figure (5-34) Variation of surface polarity of TL-GO samples as measured by WB perichromic dye with percentage content of GO.

On the other hand, the surface polarizability measured using β-Carotene perichromic dyes decreases with the increase in GO content. Increasing the GO content with highly oxygenated surface will decrease the surface polarizability of the formed TL-GO nanocomposites. However, the obtained negative values may result from limitations in the experimental determination and calculations for polar solid samples.

5.5.3. ***BET surface area and average pore diameter:***

Figures (5-35, 5-36 and 5-37) confirm that all TS-GO samples have lower surface area than the blank and the increase in GO content leads to the increase in the surface area. The average pore diameter decreases with increase in the GO amount and the pore diameter of all the samples is more than the blank average pore diameters, but shows a

decreasing trend with the increase in GO content. The presence of GO, with the associated formation of Ti-O-C bonds, seems to favor the formation of larger pores, with the subsequent decrease in BET surface area. However, as the GO content increases, and more Ti-O-C bonds form, the pore size decreases, with an observed increase in the surface area. This is reflected in the variation of the normalized average pore sizes. Table (5-7) contain the BET surface area, the average pore diameter and the average pore diameter per surface area as measured using the N_2 physisorption porosity analyzer for the TL-GO samples. N_2 adsorption isotherms of TL-GO samples are presented in Appendix (I).

Table (5-7) BET surface area, average pore diameter and average pore diameter per surface area data of TL-GO samples

% GO	Surface area (m^2/g)	BJH Adsorption average pore diameter (nm)	BJH Adsorption average pore diameter/surface area ($nm\ g/m^2$)
0	170	7.6	0.0445
0.25	151	8.8	0.0583
0.50	157	8.6	0.0546
1.00	155	8.2	0.0532
1.50	161	8.3	0.0512
2.00	164	8.1	0.0496
2.50	162	8.0	0.0493

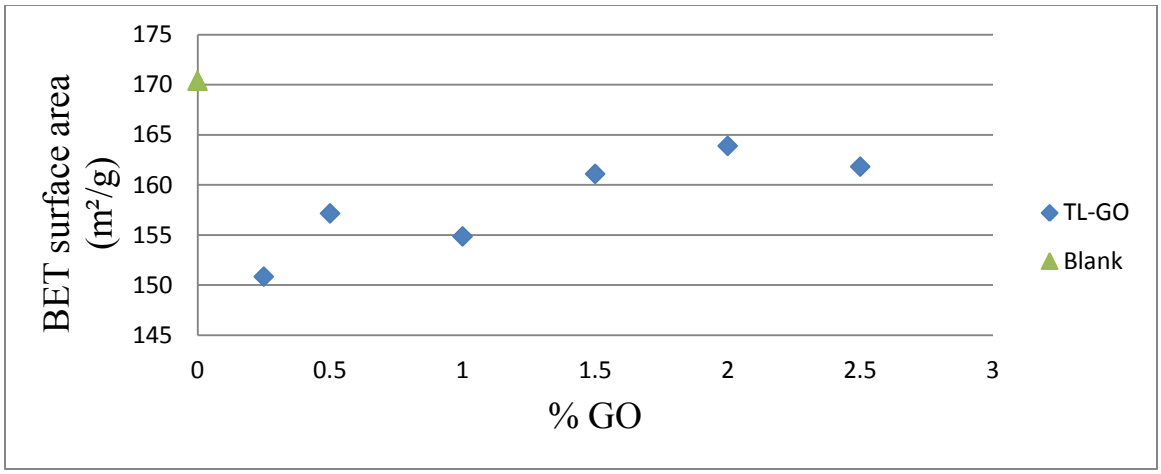

Figure (5-35) Variation of BET surface area of the TL-GO samples with percentage content of GO.

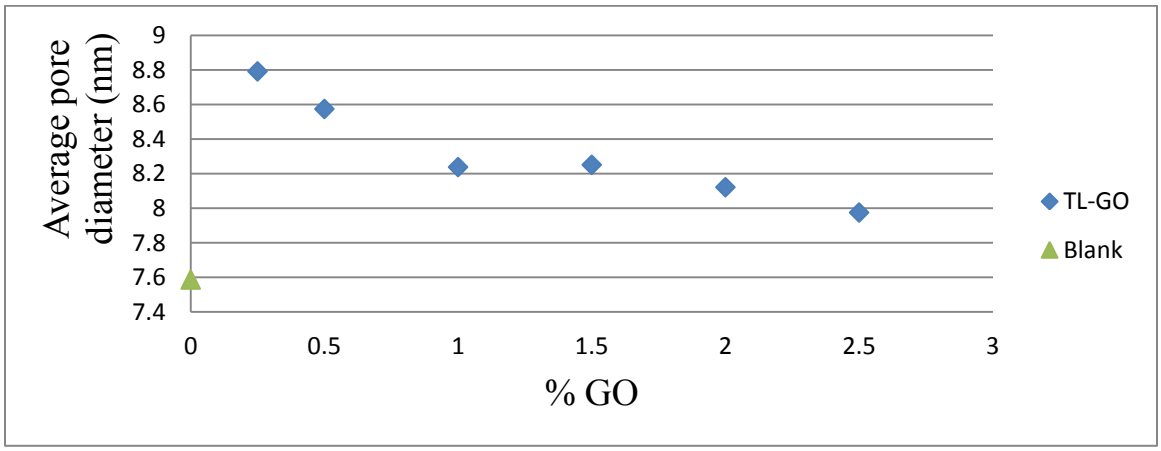

Figure (5-36) Variation of average pore diameter of TL-GO samples with percentage content of GO.

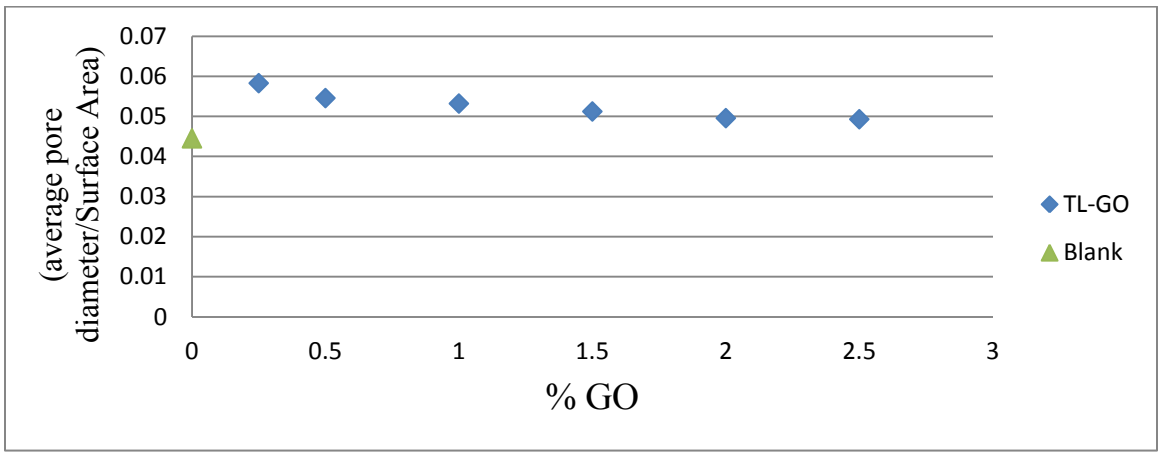

Figure (5-37) Variation of average pore diameter per surface area of TL-GO samples with percentage content of GO.

5.5.4. ***Band gap values for different TL-GO samples:***

UV–Vis DRS spectra shown in Figure (5-38) demonstrate a bathochromic shift in all GO containing samples and this red shift slightly increases with the increase in GO content. However, the variation of the GO amount in the formed nanocomposites does not lead to a noticeable change in the band gap energy (E_g) as discussed earlier and shown in Table (5-8).

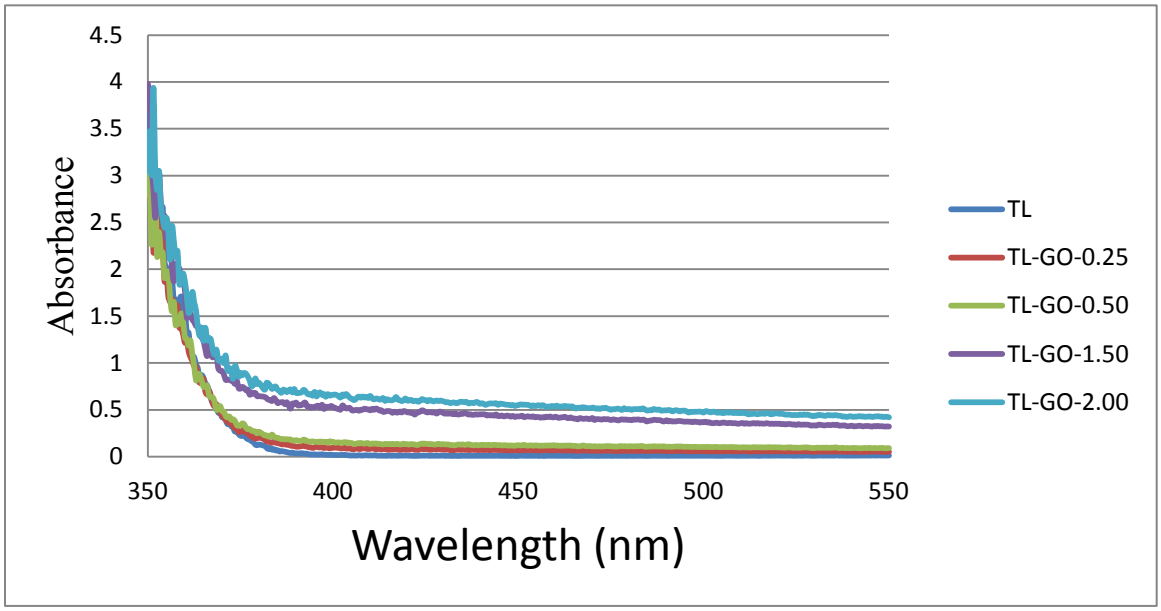

Figure (5-38) UV–Vis DRS spectra of TL-GO samples.

Table (5-8) Band gap values for different TL-GO samples.

Sample	TL	TL-GO-0.25	TL-GO-0.50	TL-GO-1.50	TL-GO-2.00
Band gap energy (eV)	3.341	3.338	3.333	3.307	3.294

5.5.5. ***Photocatalytic activity:***

All TL-GO samples are more active than the blank as presented in Table (5-9). The activity decreases linearly with increase in GO content with TL-GO-0.25 sample having the highest photocatalytic activity as presented in Figure (5-39). The kinetics of the photocatalytic degradation reaction exhibits zero order kinetics. The addition of GO to TiO_2 is observed to increase the photocatalytic degradation of MB due to the enhanced

adsorption of the dye molecules by the aromatic skeleton of GO. In addition, GO acts as electron sink for the photogenerated electrons causing a decrease in the electron-pair recombination rate and GO itself can play an important role as a photocatalyst in the photodegradation of MB [12], [144]. However, increasing the GO content may block the photocatalytic active sites on the surface of TiO_2 leading to decrease in the photodegradation activity [21].

Table (5-9) Zero order rate constants for the photocatalytic degradation of MB using TL-GO samples.

Sample	Rate constant $*10^{-8}$ (mole L^{-1} min^{-1})
TL	1.50
TL-GO-0.25	3.58
TL-GO-0.50	3.04
TL-GO-1.00	2.23
TL-GO-1.50	2.41
TL-GO-2.00	1.80
TL-GO-2.50	2.13

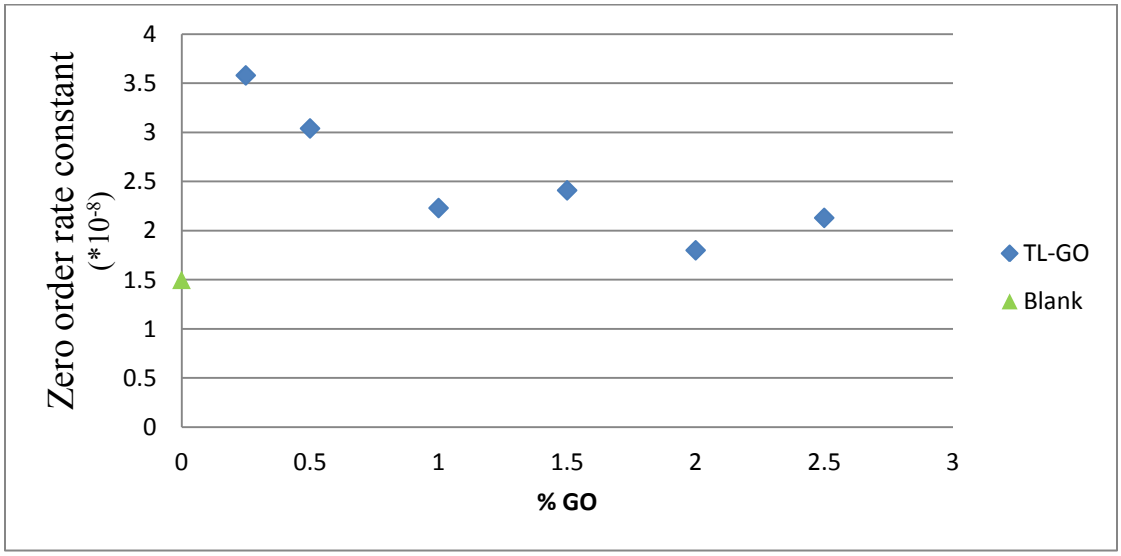

Figure (5-39) A plot of the zero order rate constants versus percentage content of GO for the photodegradation of MB using TL-GO samples.

5.5.6. ***Structural and compositional characteristics:***

A- ***XRD:***

XRD results reveal that the anatase crystalline phase of TiO_2 is the predominant phase and the crystalline structure of TiO_2 is not affected by the addition of GO as demonstrated in Figure (5-40). XRD peaks located at 2-theta values of 25.3°, 38°, 48°, 55° and 64° can be attributed respectively to (101), (004), (200), (105) and (204) crystal planes of anatase TiO_2 [23]. The main characteristic peak of GO at 24.5° is usually not observed due to masking effect of the strong anatase peak at 25.3° [32]. The small peak at 11°, attributed to the diffraction of GO, is not observed due to its low diffraction intensity and the disruption of GO exfoliation sheets in the formed nanocomposites samples. This has indeed been reported before [43], [49]. In addition, the very low XRD peak at 31° indicates the absence of brookite TiO_2 crystal phase [145], [146]. Furthermore, the absence of XRD peak at 27° of rutile TiO_2 crystal phase confirms that the main TiO_2 crystalline phase present in the TL-GO nanocomposites is the anatase phase with high photocatalytic activity [43].

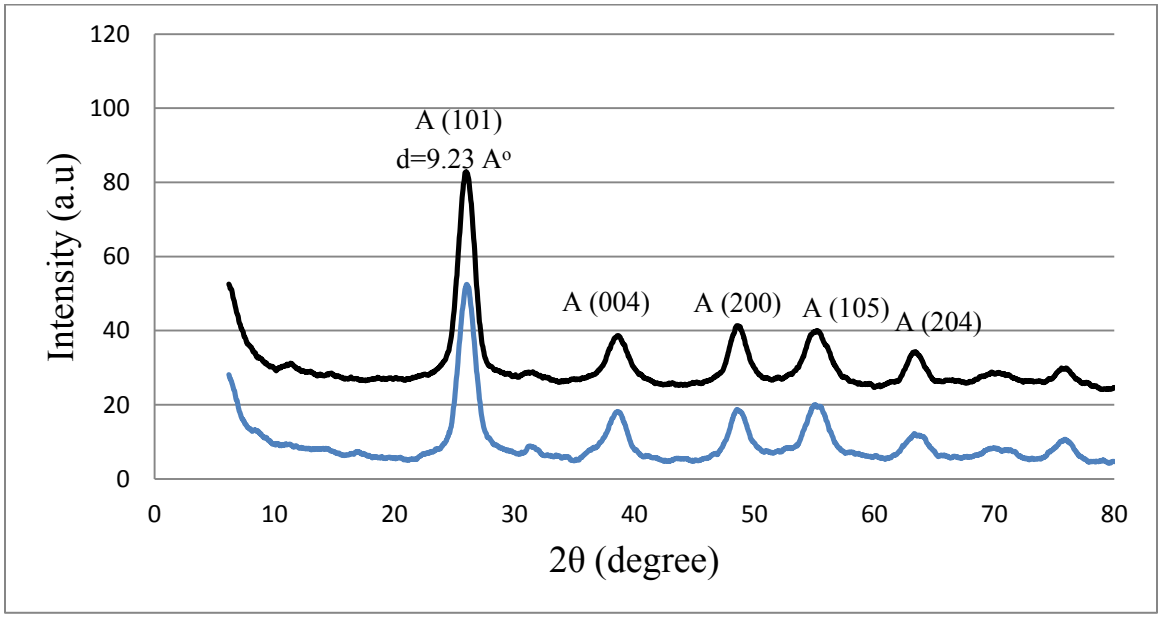

Figure (5-40) XRD spectra of TL (blue) and TL-GO-1.50 (black) as representative nanocomposite sample where, A is the Anatase crystalline phases of TiO_2.

*B- **FTIR:***

FTIR spectra for TL-GO nanocomposites show a strong band at ca. 600 cm^{-1} attributed to Ti-O-Ti and Ti-O-C bonds. The strong and broad band at ca. 3450 cm^{-1} is associated with the stretching vibration of surface hydroxyl groups on the TiO_2 surface. The presence of surface hydroxyl groups is further confirmed by the bending hydroxyl vibration at around 1640 cm^{-1}. The peak at 1640 cm^{-1} is assigned also to the bending vibration of molecular water, which would be present in the sample due to the water vapor from the atmosphere, and the aromatic ring vibration within the GO structure is located within the same region. Figure (5-41) shows the main absorption bands in the FTIR of TL-GO samples. The absence of the signal at 1720 cm^{-1} can show that the oxygenated surface of GO contains mainly hydroxyl group rather than ketonic or carboxyl groups [11], [43], [44].

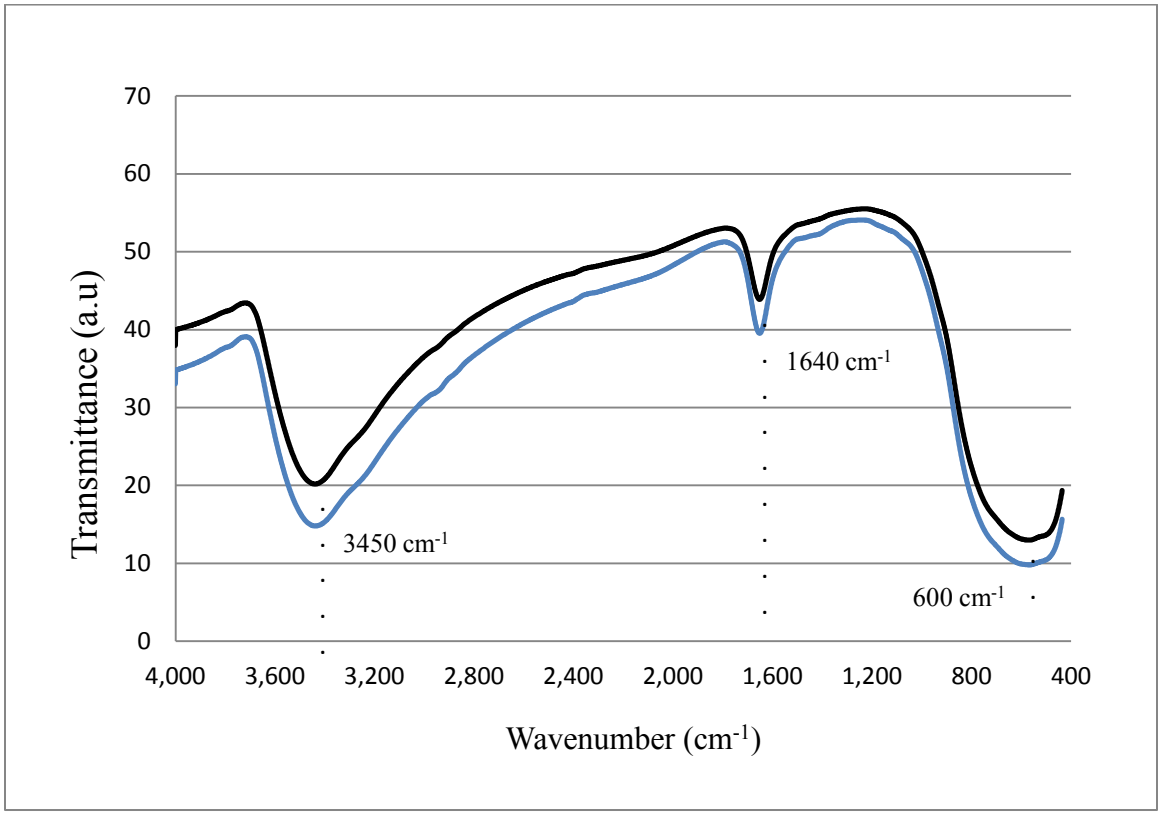

Figure (5-41) FTIR spectra of TL (black) and TL-GO-1.50 (blue) as representative nanocomposite sample.

*C- **Raman spectroscopy:***

Raman results presented in Figures (5-42) and (5-43) confirm the predominance of anatase crystal phase of TiO_2 and the formation of TL-GO nanocomposites. The Raman shift is plotted against normalized values because the intensity of the blank is much higher than the TL-GO samples. The anatase phase of TiO_2 is confirmed by the presence of vibration modes at ca. 142 cm^{-1} (E_g), 398 cm^{-1} (B_{1g}), 512 cm^{-1} (B_{1g} +A_{1g}) and 626 cm^{-1} (E_g) in all samples. The loss of fine structure in the TL-GO nanocomposites samples and the small shift in the 142 cm^{-1} (E_g) band may be attributed to the formation of Ti-O-C on the surface of the nanocomposites. The presence of GO in the nanocomposites is confirmed by the presence of G band (the E_{2g} mode of sp^2 carbon atoms) at 1590 cm^{-1} and the D band (the symmetric A_{1g} mode) at 1360 cm^{-1}. The G band at 1590 cm^{-1} confirms the presence of in-plane vibrations of sp^2 carbon structure and the D band at 1360 cm^{-1} is attributed to sp^3 defects in the GO structure. The comparable ratio between the G and D bands indicates the presence of GO with oxygenated sp^3 carbon structure [147]. The previous results confirmed the incorporation of TiO_2 and GO in the formed nanocomposites [12], [23], [25], [27], [38], [44], [49].

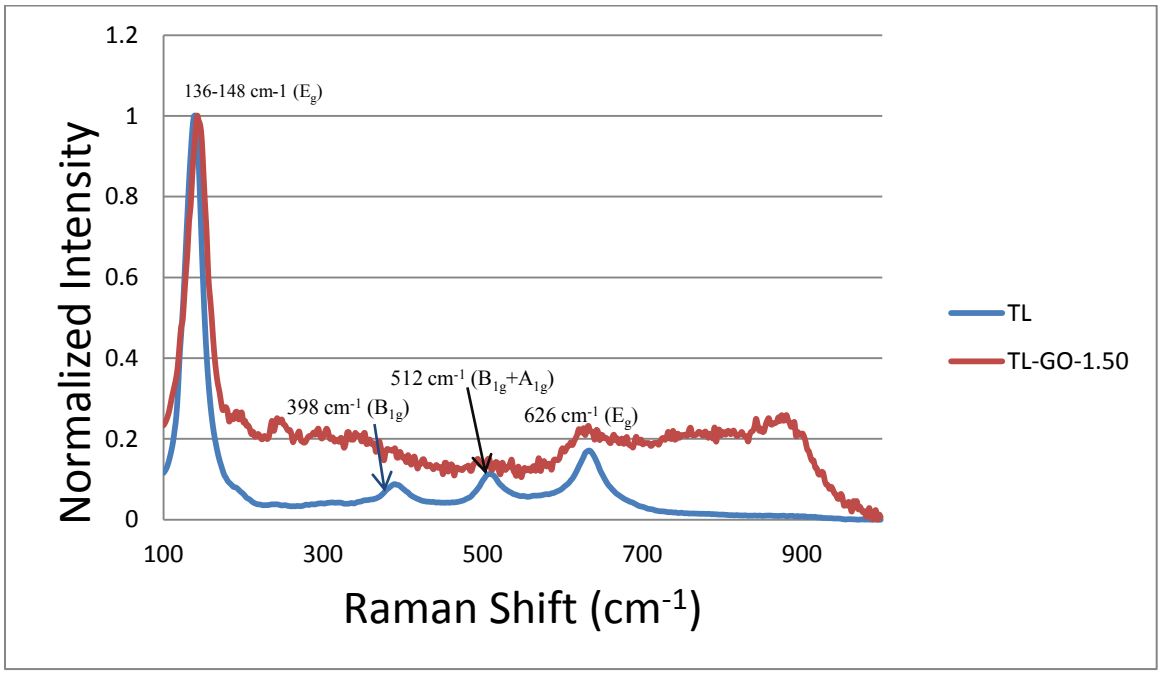

Figure (5-42) Raman spectra of TiO_2 in TL (blue) and TL-GO-1.5 (red) as representative nanocomposite sample.

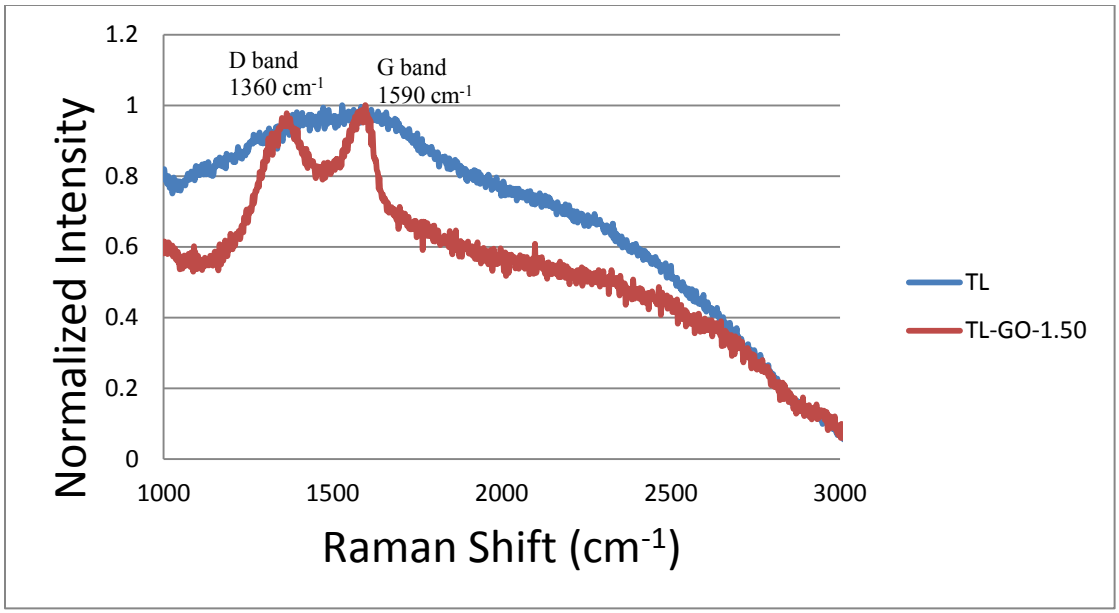

Figure (5-43) Raman spectra of carbon species in (blue) and TL-GO-1.5 (red) as representative nanocomposite sample.

5.6. *T large-G (TL-G) nanocomposites:*

5.6.1. *Surface acidity:*

Figure (5-44) shows lower Lewis acidity for the TL-G samples than the blank TiO_2. This is consistent with the formation of Ti-O-C bonds. The Ti-O-C bonds will decrease the number of Ti^{+n} cations on the surface of the nanocomposites leading to overall decrease in the number of Lewis acidic sites. Surface acidity of the TL-G nanocomposite samples shows limited variation with G content. This is probably due to sample heterogeneity resulting from the larger particle size distribution.

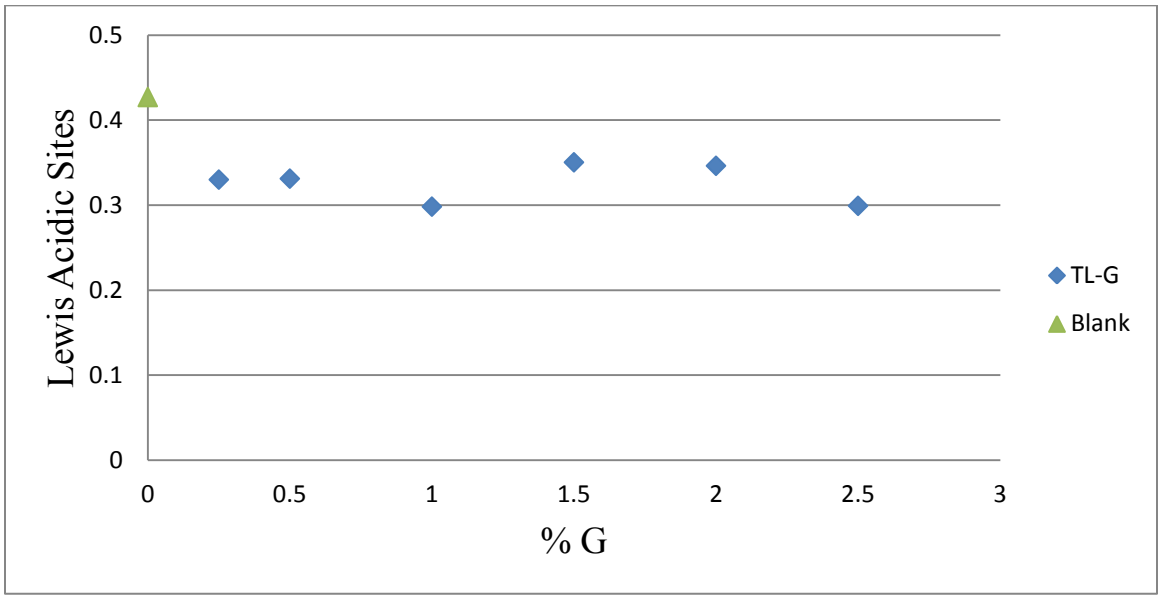

Figure (5-44) Variation of surface Lewis acidic sites of TL-G samples measured by perichromic TBSB/DTBSB pair with percentage content of G.

Figure (5-45) shows that there is no clear relationship between surface acidity as measured by NH_3-TPD and the G content in the TL-G samples. It is suspected that the large particle size distribution with its adverse impact on nanocomposite sample homogeneity led to these random data. Subsequently no correlation was found between the acidity data as measured by perichromic dyes adsorption and NH_3-TPD.

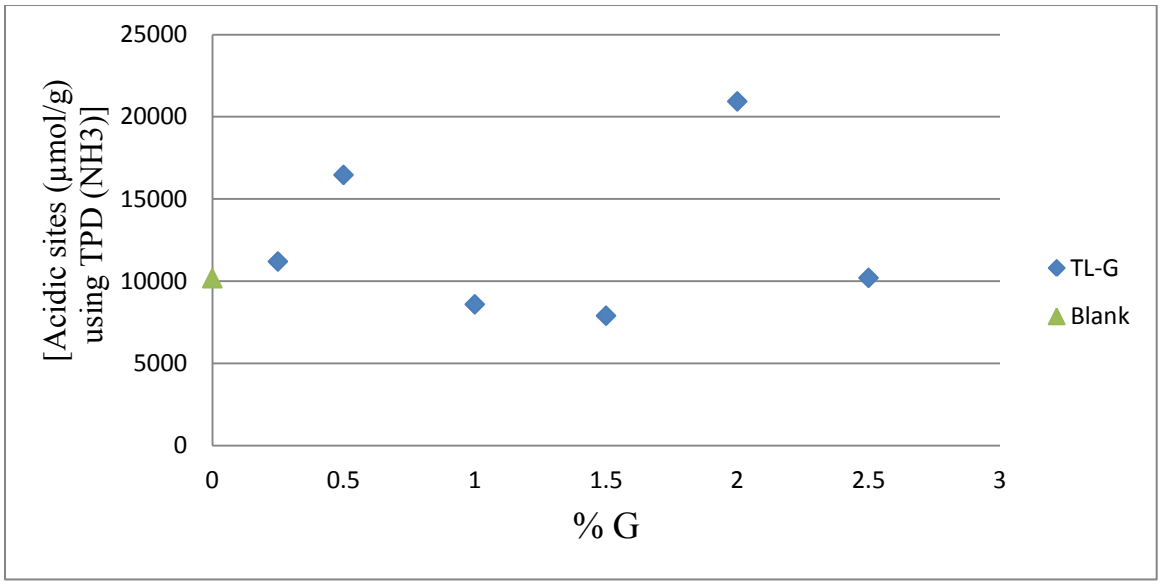

Figure (5-45) Variation of overall surface acidity of TL-G samples measured by NH_3-TPD with percentage content of G.

5.6.2. Surface Polarity and Polarizability:

Surface polarity of TL-G samples which is measured by WB perichromic dye shows that generally TL-G samples display higher surface polarity than the blank. Similarly to other data for these samples, no clear relation between surface polarity and G content can be found, as presented in Figure (5-46). This is also reflected in surface polarizability, where though the data show higher polarizability than the blank and a general increasing trend with G content, the data seem random. Higher polarizability than the blank is explained by the increase in van der Waal forces between the β-Carotene dye and the aromatic rings of the G sheets present in the samples, which would generally increase with the increase in G content. The randomness of the data probably reflects sample heterogeneity as is the case with other results for these samples.

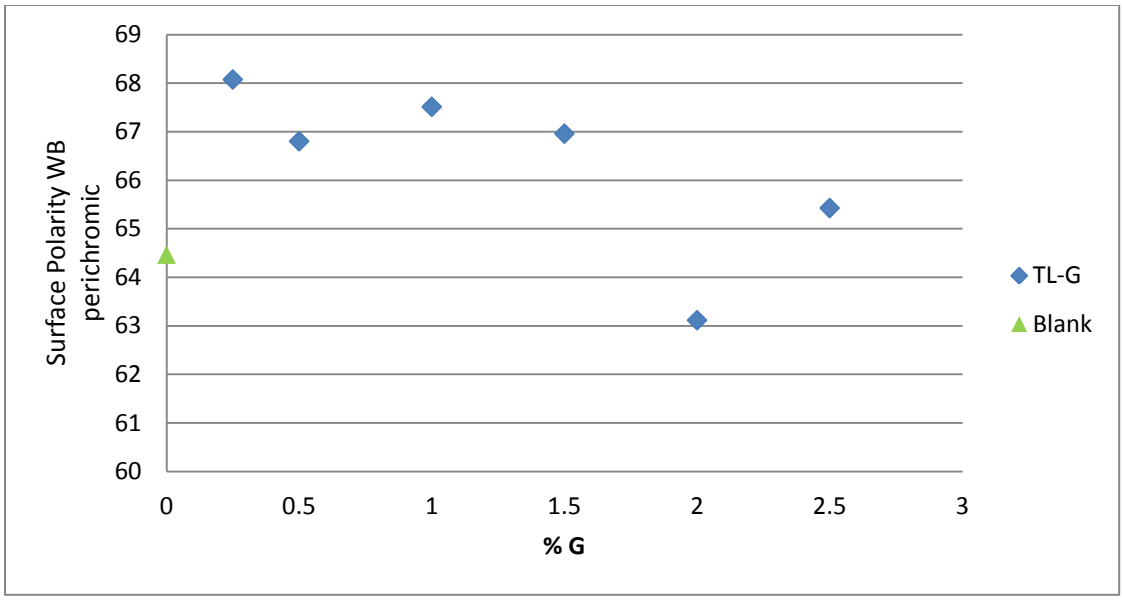

Figure (5-46) Variation of surface polarity of TL-G samples as measured by WB perichromic dye with percentage content of G.

5.6.3. BET surface area and average pore diameter:

Figures (5-47, 5-48 and 5-49) confirm that all TL-G samples are lower in surface area than the blank and the increase in the G content generally leads to an increase in the surface area. The possible aggregation of G sheets and packing of TiO_2 nanoparticles due to inhomogeneous distribution between TiO_2 and G may help to decrease the surface area than the blank. However, increasing the G content will slightly increase the surface area due to large surface area of G sheets. The average pore diameter is almost constant and higher than the blank. However, average pore diameter per surface area is decreasing with the increase in G content and all points are higher than the blank. Table (4-10) contains the BET surface area, the average pore diameter and the average pore diameter per surface area as measured using the N_2 physisorption porosity analyzer for the TL-G samples. N_2 adsorption isotherms of TL-G samples are presented in Appendix (I).

Table (5-10) BET surface area, average pore diameter and average pore diameter per surface area data of TL-G samples.

% G	Surface area (m^2/g)	BJH Adsorption average pore diameter (nm)	BJH Adsorption average pore diameter/surface area ($nm\ g/m^2$)
0	170	7.6	0.0445
0.25	111	9.0	0.0814
0.50	110	9.0	0.0823
1.00	125	8.6	0.0688
1.50	146	9.0	0.0615
2.00	154	8.3	0.0538
2.50	146	7.7	0.0527

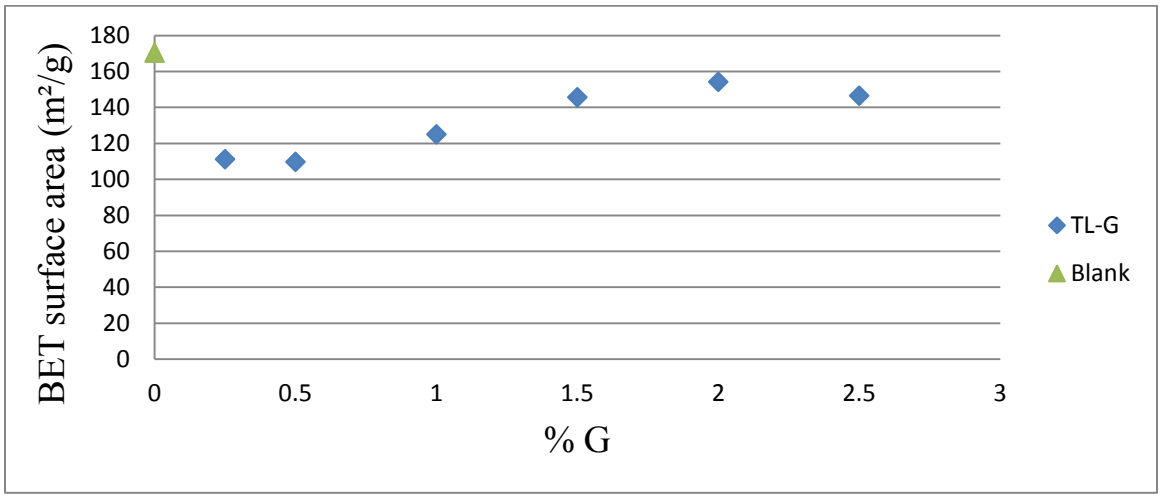

Figure (5-47) Variation of BET surface area of the TL-G samples with percentage content of G.

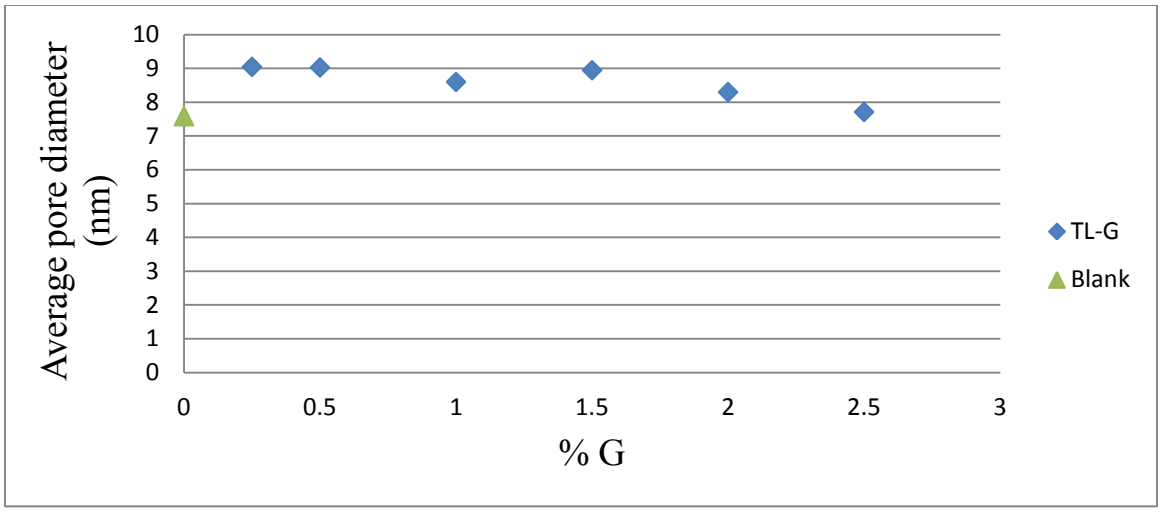

Figure (5-48) Variation of average pore diameter of TL-G samples with percentage content of G.

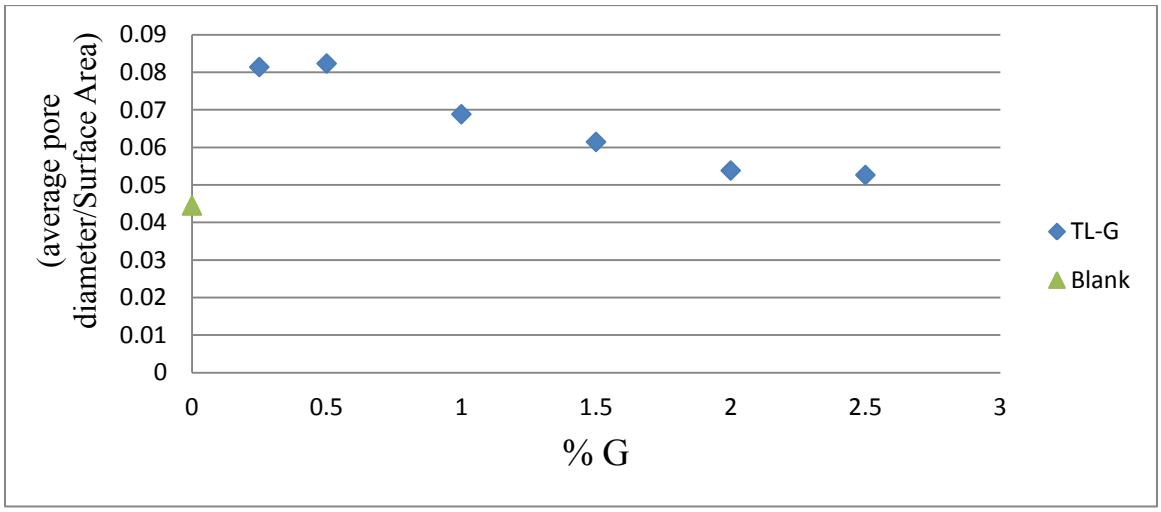

Figure (5-49) Variation of average pore diameter per surface area of TL-G samples with percentage content of G.

5.6.4. Band gap values for different TL-G samples:

UV–Vis DRS spectra shown in Figure (5-50) demonstrate a bathochromic shift in all G containing samples and this red shift slightly increases with the increase in G content. However, the variation of the G amount in the formed nanocomposites does not lead to a noticeable change in the band gap energy (E_g) as discussed earlier and shown in Table (5-11).

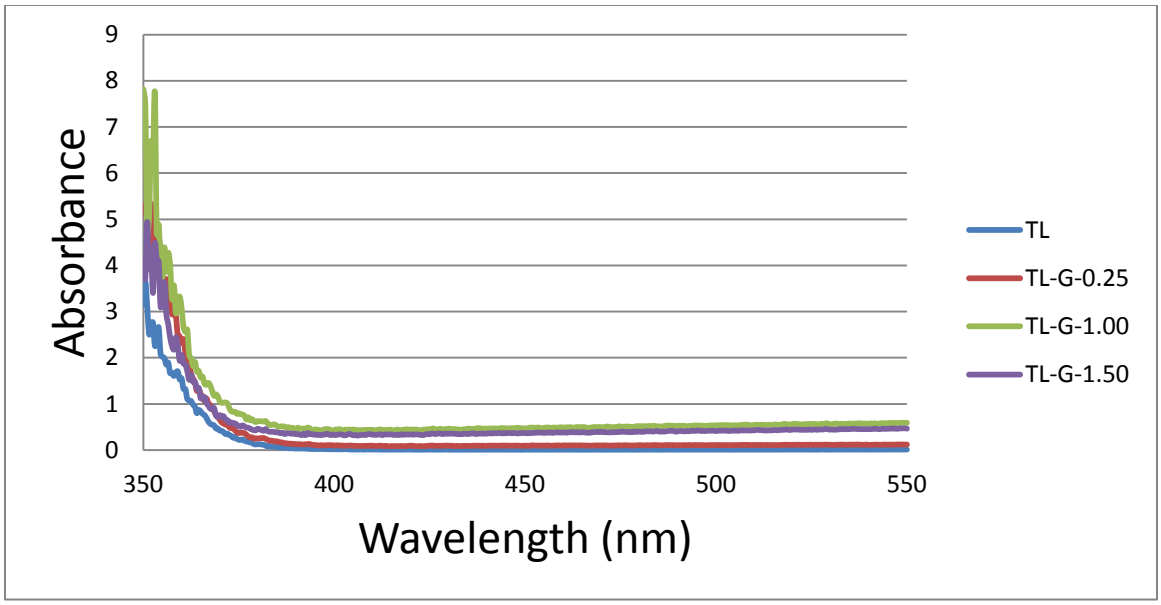

Figure (5-50) UV–Vis DRS spectra of TL-G samples.

Table (5-11) Band gap values for different TL-G samples.

Sample	**TL**	**TL-G-0.25**	**TL-G-1.00**	**TL-G-1.50**
Band gap energy (eV)	3.354	3.346	3.342	3.339

5.6.5. Photocatalytic activity:

All TL-G samples are more active than the blank as presented in Table (5-12). The photocatalytic activity decreases linearly with increase in G till 1.5% and increases again as presented in Figure (5-51). The kinetics of the photocatalytic degradation reaction exhibits zero order kinetics. The addition of G to TiO_2 increased the photocatalytic degradation of MB due to the enhanced adsorption of the dye molecules by the aromatic skeleton of G. In addition, G acts as electron sink for the photogenerated electrons causing a decrease in the electron-pair recombination rate and G itself can play an important role as a photocatalyst in the photodegradation of MB [12], [144]. However, increasing the G content may block the photocatalytic active sites on the surface of TiO_2 leading to overall decrease in the photodegradation activity [21]. The results of the

photodegradation show no clear variation with G content, similarly to other data for this set of samples, though all TL-G samples are more photoactive than the blank, as expected.

Table (5-12) Zero order rate constants for the photocatalytic degradation of MB using TL-G samples.

Sample	Rate constant $*10^{-8}$ (mole L^{-1} min^{-1})
TL	1.50
TL-G-0.25	2.23
TL-G-0.50	2.60
TL-G-1.00	2.13
TL-G-1.50	1.54
TL-G-2.00	2.41
TL-G-2.50	2.63

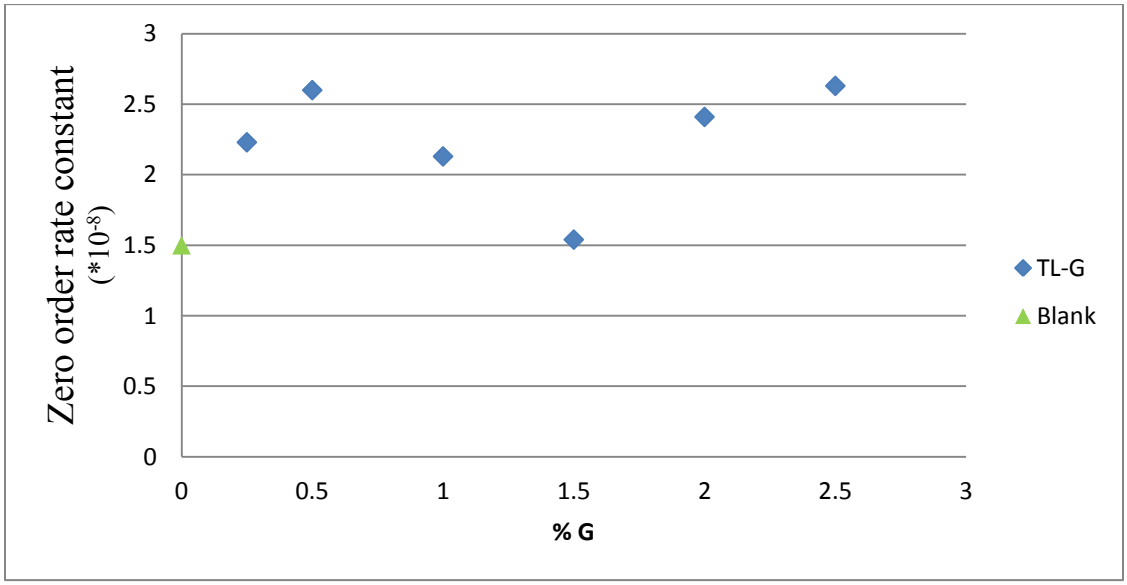

Figure (5-51) A plot of the zero order rate constants versus percentage content of G for the photodegradation of MB using TL-G samples.

5.6.6. ***Structural and compositional characteristics:***

A- ***XRD:***

XRD results reveal that the anatase crystalline phase of TiO_2 is the predominant phase and the crystalline structure of TiO_2 is not affected by the addition of G as demonstrated in Figure (5-52). XRD peaks located at 2-theta values of 25.3°, 38°, 48°, 55° and 64° can be attributed respectively to (101), (004), (200), (105) and (204) crystal planes of anatase TiO_2 [23]. The main characteristic peak of G at 24.5° is usually not observed due to masking effect of the strong anatase peak at 25.3° [32]. The small peak at 11°, attributed to the diffraction of G, is not observed due to its low diffraction intensity and the disruption of G exfoliation sheets in the formed nanocomposites samples. This has indeed been reported before [43], [49]. Furthermore, the absence of XRD peak at 27° of rutile TiO_2 crystal phase confirms that the main TiO_2 crystalline phase present in the TL-G nanocomposites is the anatase phase with high photocatalytic activity [43].

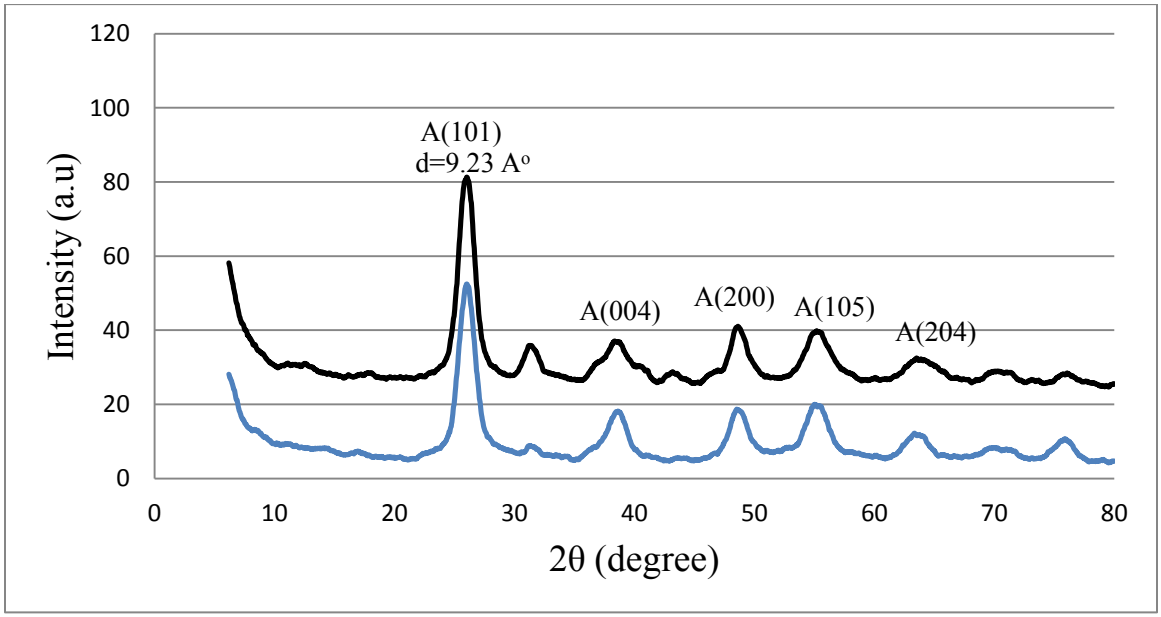

Figure (5-52) XRD spectra of TL (blue) and TL-G-1.50 (black) as representative nanocomposite sample where, A are the Anatase crystalline phases of TiO_2.

B- FTIR:

FTIR spectra for TL-G nanocomposites show a strong band at ca. 600 cm^{-1} attributed to Ti-O-Ti and Ti-O-C bonds. The strong and broad band at ca. 3450 cm^{-1} is associated with the stretching vibration of surface hydroxyl groups on the TiO_2 surface. The presence of surface hydroxyl groups is further confirmed by the bending hydroxyl vibration at around 1640 cm^{-1}. The peak at 1640 cm^{-1} is assigned also to the bending vibration of molecular water, which would be present in the sample due to the water vapor from the atmosphere, and the aromatic ring vibration within the G structure is located within the same region. Figure (5-53) shows the main absorption bands in the FTIR of TL-G samples. The absence of the signal at 1720 cm^{-1} can show that the surface of G contains no carbonyl functional groups [11], [43], [44]

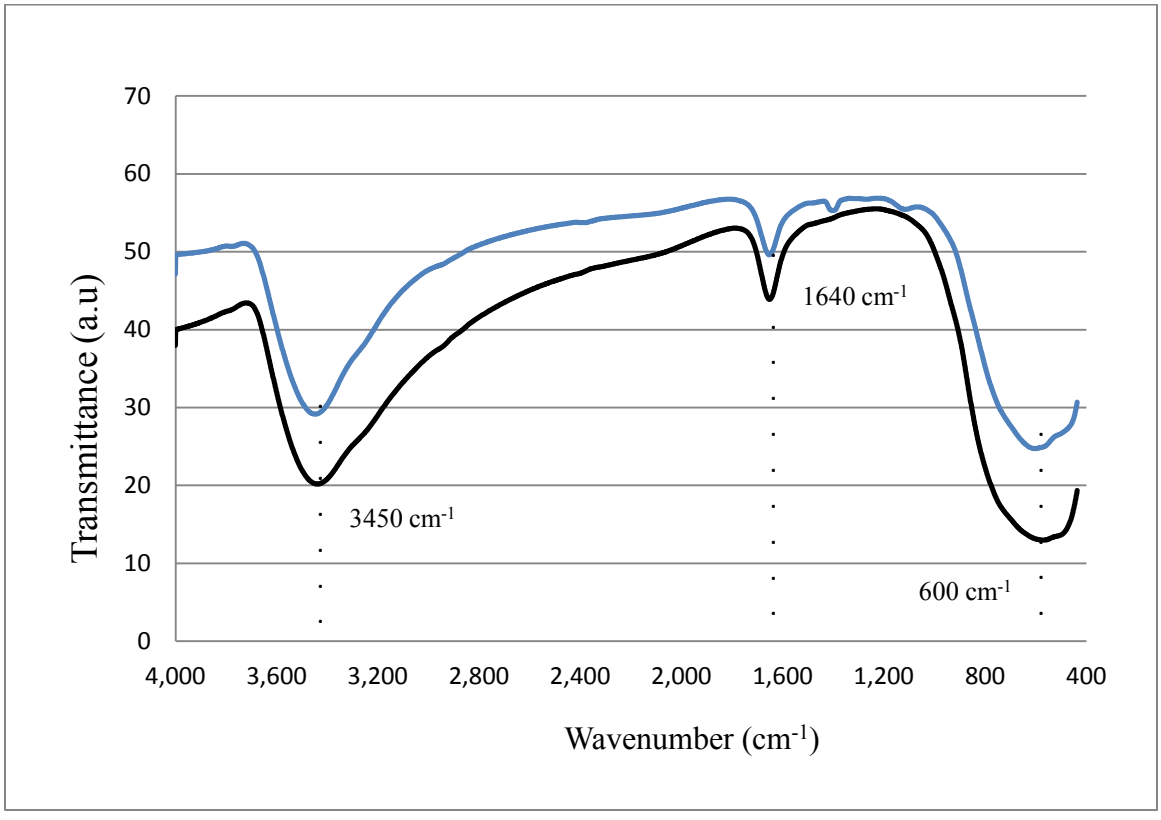

Figure (5-53) FTIR spectra of TL (black) and TL-G-1.50 (blue) as representative nanocomposite sample.

*C- **Raman spectroscopy:***

Raman results presented in Figures (5-54) and (5-55) confirm the predominance of anatase crystal phase of TiO_2 and the formation of TL-G nanocomposites. The Raman shift is plotted against normalized values because the intensity of the blank is much higher than the TL-G samples. The anatase phase of TiO_2 is confirmed by the presence of vibration modes at ca. 142 cm^{-1} (E_g), 398 cm^{-1} (B_{1g}), 512 cm^{-1} (B_{1g} +A_{1g}) and 626 cm^{-1} (E_g) in all samples. The loss of fine structure in the TL-G nanocomposites samples and the small shift in the 142 cm^{-1} (E_g) band may be attributed to the formation of Ti-O-C on the surface of the nanocomposites. The presence of G in the nanocomposites is confirmed by the presence of G band (the E_{2g} mode of sp^2 carbon atoms) at 1590 cm^{-1} and the D band (the symmetric A_{1g} mode) at 1360 cm^{-1}. The G band at 1590 cm^{-1} confirms the presence of in-plane vibrations of sp^2 carbon structure and the D band at 1360 cm^{-1} is attributed to sp^3 defects in the G structure. The high ratio between the D and G bands can be attributed to the higher defect density present in the TL-G samples [22]. These defects can interfere with the efficient photogenerated electron transfer on the surface of G with subsequent decrease in the photocatalytic activity with the increase in G content as confirmed by our results. The previous results confirmed the incorporation of TiO_2 and G in the formed nanocomposites [12], [23], [25], [38], [44], [49].

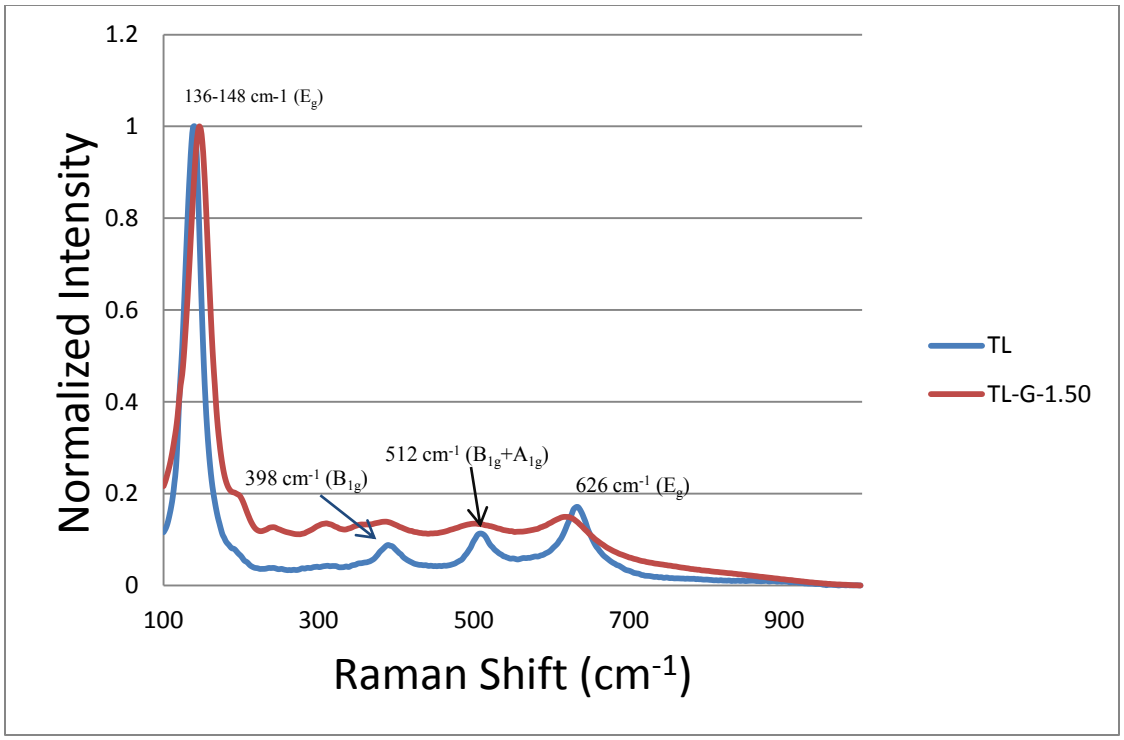

Figure (5-54) Raman spectra of TiO_2 in TL (blue) and TL-G-1.50 (red) as representative nanocomposite sample.

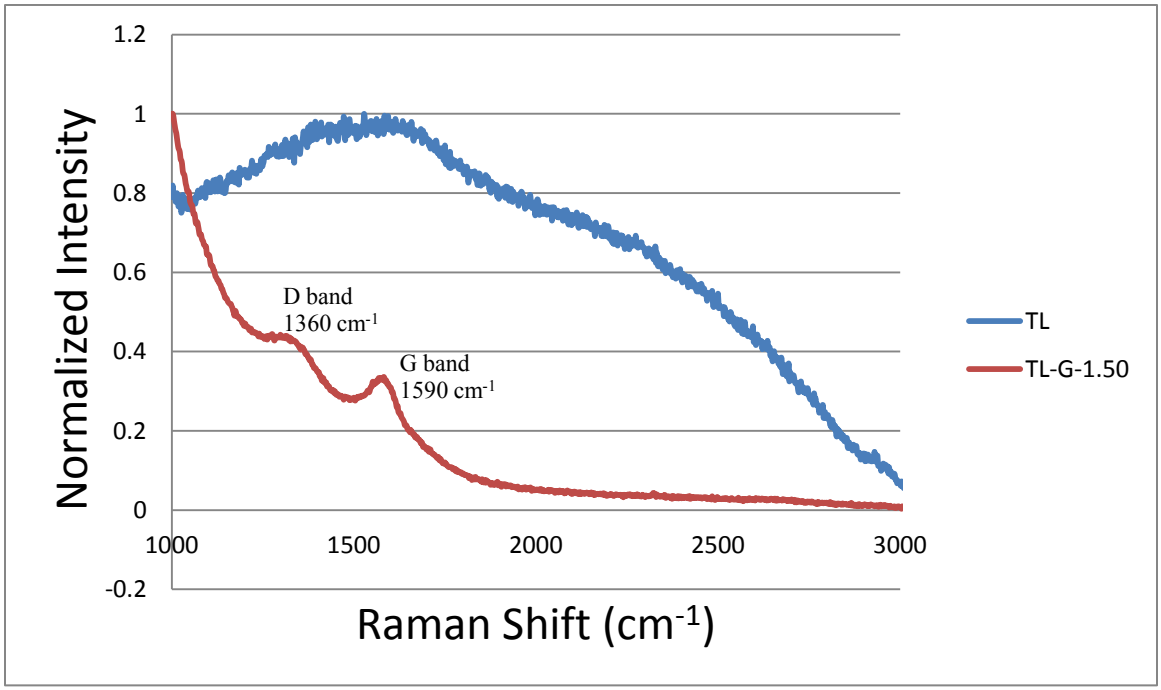

Figure (5-55) Raman spectra of carbon species in TL (blue) and TL-G-1.50 (red) as representative nanocomposite sample.

5.7. TL-GO versus TL-G Samples:

Lewis surface acidity measured using perichromic TBSB/DTBSB pair shows that both types of nanocomposites exhibit lower Lewis acidity than the blank sample and this can be attributed to the formation of Ti-O-C bonds which lead to this observed decrease [141]. In addition, the Lewis acidity decreases with the increase in the GO content due to the increased number of Ti-O-C bonds decreasing the amount of Ti^{+n} cations in the structure and consequently surface acidity. On the other hand, no clear variation is observed for surface acidity with G content. This is believed to be due to surface heterogeneity resulting from larger particle size distribution.

As for overall acidity, determined by NH_3-TPD, TL-GO samples exhibit higher overall surface acidity than the blank TL, while no clear correlation exist between the overall surface acidity and G content in the TL-G samples. The higher overall surface acidity of TL-GO samples is expected due to the highly oxygenated surface of GO [48]. On the other hand, the surface heterogeneity in TL-G samples resulted in the observed random data. No clear correlation exists between both types of measurements of surface acidity (perichromic dyes and NH_3-TPD) in both types of samples. This is due to limited homogeneity in TL containing samples due to larger particle size distribution.

Determination of surface polarity using WB dye shows a complex variation with G or GO contents. Similarly to other data for these samples, this complex variation is attributed to the surface heterogeneity in TL containing nanocomposites.

On the other hand, surface polarizability as measured using β-Carotene of TL-GO samples is generally lower than the blank and decreases linearly with the increase in the GO content, which is due to the highly oxygenated surface of GO that may decrease the interaction between the β-Carotene dye and the sample. On the contrary, addition of G increased surface polarizability and the increase is linear with the amount of added G. this is due to the increase in overall surface hydrophobicity associated with the presence of G [111].

The data of BET surface area show that both types of nanocomposites exhibit lower BET surface area than the blank sample and this can be attributed to the formation of Ti-O-C bonds in TL-GO samples [49]. In addition, the possible aggregation of G decreased the BET surface area of TL-G samples than the blank and TL-GO samples. Moreover, the

observed increase in the BET surface area with increase in the G or GO contents is believed to be due to the decrease in the normalized average pore sizes in both TL-GO and TL-G samples.

The bathochromic shifts observed in the UV-Visible DRS spectra confirm the decrease in the band gap energy (E_g) after the addition of GO and G. However, this decrease is unnoticeable. TL-GO and TL-G samples have higher photocatalytic degradation rates of MB dye compared to the blank and the photocatalytic activity decreases with the increase in GO or G content. However, TL-GO samples have higher values of photocatalytic degradation rate compared to TL-G which imparts the importance of surface area effects on the photodegradation rate. The higher BET surface area values of TL-GO samples have a prominent effect on the photocatalytic degradation of MB dye compared to TL-G samples with lower surface area [142].

Structural and compositional data measured using XRD, FTIR and Raman spectroscopy confirm the formation of the nanocomposites between TiO_2 and GO or G. FTIR spectra show almost the same characteristic peaks with a minor increase in intensity in the TL-GO samples compared to TL-G samples denoting the presence of more surface oxygenated functional groups [11]. Furthermore, the difference between TL-GO and TL-G samples can be clearly observed using Raman spectroscopy. The loss of fine structure in the Raman spectrum after the addition of GO or G is attributed to the formation of Ti-O-C bonds. The low frequency region (100-900 cm^{-1}) shows a blue shift to a higher frequency after the addition of GO or G confirming the formation of chemical bonds between TiO_2 and GO or G. The higher frequency region (1000-3000 cm^{-1}) confirms the presence of GO or G through the G and D bands [12], [38]. TL-G samples have lower intensity for the G and D bands than the TL-GO samples confirming the presence of GO in the TL-GO samples as reported by Štengl et al [149]. The loss of fine structure in the G and D bands of TL-G samples is believed to be due to the possible aggregation of G [38].

Anatase is the prominent crystalline phase of TiO_2 present in the samples and the crystalline structure is not greatly affected by the addition of GO or G as confirmed using XRD[23].

5.8. TS versus TL Samples:

5.8.1. TS-GO versus TL-GO Samples:

Lewis surface acidity measured using perichromic TBSB/DTBSB pair shows that both types of nanocomposites exhibit lower Lewis acidity than the blank sample and this can be attributed to the formation of Ti-O-C bonds which lead to this observed decrease [141]. In addition, the Lewis acidity decreases with the increase in the GO content due to the increased number of Ti-O-C bonds decreasing the amount of Ti^{+n} cations in the structure and consequently surface acidity. The comparable Lewis surface acidity values of TS-GO and TL-GO samples is expected due to the presence of GO in both types of nanocomposites. Furthermore, the blank TS show higher Lewis acidity than the blank TL which can be attributed to the availability of more Ti^{+n} cations, which is probably due to the preparation routine used leading to less cross-linking for TS samples. .

As for overall acidity determined by NH_3-TPD, both types of nanocomposites exhibit higher overall surface acidity than their corresponding blank samples. In addition, TL-GO samples show higher overall surface acidity than TS-GO samples. This is attributed to the lower overall surface acidity of the blank TS than the blank TL. This is an indication that the decrease in TiO_2 particle size is associated with the decrease in overall surface acidity of the blank TiO_2 samples. Linear correlation exists between both types of measurement of surface acidity (perichromic dyes and NH_3-TPD) in TS-GO samples. This is an indication that perichromism can be used to elucidate the surface Lewis acidity of TS-GO nanocomposites. On the other hand, no clear correlation exists between both types of measurement of surface acidity in TL-GO samples due to the lack of surface homogeneity.

Determination of surface polarity using WB dye shows that TS-GO samples have higher surface polarity than TL-GO samples. The lower surface polarity of TL containing samples may be due to the possible packing of TiO_2 nanoparticles. On the other hand, surface polarizability as measured using β-Carotene, of both TS-GO and TL-GO samples, is lower than the blank and decreased linearly with the increase in the GO content. This is due to the presence of highly oxygenated polar surface of GO [111], [142].

The BET surface area data show that both types of nanocomposites exhibit lower BET surface area than their corresponding blank samples and this can be attributed to the

formation of Ti-O-C bonds in TS-GO and TL-GO samples. In addition, the higher BET surface area values of TL-GO samples than TS-GO samples, is attributed to the high BET surface area of the blank TL which is associated with the smaller pores within the TiO_2 matrix resulting from the preparation routine leading to more cross-linking for TL samples. Moreover, the effect of GO content on the BET surface area values of TL-GO samples is more significant than the values of TS-GO samples.

The bathochromic shifts observed in the UV-Visible DRS spectra confirm the decrease in the band gap energy (E_g) after the addition of GO. However, this decrease is unnoticeable. TS-GO and TL-GO samples have higher photocatalytic degradation rates of MB dye compared to their corresponding blank samples, TS and TL respectively, and the photocatalytic activity decreases with the increase in GO content [35]. However, TS-GO samples have higher values of photocatalytic degradation rate compared to TL-GO which imparts the importance of surface homogeneity and narrow particle size distribution on the photocatalytic degradation rates [23].

FTIR spectra show almost the same characteristic peaks with a minor increase in intensity in the TL-GO samples compared to TS-GO samples denoting the presence of more surface oxygenated functional groups [43], [44]. Raman spectroscopy confirms the interactions between TiO_2 and GO [27]. The higher ratio between D and G bands intensity in the TS-GO samples indicates less stacking of the GO than the TL-GO samples and higher photocatalytic activity [149].

Anatase is the prominent crystalline phase of TiO_2 present in the samples and the crystalline structure is not greatly affected by the addition of GO as confirmed using XRD [23].

5.8.2. TS-G versus TL-G Samples:

Lewis surface acidity measured using perichromic TBSB/DTBSB pair shows that both types of nanocomposites exhibit lower Lewis acidity than the blank sample and this can be attributed to the formation of Ti-O-C bonds which lead to this observed decrease [141]. However, the change in G content in TS-G and TL-G samples shows no clear variation in the Lewis surface acidity. This is indication that the amount of added G has no significant effect on the Lewis surface acidity.

As for overall acidity, determined by NH_3-TPD, TS-G samples exhibit higher overall surface acidity than the blank TS, while no clear correlation exist between the overall surface acidity and G content in the TL-G samples. The higher overall surface acidity of TS-G samples may be attributed to the interactions between TiO_2 and G leading to a better availability of acidic hydrogen of TiO_2. On the other hand, the surface heterogeneity in TL-G samples resulted in the observed random data. Linear correlation exists between both types of measurement of surface acidity (perichromic dyes and NH_3-TPD) in TS-G samples. This is an indication that perichromism can be used to elucidate the surface Lewis acidity of TS-G nanocomposites. However, no clear correlation exists between both types of measurements of surface acidity in TL-G samples. This is due to lack of homogeneity in TL-G samples due to larger particle size distribution.

Determination of surface polarity using WB dye shows that both TS-G and TL-G samples have higher surface polarity than the blank. However, the inconsistency in the surface polarity data of both TS-G and TL-G samples can be attributed to the hydrophobic nature of G, the possible stacking of G and the heterogeneity in the TL-G samples. On other hand, the surface polarity of the blank TS shows higher surface polarity than the blank TL which may indicates the possible packing of TiO_2 nanoparticles in the TL samples. On the other hand, surface polarizability as measured using β-Carotene, of both TS-G and TL-G samples, is higher than their corresponding blank and increases linearly with the increase in the G content. The surface polarizability values of TS-G are more significant which imparts the better homogeneity in the TS-G samples compared to TL-G samples [119].

TS-G samples have almost similar surface area values as the TS blank, whereas TL-G samples have lower values than the TL blank. The possible stacking of G decreased the

BET surface area of TL-G samples than the blank due to limitations in the formation of Ti-O-C bonds. The same findings were observed, to a much lesser extent, for TS-G samples.

The bathochromic shifts observed in the UV-Visible DRS spectra confirm the decrease in the band gap energy (E_g) after the addition of G. However, this decrease is unnoticeable. TS-G and TL-G samples have higher photocatalytic degradation rates of MB dye compared to their corresponding blank samples, TS and TL respectively, and the photocatalytic activity decreases with the increase in G content. However, TS-G samples have higher values of photocatalytic degradation rate compared to TL-G which imparts the importance of surface homogeneity, small particle size and narrow particle size distribution on the photocatalytic degradation rates [23].

Raman spectroscopy confirms the formation of the nanocomposites between TiO_2 and G. FTIR spectra show almost the same characteristic peaks with a minor increase in intensity in the TS-G samples compared to TL-G samples. TL-G samples have lower intensity than the blank which may be attributed to aggregation of both TiO_2 nanoparticles and stacking of G. The higher ratio between D and G bands intensity in the TS-G samples indicates better incorporation of G and TiO_2 in the nanocomposite and higher photocatalytic activity [149].

Anatase is the prominent crystalline phase of TiO_2 present in the samples and the crystalline structure is not greatly affected by the addition of GO as confirmed using XRD [23].

5.9. ***FESEM:***

FESEM images confirmed the loading of TiO_2 nanoparticles on G and GO nanosheets. However, the effect of different concentrations of G or GO and the difference in TiO_2 particle size is not clear in the FESEM images. Figures (5-56), (5-57), (5-58) and (5-59) show representative FESEM images of TiO_2-GO and TiO_2-G nanocomposites.

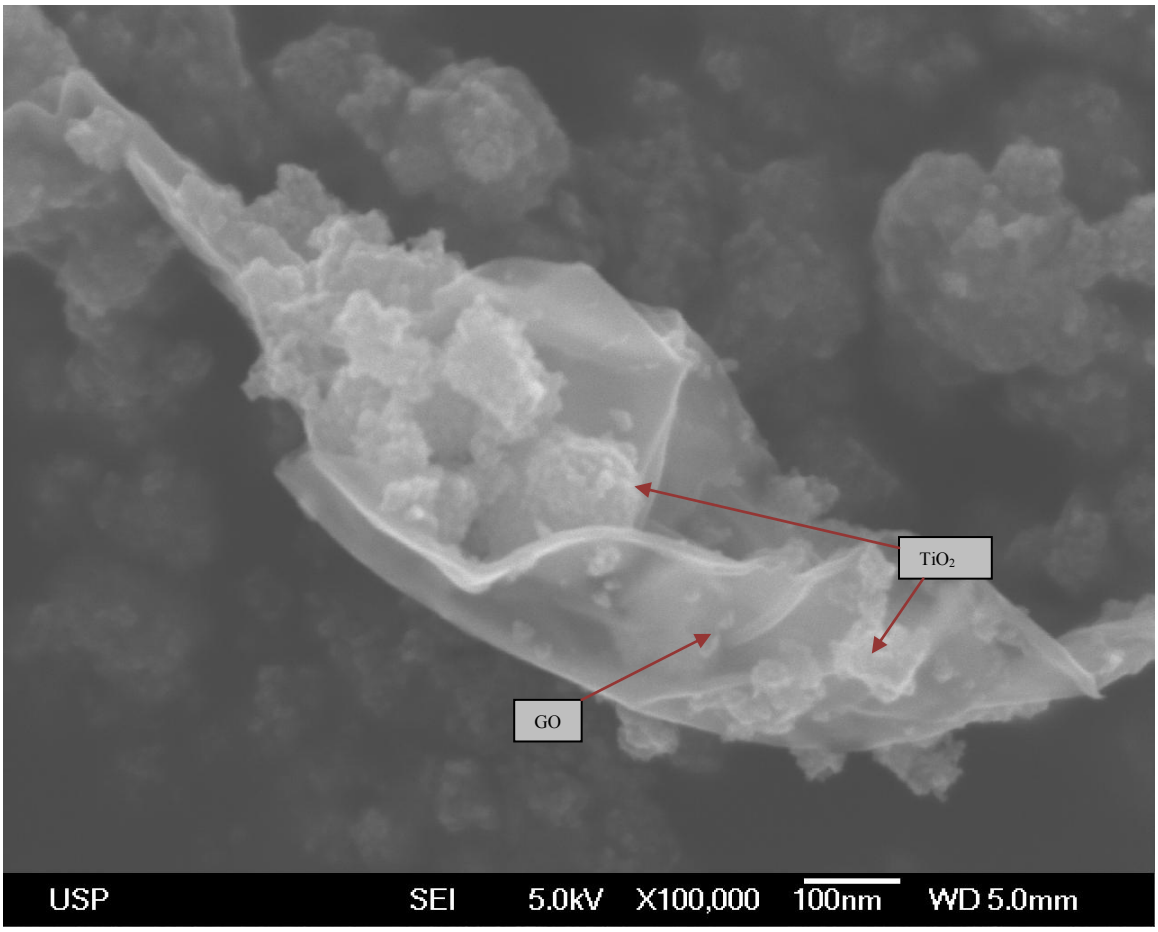

Figure (5-56) FESEM of TiO_2-GO-2.50 as representative nanocomposite sample showing the loadings of TiO_2 nanoparticles on GO nanosheets using magnification x100000.

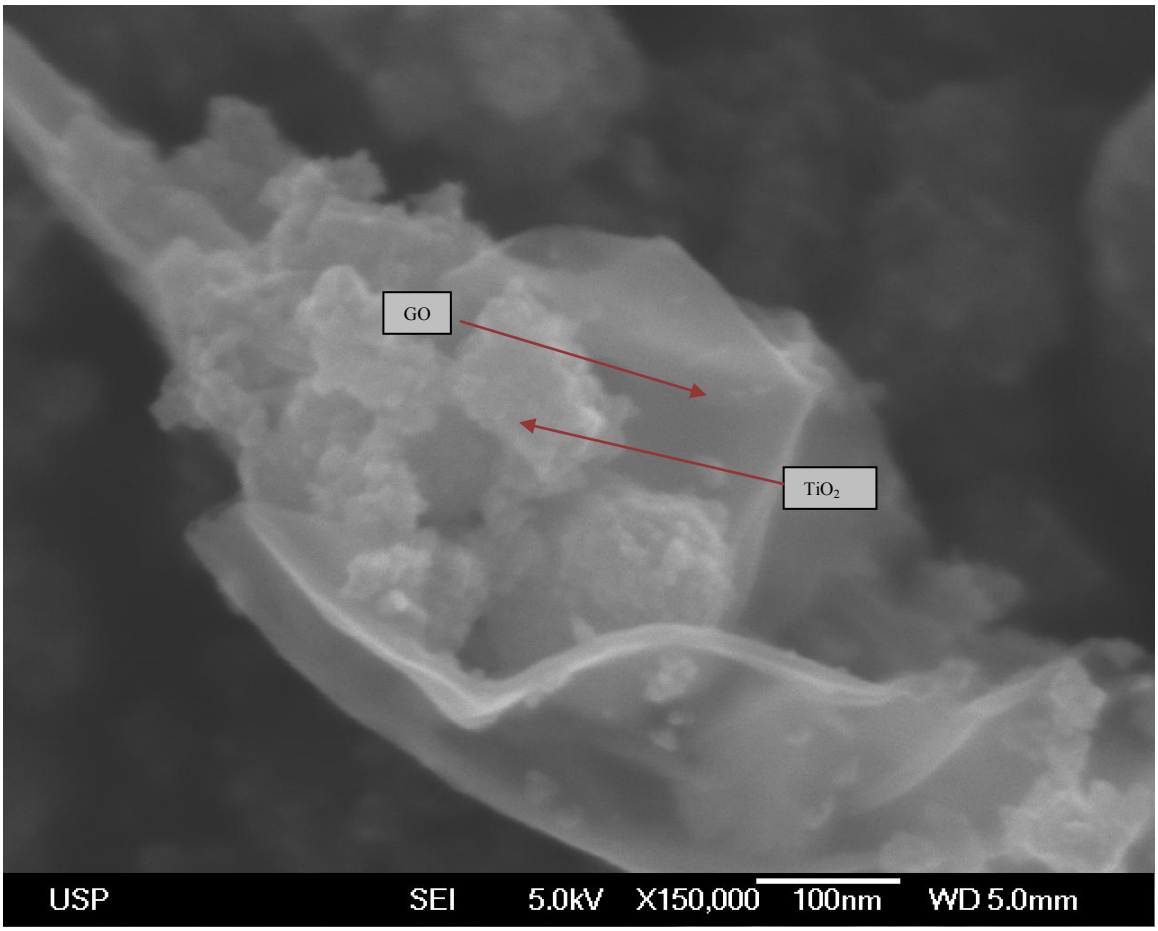

Figure (5-57) FESEM of TiO_2-GO-2.50 as representative nanocomposite sample showing the loadings of TiO_2 nanoparticles on GO nanosheets using magnification x150000.

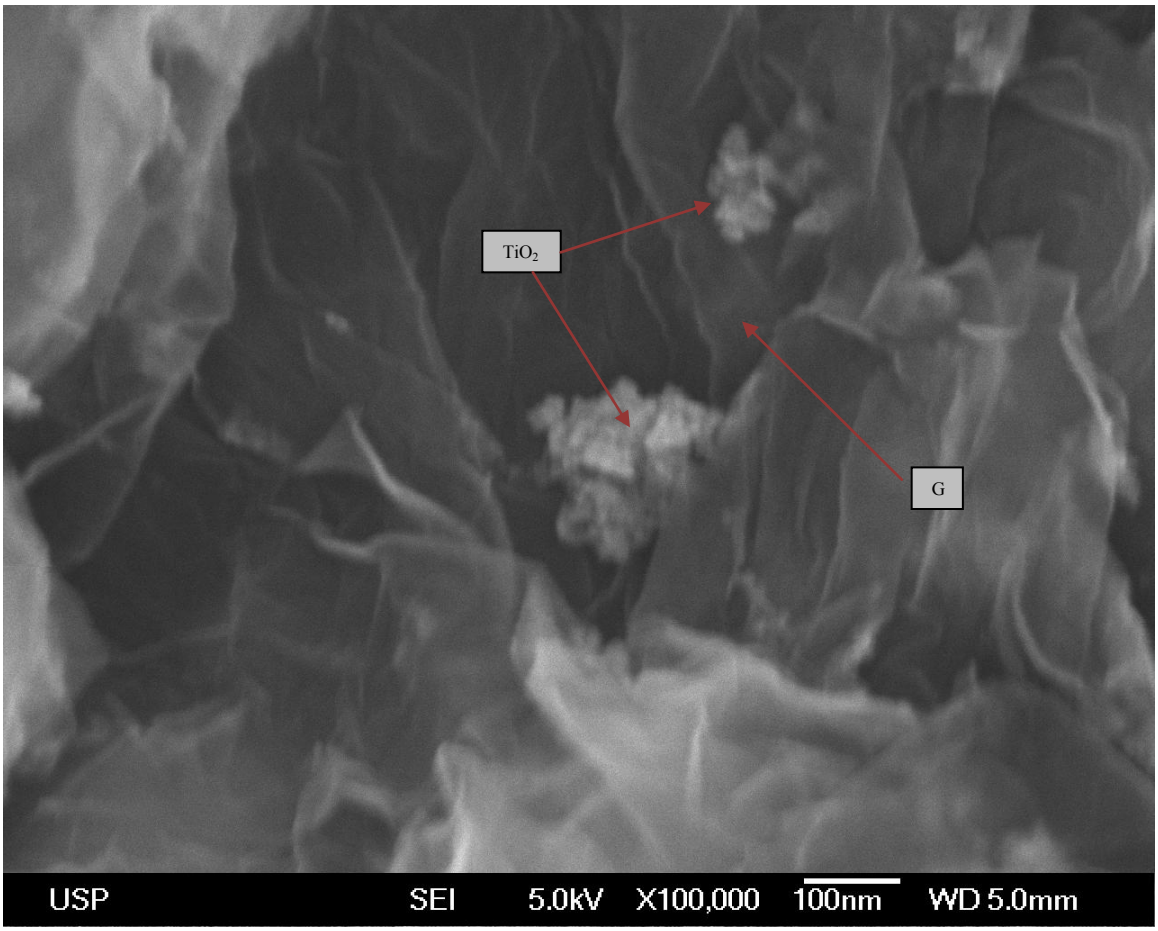

Figure (5-58) FESEM of TiO_2-G-2.50 as representative nanocomposite sample showing the interaction between the loadings of TiO_2 nanoparticles on G sheets using magnification x100000.

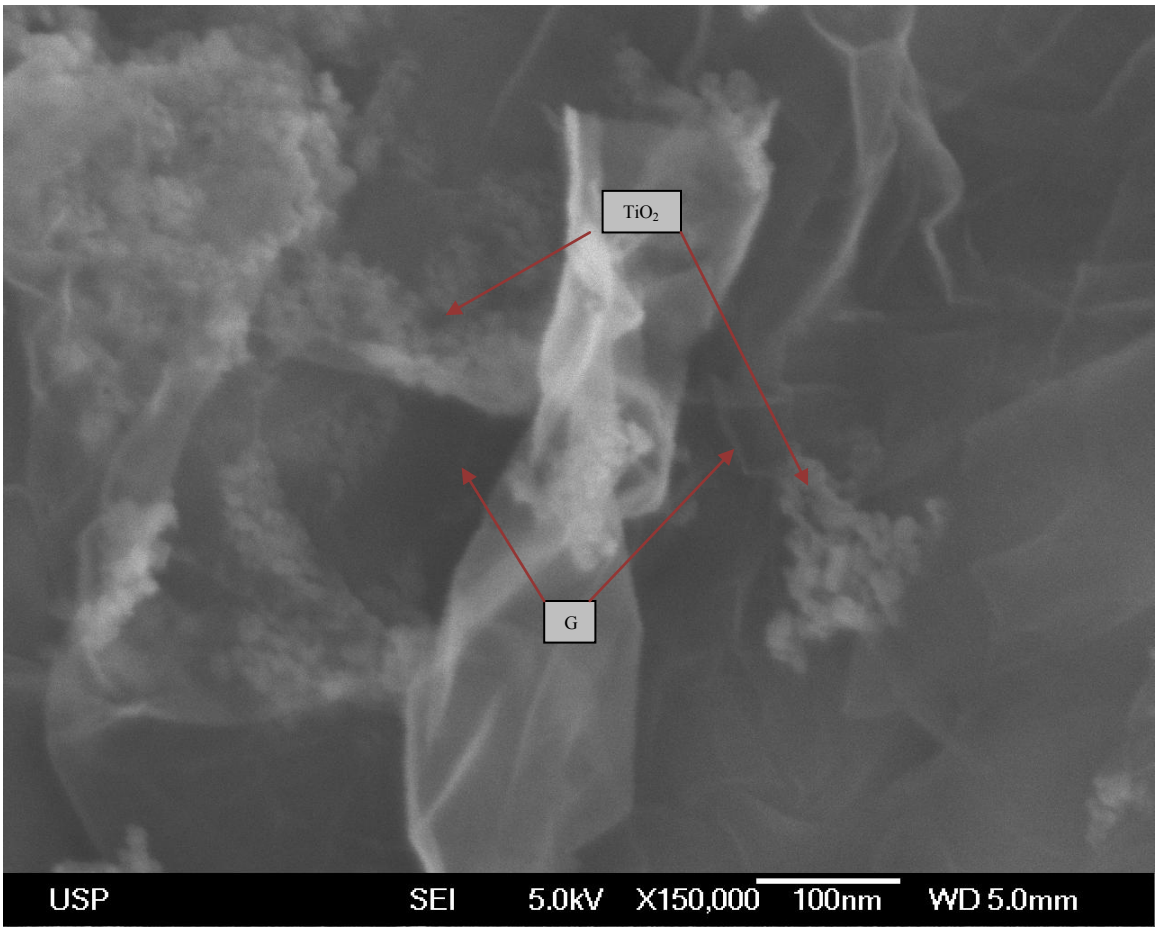

Figure (5-59) FESEM of TiO_2-G-2.50 as representative nanocomposite sample showing the loadings and good distribution of TiO_2 nanoparticles on G nanosheets using magnification x150000.

Chapter (6)
Conclusions and Future Work

6.1. Conclusions:

This study is aimed at investigating the effect of introducing G or GO on the photocatalytic activity of TiO_2, using the oxidation of MB as a model reaction. A central part of this thesis is to investigate the surface properties of the produced TiO_2-G and TiO_2-GO nanocomposites by several *independent techniques*, because the catalytic efficiency is intimately linked to surface properties. The properties investigated are listed below, along with techniques employed:

- Surface area and porosity, studied by nitrogen adsorption;
- Total surface acidity (Brønsted plus Lewis acidity) determined by NH_3-TPD , and surface Lewis acidity, determined by perichromic dyes. The results of both techniques were correlated.
- Surface empirical polarity and polarizability, studied with perichromic dyes.
- Surface morphology, studied by SEM.
- Additional information on surface properties was obtained from the results of UV-Visible, FTIR, and Raman spectroscopy.

The nanocomposites synthesized were tested as catalysts for the photo-oxidation of MB, and the results correlated with their composition, and compared to those obtained with unmodified TiO_2. The main findings of this work are presented below.

-Particle size of TiO_2 nanoparticles

TiO_2 particle sizes differ with the method of preparation of TiO_2, adding DI drop by drop or at once, and found to be 436 ±59 nm for TL and 251 ±32 nm for TS. In TL samples, prepared by drop by drop addition of DI, the condensation-polymerization reaction is taken place in a slower rate. This allows the formation of more cross-linking in TL sample with smaller pores and larger surface area.

-Formation of the nanocomposites

The addition of G or GO to TiO_2 shows that the nanocomposite formation is ascribed to chemical bond formation and this chemical interaction is reflected in the G and GO peaks in the Raman spectra. However, the formation of the nanocomposites did not have any

negative impact on the structure of TiO_2 or G/GO as evidenced by FTIR. Moreover, the addition of G or GO did not affect the crystal structure of TiO_2 as evidenced by XRD.

-*Catalytic performance of the synthesized nanocomposites*

Except for one case (corresponding to 4%), all nanocomposites showed higher catalytic efficiency than unmodified TiO_2. The rate enhancement ranged from 9.2 to 69.2% for TS, and 18.8 to 237.5% for TL, showing the clear advantage of using nanocomposites as photocatalysts for pollutants.

- *Rationale for the photocatalytic activity of nanocomposites*

The photocatalytic activity of the samples are dependent on several factors such as surface acidity, surface area and, to a much lesser extent, the change in band gap energy. The overall effect is a complex combination of all these factors. At the moment, therefore, it is not warranted to determine the effect of each of them on the photocatalytic activity. In addition, the effect of the change in band gap energy is overridden by the other two factors with much lesser effect on the photocatalytic activity.

- *Analysis of the effects of introducing G and GO on the surface properties of the nanocomposites.*

- Surface acidity

The addition of G or GO to TiO_2 increased the overall surface acidity (including both Brønsted and Lewis acidity) relative to the blank samples. This increase is believed to be primarily due to Brønsted acidity as the results show that Lewis acidity for all samples is generally lower than that of unmodified TiO_2. The increase in Brønsted acidity means the availability of more acidic protons in composite samples relative to the blank. This availability is due to different effects. For GO-containing samples the hydroxylated surface of GO contains acidic protons. In addition, the formation of Ti-O-C bonds in both G and GO containing samples will increase the availability of more acidic protons on the surface of the nanocomposite samples.

The effect of Lewis acidity is not the same in all samples and it's appeared to be dependent mainly on the formation of Ti-O-C bonds that decrease the number of

available Ti^{+4} cations which resulted in the decrease in Lewis surface acidity. Within a particular set of nanocomposites, i.e., excluding the unmodified TiO_2, the overall surface acidity as well as Lewis acidity either remain constant or decrease with the increase in G or GO contents. This is probably due to possible stacking of structures causing:

1- Limitations in the formation of Ti-O-C bonds hence decrease in both Lewis and Brønsted acidity is expected.

2- Limitations in the availability of hydroxylated surface groups of GO.

This stacking is reflected in the fact that the surface area of the nanocomposite samples not increase with increase in G or GO contents as otherwise be expected (because of the high surface area of G and GO). Also, it is reflected in the porosity of the samples which is not decreasing as would have been expected due to the formation of more Ti-O-C bonds and therefore more cross-linking. The effect of the increase in G or GO contents on the surface area is very limited due to the limitations in Ti-O-C bond formation and hydroxylated surface of GO due to the stacking of G and GO, as concluded above.

-Surface polarizability and polarity

The surface polarizability of TiO_2-G increases as a function of increasing the content of G because of the hydrophobic character of G. On the other hand relatively hydrophilic GO decreases the surface polarizability of the nanocomposite sample, relative to unmodified TiO_2. Despite the clarity of these trends, the experimental methodology of extending the use of perichromic probes for determination of surface polarizability of solid surfaces, has shown limitations and requires further work.

Interpretation of the surface polarity results of the samples is more complex because this property includes specific as well as non-specific surface-dye interactions. Therefore, a larger collection of samples should be examined before a general trend can be pointed out.

6.2. Future work:

Future work may focus on these aspects:

- The use of different solid samples with variable surface properties to construct calibration curves for the perichromic probes on solid surfaces. This allows the use of these calibration curves to extend these techniques to measure surface polarizability in more reliable manner.
- Extend these investigations to different types of metal oxides to measure their surface properties relevant to their applications.
- Use of G and GO with different surface functionalities to investigate the impact on photocatalytic activity.

References

References

[1] V. R. De Mendonça, H. a J. L. Mourão, A. R. Malagutti, and C. Ribeiro, "The role of the relative dye/photocatalyst concentration in TiO_2 assisted photodegradation process," *Photochem. Photobiol.*, vol. 90, no. 1, pp. 66–72, 2014.

[2] H. Tao, X. Liang, Q. Zhang, and C.-T. Chang, "Enhanced photoactivity of graphene/titanium dioxide nanotubes for removal of Acetaminophen," *Appl. Surf. Sci.*, vol. 324, pp. 258–264, 2015.

[3] N. Raghavan, S. Thangavel, and G. Venugopal, "Enhanced photocatalytic degradation of methylene blue by reduced graphene-oxide/titanium dioxide/zinc oxide ternary nanocomposites," *Mater. Sci. Semicond. Process.*, vol. 30, pp. 321–329, 2015.

[4] Y. Gao, X. Pu, D. Zhang, G. Ding, X. Shao, and J. Ma, "Combustion synthesis of graphene oxide–TiO_2 hybrid materials for photodegradation of methyl orange," *Carbon N. Y.*, vol. 50, no. 11, pp. 4093–4101, 2012.

[5] A. Fujishima and K. Honda, "Electrochemical Photolysis of Water at a Semiconductor Electrode," *Nature*, vol. 238, no. 5358, pp. 37–38, Jul. 1972.

[6] D. Liang, C. Cui, H. Hub, Y. Wang, S. Xu, B. Ying, P. Li, B. Lu, and H. Shen, "Hydrothermal synthesis of anatase TiO_2/reduced graphene oxide nanocomposites with enhanced photocatalytic activity," *J. Alloys Compd.*, vol. 582, pp. 236–240, 2014.

[7] H. Wu, J. Fan, E. Liu, X. Hu, Y. Ma, X. Fan, Y. Li, and C. Tang, "Facile hydrothermal synthesis of TiO_2 nanospindles-reduced graphene oxide composite with a enhanced photocatalytic activity," *J. Alloys Compd.*, vol. 623, pp. 298–303, 2015.

[8] H. Wang, X. Yuan, Y. Wu, H. Huang, X. Peng, G. Zeng, H. Zhong, J. Liang, and M. M. Ren, "Graphene-based materials: Fabrication, characterization and application for the decontamination of wastewater and wastegas and hydrogen storage/generation," *Adv. Colloid Interface Sci.*, vol. 195–196, pp. 19–40, 2013.

[9] B. Jiang, C. Tian, Q. Pan, Z. Jiang, J.-Q. Wang, W. Yan, and H. Fu, "Enhanced Photocatalytic Activity and Electron Transfer Mechanisms of Graphene/TiO_2 with Exposed {001} Facets," *J. Phys. Chem. C*, vol. 115, no. 48, pp. 23718–23725, 2011.

[10] Z.-C. Wang and H.-F. Shui, "Effect of PO_4^{3-} and PO_4^{3-}–SO_4^{2-} modification of TiO_2 on its photocatalytic properties," *J. Mol. Catal. A Chem.*, vol. 263, no. 1–2, pp. 20–25, 2007.

[11] H. Zhang, X. Lv, Y. Li, Y. Wang, and J. Li, "P25-graphene composite as a high performance photocatalyst.," *ACS Nano*, vol. 4, no. 1, pp. 380–6, Jan. 2010.

[12] D.-H. Yoo, T. V. Cuong, V. H. Pham, J. S. Chung, N. T. Khoa, E. J. Kim, and S. H. Hahn, "Enhanced photocatalytic activity of graphene oxide decorated on TiO_2 films under UV and visible irradiation," *Curr. Appl. Phys.*, vol. 11, no. 3, pp. 805–808, 2011.

[13] J. Liu, H. Bai, Y. Wang, Z. Liu, X. Zhang, and D. D. Sun, "Self-assembling TiO_2 nanorods on large graphene oxide sheets at a two-phase interface and their anti-recombination in photocatalytic applications," *Adv. Funct. Mater.*, vol. 20, no. 23, pp. 4175–4181, 2010.

[14] R. Leary and A. Westwood, "Carbonaceous nanomaterials for the enhancement of TiO_2 photocatalysis," *Carbon N. Y.*, vol. 49, no. 3, pp. 741–772, 2011.

[15] M. M. Mohamed and M. M. Al-Esaimi, "Characterization, adsorption and photocatalytic activity of vanadium-doped TiO_2 and sulfated TiO_2 (rutile) catalysts: Degradation of methylene blue dye," *J. Mol. Catal. A Chem.*, vol. 255, no. 1–2, pp. 53–61, 2006.

[16] O. A. El Seoud, A. R. Ramadan, B. M. Sato, and P. A. R. Pires, "Surface properties of calcinated titanium dioxide probed by solvatochromic indicators: Relevance to catalytic applications," *J. Phys. Chem. C*, vol. 114, no. 23, pp. 10436–10443, 2010.

[17] K. Cheetham, *The Chemistry of Nanomaterials: Synthesis, Properties and Applications*. WILEY-VCH Verlag GmbH & Co. KGaA, Weinheim, 2004.

[18] X. Chen and S. S. Mao, "Titanium dioxide nanomaterials: Synthesis, properties, modifications and applications," *Chem. Rev.*, vol. 107, no. 7, pp. 2891–2959, 2007.

[19] Z. Guo and L. Tan, *Fundamentals and Applications of Nanomaterials*. 2009.

[20] K. Byrappa and M. Yoshimura, *Handbook of Hydrothermal Technology A Technology for Crystal Growth and Materials Processing*. 2001.

[21] M. S. A. Sher Shah, A. R. Park, K. Zhang, J. H. Park, and P. J. Yoo, "Green synthesis of biphasic TiO_2-reduced graphene oxide nanocomposites with highly enhanced photocatalytic activity.," *ACS Appl. Mater. Interfaces*, vol. 4, no. 8, pp. 3893–901, 2012.

[22] S. D. Perera, R. G. Mariano, K. Vu, N. Nour, O. Seitz, Y. Chabal, and K. J. Balkus, "Hydrothermal Synthesis of Graphene-TiO_2 Nanotube Composites with Enhanced Photocatalytic Activity," *ACS Catal.*, vol. 2, pp. 949–956, 2012.

[23] X. Bai, X. Zhang, Z. Hua, W. Ma, Z. Dai, X. Huang, and H. Gu, "Uniformly distributed anatase TiO_2 nanoparticles on graphene: Synthesis, characterization, and photocatalytic application," *J. Alloys Compd.*, vol. 599, pp. 10–18, 2014.

[24] J.-W. Shi, H.-Y. Ai, J.-W. Chen, H.-J. Cui, and M.-L. Fu, "The composite of nitrogen-doped anatase titania plates with exposed {001} facets/graphene nanosheets for enhanced visible-light photocatalytic activity," *J. Colloid Interface Sci.*, vol. 430, pp. 100–107, 2014.

[25] Y. Gu, M. Xing, and J. Zhang, "Synthesis and photocatalytic activity of graphene based doped TiO_2 nanocomposites," *Appl. Surf. Sci.*, vol. 319, pp. 2–9, 2014.

[26] J. S. Lee, K. H. You, and C. B. Park, "Highly photoactive, low bandgap TiO_2 nanoparticles wrapped by graphene," *Adv. Mater.*, vol. 24, pp. 1084–1088, 2012.

[27] Y. Ni, W. Wang, W. Huang, C. Lu, and Z. Xu, "Graphene strongly wrapped TiO_2 for high-reactive photocatalyst: A new sight for significant application of graphene," *J. Colloid Interface Sci.*, vol. 428, pp. 162–169, 2014.

[28] S. Linley, Y. Liu, C. J. Ptacek, D. W. Blowes, and F. X. Gu, "Recyclable graphene oxide-supported titanium dioxide photocatalysts with tunable properties.," *ACS Appl. Mater. Interfaces*, vol. 6, pp. 4658–68, 2014.

[29] S. N. Ariffin, H. N. Lim, F. A. Jumeri, M. Zobir, a. H. Abdullah, M. Ahmad, N. a. Ibrahim, N. M. Huang, P. S. Teo, K. Muthoosamy, and I. Harrison, "Modification of polypropylene filter with metal oxide and reduced graphene oxide for water treatment," *Ceram. Int.*, vol. 40, pp. 6927–6936, 2014.

[30] P. T. N. Nguyen, C. Salim, W. Kurniawan, and H. Hinode, "A non-hydrolytic sol–gel synthesis of reduced graphene oxide/TiO_2 microsphere photocatalysts," *Catal. Today*, vol. 230, pp. 166–173, 2014.

[31] Z. Zhang, F. Xiao, Y. Guo, S. Wang, and Y. Liu, "One-pot self-assembled three-dimensional TiO_2-graphene hydrogel with improved adsorption capacities and photocatalytic and electrochemical activities," *ACS Appl. Mater. Interfaces*, vol. 5, pp. 2227–2233, 2013.

[32] J. Li, S. L. Zhou, G. B. Hong, and C. T. Chang, "Hydrothermal preparation of P25-graphene composite with enhanced adsorption and photocatalytic degradation of dyes," *Chem. Eng. J.*, vol. 219, pp. 486–491, 2013.

[33] X. Pan, Y. Zhao, S. Liu, C. L. Korzeniewski, S. Wang, and Z. Fan, "Comparing Graphene-TiO_2 Nanowire and Graphene-TiO_2 Nanoparticle Composite Photocatalysts," *ACS Appl. Mater. Interfaces*, vol. 4, no. 8, pp. 3944–3950, Aug. 2012.

[34] C. Wang, M. Cao, P. Wang, Y. Ao, J. Hou, and J. Qian, "Preparation of graphene-carbon nanotube-TiO_2 composites with enhanced photocatalytic activity for the removal of dye and Cr (VI)," *Appl. Catal. A Gen.*, vol. 473, pp. 83–89, 2014.

[35] W. Qian, P. A. Greaney, S. Fowler, S. Chiu, A. M. Goforth, and J. Jiao, "Low-Temperature Nitrogen Doping in Ammonia Solution for Production of N-Doped TiO_2 - Hybridized Graphene as a Highly Efficient Photocatalyst for Water Treatment," *ACS Sustain. Chem. Eng.*, vol. 2, no. 7, pp. 1802–1810, 2014.

[36] K. Li, J. Xiong, T. Chen, L. Yan, Y. Dai, D. Song, Y. Lv, and Z. Zeng, "Preparation of graphene/TiO_2 composites by nonionic surfactant strategy and their simulated sunlight and visible light photocatalytic activity towards representative aqueous POPs degradation," *J. Hazard. Mater.*, vol. 250–251, pp. 19–28, 2013.

[37] Q. Huang, S. Tian, D. Zeng, X. Wang, W. Song, Y. Li, W. Xiao, and C. Xie, "Enhanced Photocatalytic Activity of Chemically Bonded TiO_2/Graphene Composites Based on the Effective Interfacial Charge Transfer through the C−Ti Bond," *ACS Catal.*, vol. 3, pp. 1477–1485, 2013.

[38] Y. Min, K. Zhang, W. Zhao, F. Zheng, Y. Chen, and Y. Zhang, "Enhanced chemical interaction between TiO_2 and graphene oxide for photocatalytic decolorization of methylene blue," *Chem. Eng. J.*, vol. 193–194, pp. 203–210, 2012.

[39] D. Cai, P. Lian, X. Zhu, S. Liang, W. Yang, and H. Wang, "High specific capacity of TiO_2-graphene nanocomposite as an anode material for lithium-ion batteries in an enlarged potential window," *Electrochim. Acta*, vol. 74, pp. 65–72, 2012.

[40] L. Gu, J. Wang, H. Cheng, Y. Zhao, L. Liu, and X. Han, "One-step preparation of graphene-supported anatase TiO_2 with exposed {001} facets and mechanism of enhanced photocatalytic properties," *ACS Appl. Mater. Interfaces*, vol. 5, pp. 3085–3093, 2013.

[41] P. Gao, A. Li, D. D. Sun, and W. J. Ng, "Effects of various TiO_2 nanostructures and graphene oxide on photocatalytic activity of TiO_2," *J. Hazard. Mater.*, vol. 279, pp. 96–104, 2014.

[42] J. Liu, L. Liu, H. Bai, Y. Wang, and D. D. Sun, "Gram-scale production of graphene oxide-TiO_2 nanorod composites: Towards high-activity photocatalytic materials," *Appl. Catal. B Environ.*, vol. 106, no. 1–2, pp. 76–82, 2011.

[43] T. D. Nguyen-Phan, V. H. Pham, E. W. Shin, H. D. Pham, S. Kim, J. S. Chung, E. J. Kim, and S. H. Hur, "The role of graphene oxide content on the adsorption-enhanced photocatalysis of titanium dioxide/graphene oxide composites," *Chem. Eng. J.*, vol. 170, no. 1, pp. 226–232, 2011.

[44] R. T. Thomas, P. Abdul Rasheed, and N. Sandhyarani, "Synthesis of nanotitania decorated few-layer graphene for enhanced visible light driven photocatalysis," *J. Colloid Interface Sci.*, vol. 428, pp. 214–221, 2014.

[45] S. Ghasemi, A. Esfandiar, S. Rahman Setayesh, A. Habibi-Yangjeh, A. Iraji Zad, and M. R. Gholami, "Synthesis and characterization of TiO_2-graphene nanocomposites modified with noble metals as a photocatalyst for degradation of pollutants," *Appl. Catal. A Gen.*, vol. 462–463, pp. 82–90, 2013.

[46] H. Il Kim, G. H. Moon, D. Monllor-Satoca, Y. Park, and W. Choi, "Solar photoconversion using graphene/TiO_2 composites: Nanographene shell on TiO_2 core versus TiO_2 nanoparticles on graphene sheet," *J. Phys. Chem. C*, vol. 116, pp. 1535–1543, 2012.

[47] N. J. Bell, Y. H. Ng, A. Du, H. Coster, S. C. Smith, and R. Amal, "Understanding the Enhancement in Photoelectrochemical Properties of Photocatalytically Prepared TiO_2 -Reduced Graphene Oxide Composite," *J. Phys. Chem. C*, vol. 115, pp. 6004–6009, 2011.

[48] S. Morales-Torres, L. M. Pastrana-Martínez, J. L. Figueiredo, J. L. Faria, and A. M. T. Silva, "Graphene oxide-P25 photocatalysts for degradation of diphenhydramine pharmaceutical and methyl orange dye," *Appl. Surf. Sci.*, vol. 275, pp. 361–368, 2013.

[49] V. Stengl, S. Bakardjieva, T. M. Grygar, J. Bludská, and M. Kormunda, "TiO_2-graphene oxide nanocomposite as advanced photocatalytic materials.," *Chem. Cent. J.*, vol. 7, pp. 41–52, 2013.

[50] S. S. Liu, H. Sun, S. S. Liu, and S. Wang, "Graphene facilitated visible light photodegradation of methylene blue over titanium dioxide photocatalysts," *Chem. Eng. J.*, vol. 214, pp. 298–303, 2013.

[51] C. Y. Park, U. Kefayat, N. Vikram, T. Ghosh, W. C. Oh, and K. Y. Cho, "Preparation of novel CdS-graphene / TiO_2 composites with high photocatalytic activity for methylene blue dye under visible light," *Bull. Mater. Sci.*, vol. 36, no. 5, pp. 869–876, 2013.

[52] L. M. Pastrana-Martínez, S. Morales-Torres, V. Likodimos, J. L. Figueiredo, J. L. Faria, P. Falaras, and A. M. T. Silva, "Advanced nanostructured photocatalysts based on reduced graphene oxide-TiO_2 composites for degradation of diphenhydramine pharmaceutical and methyl orange dye," *Appl. Catal. B Environ.*, vol. 123–124, pp. 241–256, 2012.

[53] L. M. Pastrana-Martínez, S. Morales-Torres, A. G. Kontos, N. G. Moustakas, J. L. Faria, J. M. Doña-Rodríguez, P. Falaras, and A. M. T. Silva, "TiO_2, surface modified TiO_2 and graphene oxide-TiO_2 photocatalysts for degradation of water pollutants under near-UV/Vis and visible light," *Chem. Eng. J.*, vol. 224, pp. 17–23, 2013.

[54] G. Jiang, Z. Lin, C. Chen, L. Zhu, Q. Chang, N. Wang, W. Wei, and H. Tang, "TiO_2 nanoparticles assembled on graphene oxide nanosheets with high photocatalytic activity for removal of pollutants," *Carbon N. Y.*, vol. 49, no. 8, pp. 2693–2701, 2011.

[55] C. P. Athanasekou, S. Morales-Torres, V. Likodimos, G. E. Romanos, L. M. Pastrana-Martinez, P. Falaras, J. L. Faria, J. L. Figueiredo, and A. M. T. Silva, "Prototype composite membranes of partially reduced graphene oxide/TiO_2 for photocatalytic ultrafiltration water treatment under visible light," *Appl. Catal. B Environ.*, vol. 158–159, pp. 361–372, 2014.

[56] C. Xu, Y. Xu, and J. Zhu, "Photocatalytic Antifouling Graphene Oxide-Mediated Hierarchical Filtration Membranes with Potential Applications on Water Purification," *ACS Appl. Mater. Interfaces*, vol. 6, pp. 16117–16123, 2014.

[57] H. Qin, Y. Xu, J. Kim, T. Hwang, and T. Kim, "The effect of structure on the photoactivity of a graphene/TiO_2 composite," *Mater. Sci. Eng. B Solid-State Mater. Adv. Technol.*, vol. 184, pp. 72–79, 2014.

[58] M. Wojtoniszak, D. Dolat, A. Morawski, and E. Mijowska, "Carbon-modified TiO_2 for photocatalysis," *Nanoscale Res. Lett.*, vol. 7, p. 235, 2012.

[59] Y. Gao, M. Hu, and B. Mi, "Membrane surface modification with TiO_2-graphene oxide for enhanced photocatalytic performance," *J. Memb. Sci.*, vol. 455, pp. 349–356, 2014.

[60] Y. Yang, E. Liu, J. Fan, X. Hu, W. Hou, F. Wu, and Y. Ma, "Green and facile microwave-assisted synthesis of TiO_2/graphene nanocomposite and their photocatalytic activity for methylene blue degradation," *Russ. J. Phys. Chem. A*, vol. 88, no. 3, pp. 478–483, 2014.

[61] S. Anandan, T. Narasinga Rao, M. Sathish, D. Rangappa, I. Honma, and M. Miyauchi, "Superhydrophilic graphene-loaded TiO_2 thin film for self-cleaning applications," *ACS Appl. Mater. Interfaces*, vol. 5, pp. 207–212, 2013.

[62] Z. Peining, A. S. Nair, P. Shengjie, Y. Shengyuan, and S. Ramakrishna, "Facile fabrication of TiO_2-graphene composite with enhanced photovoltaic and photocatalytic properties by electrospinning," *ACS Appl. Mater. Interfaces*, vol. 4, pp. 581–585, 2012.

[63] K. Ichimura, A. Funabiki, and K. Aoki, “Solid-state Solvatochromic Behavior of Reichardt’s Dye Crystals Hybridized with Silica Nanoparticles,” *Chemistry Letters*, vol. 39, no. 6. pp. 586–587, 2010.

[64] S. Spange, S. Prause, E. Vilsmeier, and W. R. Thiel, “Probing surface basicity of solid acids with an aminobenzodifurandione dye as the solvatochromic probe,” *J. Phys. Chem. B*, vol. 109, no. 15, pp. 7280–7289, 2005.

[65] S. Spange, E. Vilsmeier, and Y. Zimmermann, “Probing the Surface Polarity of Various Silicas and Other Moderately Strong Solid Acids by Means of Different Genuine Solvatochromic Dyes,” *Chart*, pp. 6417–6428, 2000.

[66] S. Spange, E. Vilsmeier, K. Fischer, A. Reuter, S. Prause, Y. Zimmermann, and C. Schmidt, “Empirical polarity parameters for various macromolecular and related materials,” *Macromol. Rapid Commun.*, vol. 21, no. 10, pp. 643–659, Jun. 2000.

[67] S. Spange, A. Reuter, S. Prause, and C. Bellmann, “Electrokinetic and solvatochromic studies of functionalized silica particles,” *J. Adhes. Sci. Technol.*, vol. 14, no. 3, pp. 399–414, 2000.

[68] S. Spange, A. Reuter, and E. Vilsmeier, “On the determination of polarity parameters of silica by means of solvatochromic probe dyes,” *Colloid Polym. Sci.*, vol. 274, no. 1, pp. 59–69, 1996.

[69] S. Spange, D. Kunzmann, R. Sens, I. Roth, A. Seifert, and W. R. Thiel, “Solvatochromic azamethine dyes for probing the polarity of gold-cluster-functionalized silica particles,” *Chem. - A Eur. J.*, vol. 9, no. 17, pp. 4161–4167, 2003.

[70] Y. K. Ryu, J. K. Park, H. J. Lim, and J. H. Park, “Solvatochromic characterization of Silica-based stationary phases for liquid chromatography,” *Chromatographia*, vol. 51, no. 9–10, pp. 567–576, 2000.

[71] R. Lungwitz and S. Spange, “Structure and polarity of the phase boundary of n-methylimidazolium chloride/silica,” *J. Phys. Chem. C*, vol. 112, no. 49, pp. 19443–19448, 2008.

[72] S. Prause, S. Spange, and H. Barthel, “Surface polarity of dimethylsiloxane-grafted silica particles,” *Macromol. Chem. Phys.*, vol. 206, no. 3, pp. 364–371, 2005.

[73] Y. Zimmermann and S. Spange, “Solvent Influence on the Catalytic Activity and Surface Polarity of Inorganic Solid Acids,” *J. Phys. Chem. B*, vol. 106, no. 1, pp. 12524–12530, 2002.

[74] S. Prause and S. Spange, “Adsorption of Polymers on Inorganic Solid Acids Investigated by Means of Coadsorbed Solvatochromic Probes,” *J. Phys. Chem. B*, vol. 108, no. 18, pp. 5734–5741, 2004.

[75] I. Kahle and S. Spange, “Internal and external acidity of faujasites as measured by a solvatochromic spiropyran,” *J. Phys. Chem. C*, vol. 114, no. 36, pp. 15448–15453, 2010.

[76] S. Seifert, A. Seifert, G. Brunklaus, K. Hofmann, T. Rüffer, H. Lang, and S. Spange, “Probing the surface polarity of inorganic oxides using merocyanine-type dyes derived from barbituric acid,” *New J. Chem.*, vol. 36, no. 3, p. 674, 2012.

[77] S. Spange, A. Reuter, and D. Lubda, “$E_T(30)$ surface polarity parameters of alkyl- and aryl-group-functionalized silica particles: Differentiating the surface environments by means of the application of differently substituted Reichardt’s dyes,” *Langmuir*, vol. 15, no. 6, pp. 2103–2111, 1999.

[78] I. V. Khristenko, Y. V. Kholin, N. O. Mchedlov-Petrossyan, C. Reichardt, and V. N. Zaitsev, “Probing of chemically modified silica surfaces by solvatochromic pyridinium N-phenolate betaine indicators,” *Colloid J.*, vol. 68, no. 4, pp. 511–517, 2006.

[79] J. Schneider, M. Matsuoka, M. Takeuchi, J. Zhang, Y. Horiuchi, M. Anpo, and D. W. Bahnemann, “Understanding TiO_2 Photocatalysis : Mechanisms and Materials,” *Chem. Rev.*, vol. 114, pp. 9919–9968, 2014.

[80] R. E. Smalley, “Top Ten Problems of Humanity for Next 50 Years,” in *Energy & Nano Technology Conference, Rice University*, 2003.

[81] X. Zhang, B. Zhang, D. Huang, H. Yuan, M. Wang, and Y. Shen, “TiO_2 nanotubes modified with electrochemically reduced graphene oxide for photoelectrochemical water splitting,” *Carbon N. Y.*, vol. 80, pp. 591–598, 2014.

[82] Y. T. Liang, B. K. Vijayan, K. A. Gray, and M. C. Hersam, “Minimizing graphene defects enhances titania nanocomposite-based photocatalytic reduction of CO_2 for improved solar fuel production,” *Nano Lett.*, vol. 11, pp. 2865–2870, 2011.

[83] L. Chen, C. Hsu, P. Chan, X. Zhang, and C. Huang, “Improving the performance of dye-sensitized solar cells with TiO_2/graphene/TiO_2 sandwich structure,” *Nanoscale Res. Lett.*, vol. 9, no. 380, pp. 1–7, 2014.

[84] W. Li, F. Wang, Y. Liu, J. Wang, J. Yang, L. Zhang, A. a. Elzatahry, D. M. Aldhayan, Y. Xia, D. Zhao, D. Al-Dahyan, Y. Xia, and D. Zhao, “General Strategy to Synthesize Uniform Mesoporous TiO_2/Graphene/Mesoporous TiO_2 Sandwich-Like Nanosheets for Highly Reversible Lithium Storage,” *Nano Lett.*, vol. 15, no. 3, pp. 2186–2193, Mar. 2015.

[85] J. Qiu, P. Zhang, M. Ling, S. Li, P. Liu, H. Zhao, and S. Zhang, "Photocatalytic synthesis of TiO_2 and reduced graphene oxide nanocomposite for lithium ion battery.," *ACS Appl. Mater. Interfaces*, vol. 4, pp. 3636–42, 2012.

[86] D. Dutta, S. K. Hazra, J. Das, C. K. Sarkar, and S. Basu, "Studies on p-TiO_2/n-graphene heterojunction for hydrogen detection," *Sensors Actuators B Chem.*, vol. 212, pp. 84–92, 2015.

[87] H. D. Jang, S. K. Kim, H. Chang, K. M. Roh, J. W. Choi, and J. Huang, "A glucose biosensor based on TiO_2-Graphene composite," *Biosens. Bioelectron.*, vol. 38, no. 1, pp. 184–188, 2012.

[88] H. Xu, S. Ouyang, L. Liu, P. Reunchan, N. Umezawa, and J. Ye, "Recent advances in TiO_2-based photocatalysis," *J. Mater. Chem. A*, vol. 2, no. 32, pp. 12642–12661, 2014.

[89] K. Hashimoto, H. Irie, and A. Fujishima, "Photocatalysis: A Historical Overview and Future Prospects," *Jpn. J. Appl. Phys.*, vol. 44, no. 12, pp. 8269–8285, 2005.

[90] C. F. Goodeve and J. A. Kitchener, "The mechanism of photosensitisation by solids," *Trans. Faraday Soc.*, vol. 34, pp. 902–908, Jan. 1938.

[91] C. Hurtado, S. Azucena, and G. Duarte, "Effect of the synthesis variables of TiO_2 on the photocatalytic activity towards the degradation of water pollutants," *Rev. la Fac. Ing. Univ. Antioquia*, vol. 57, pp. 49–56, 2011.

[92] N. Farhangi, "Nano TiO_2/Graphene Composites for Photovoltaic and Photocatalytic Materials," University of Western Ontario, 2012.

[93] Houas A., "Photocatalytic degradation pathway of methylene blue in water," *Appl. Catal. B Environ.*, vol. 31, no. 2, pp. 145–157, 2001.

[94] S. Chowdhury and R. Balasubramanian, "Graphene/semiconductor nanocomposites (GSNs) for heterogeneous photocatalytic decolorization of wastewaters contaminated with synthetic dyes: A review," *Appl. Catal. B Environ.*, vol. 160–161, no. 1, pp. 307–324, 2014.

[95] "Graphene," *The Royal Swedish Academy of Sciences*, 2010. [Online]. Available: http://www.nobelprize.org/nobel_prizes/physics/laureates/2010/advanced-physicsprize2010.pdf.

[96] K. S. Novoselov, A. K. Geim, S. V Morozov, D. Jiang, Y. Zhang, S. V Dubonos, I. V Grigorieva, and A. A. Firsov, "Electric field effect in atomically thin carbon films.," *Science*, vol. 306, no. 5696, pp. 666–9, Oct. 2004.

[97] V. Singh, D. Joung, L. Zhai, S. Das, S. I. Khondaker, and S. Seal, “Graphene based materials: Past, present and future,” *Prog. Mater. Sci.*, vol. 56, no. 8, pp. 1178–1271, 2011.

[98] A. K. Geim and K. S. Novoselov, “The rise of graphene.,” *Nat. Mater.*, vol. 6, pp. 183–191, 2007.

[99] Y. Zhu, S. Murali, W. Cai, X. Li, J. W. Suk, J. R. Potts, and R. S. Ruoff, “Graphene and graphene oxide: Synthesis, properties, and applications,” *Adv. Mater.*, vol. 22, no. 35, pp. 3906–3924, 2010.

[100] D. R. Dreyer, S. Park, C. W. Bielawski, and R. S. Ruoff, “The chemistry of graphene oxide.,” *Chem. Soc. Rev.*, vol. 39, no. 1, pp. 228–240, 2010.

[101] H. He, J. Klinowski, M. Forster, and A. Lerf, “A new structural model for graphite oxide,” *Chem. Phys. Lett.*, vol. 287, no. 1–2, pp. 53–56, Apr. 1998.

[102] A. Lerf, H. He, M. Forster, and J. Klinowski, “Structure of Graphite Oxide Revisited Ⅱ,” *J. Phys. Chem. B*, vol. 102, no. 23, pp. 4477–4482, Jun. 1998.

[103] D. Chen, H. Feng, and J. Li, “Graphene oxide: Preparation, functionalization, and electrochemical applications,” *Chem. Rev.*, vol. 112, no. 11, pp. 6027–6053, 2012.

[104] Y. Park, W. Kim, H. Park, T. Tachikawa, T. Majima, and W. Choi, “Carbon-doped TiO_2 photocatalyst synthesized without using an external carbon precursor and the visible light activity,” *Appl. Catal. B Environ.*, vol. 91, no. 1–2, pp. 355–361, 2009.

[105] S. Nigam and S. Rutan, “Principles and Applications of Solvatochromism,” *Appl. Spectrosc.*, vol. 55, no. 11, p. 362A–370A, 2001.

[106] C. Reichardt, “Solvatochromic dyes as solvent polarity indicators,” *Chem. Rev.*, vol. 94, pp. 2319–2358, 1994.

[107] L. C. Fidale, T. Heinze, and O. A. El Seoud, “Perichromism: A powerful tool for probing the properties of cellulose and its derivatives,” *Carbohydr. Polym.*, vol. 93, no. 1, pp. 129–134, 2013.

[108] J. Catalan, E. Mena, W. Meutermans, and J. Elguero, “Solvatochromism of a typical merocyanine: stilbazolium betaine and its 2,6-di-tert-butyl derivative,” *J. Phys. Chem.*, vol. 96, no. 9, pp. 3615–3621, 1992.

[109] J. Catalán, P. Pérez, J. Elguero, and W. Meutermans, “Solvatochromism of Sterically Hindered Stilbazolium Betaines and Its Relationship to Reichardt’s $E_T(30)$ Scale: The Problem of the Measurement of the Polarity vs the Acidity of Alcohols,” *Chem. Ber.*, vol. 126, no. 11, pp. 2445–2448, Nov. 1993.

[110] M. A. Kessler and O. S. Wolfbeis, "$E_T(33)$, a solvatochromic polarity and micellar probe for neutral aqueous solutions," *Chem. Phys. Lipids*, vol. 50, no. 1, pp. 51–56, Apr. 1989.

[111] C. Loffredo, P. A. R. Pires, M. Imran, and O. A. El Seoud, "β-Carotene: A green, inexpensive, and convenient solvatochromic probe for the determination of solvent polarizability," *Dye. Pigment.*, vol. 96, no. 1, pp. 16–24, 2013.

[112] J. Catalán and C. Díaz, "A Generalized Solvent Acidity Scale: The Solvatochromism ofo-tert-Butylstilbazolium Betaine Dye and Its Homomorph o,o′-Di-tert-butylstilbazolium Betaine Dye," *Liebigs Ann.*, vol. 1997, no. 9, pp. 1941–1949, Sep. 1997.

[113] "IUPAC. Compendium of Chemical Terminology, 2nd ed. (the 'Gold Book'). Compiled by A. D. McNaught and A. Wilkinson. Blackwell Scientific Publications, Oxford (1997). XML on-line corrected version: http://goldbook.iupac.org (2006-) created by M. Nic, J. Jir." [Online]. Available: http://goldbook.iupac.org/P04710.html. [Accessed: 05-Apr-2015].

[114] L. C. Fidale, P. M. Lima, T. Heinze, and O. A. El Seoud, "Employing perichromism for probing the properties of carboxymethyl cellulose films : an expedient , accurate method for the determination of the degree of substitution of the biopolymer derivative," *Cellulose*, vol. 19, pp. 151–159, 2012.

[115] E. B. Tada, L. P. Novaki, and O. A. El Seoud, "Solvatochromism in pure and binary solvent mixtures : effects of the molecular structure of the zwitterionic probe," *J. Phys. Org. Chem.*, vol. 13, no. 30, pp. 679–687, 2000.

[116] R. Pardo, M. Zayat, and D. Levy, "$E_T(33)$ dye as a tool for polarity determinations: Application to porous hybrid silica thin-films," *J. Photochem. Photobiol. A Chem.*, vol. 210, no. 1, pp. 17–22, 2010.

[117] O. A. El Seoud, P. A. R. Pires, C. Loffredo, M. Imran, P. D. Pulcini, M. F. Corrêa, and R. Mustafa, "Convenient solvatochromic probes for the determination of solvent properties: β-Carotene and 2-chloro-7-nitro-9H-fluorene," *J. Braz. Chem. Soc.*, vol. 24, no. 7, pp. 1079–1084, 2013.

[118] P. A. R. Pires, M. Imran, C. Loffredo, P. M. Donate, D. Previdi, and O. A. El Seoud, "Solvatochromism of 2-(N,N-dimethylamino)-7-nitrofluorene and the natural dye β-carotene: application for the determination of solvent dipolarity and polarizability," *J. Phys. Org. Chem.*, vol. 26, no. 3, pp. 280–285, 2013.

[119] J. Catalán and H. Hopf, "Empirical treatment of the inductive and dispersive components of solute-solvent interactions: The solvent polarizability (SP) scale," *European J. Org. Chem.*, vol. 2004, pp. 4694–4702, 2004.

[120] J. Catalán, “Toward a generalized treatment of the solvent effect based on four empirical scales: Dipolarity (SdP, a new scale), polarizability (SP), acidity (SA), and basicity (SB) of the medium,” *J. Phys. Chem. B*, vol. 113, no. 17, pp. 5951–5960, 2009.

[121] R. J. Cvetanović and Y. Amenomiya, “Application of a Temperature-Programmed Desorption Technique to Catalyst Studies,” *Adv. Catal.*, vol. 17, pp. 103–149, 1967.

[122] M. Niwa, N. Katada, and K. Okumura, “Solid Acidity of Zeolites,” in *Characterization and Design of Zeolite Catalysts SE - 2*, vol. 141, Springer Berlin Heidelberg, 2010, pp. 9–27.

[123] X. S. Zhao and G. Q. Lu, “Nanoporous Materials - an Overview,” *Nanoporous Mater. Sci. Eng.*, vol. Volume 4, pp. 1–13, 2004.

[124] K. S. W. Sing, “Reporting physisorption data for gas/solid systems with special reference to the determination of surface area and porosity (Recommendations 1984),” *Pure Appl. Chem.*, vol. 57, no. 4, Jan. 1985.

[125] “Operating Principles - Surface Analysis Facility.” [Online]. Available: http://saf.chem.ox.ac.uk/operating-principles-3.aspx. [Accessed: 05-Apr-2015].

[126] S. Brunauer, P. H. Emmett, and E. Teller, “Adsorption of Gases in Multimolecular Layers,” *J. Am. Chem. Soc.*, vol. 60, no. 2, pp. 309–319, Feb. 1938.

[127] S. Brunauer, *The Adsorption of Gases and Vapors. Physical Adsorption*, vol. 1. 1943.

[128] D. Harvey, “Spectroscopic Methods,” in *Modern Analytical Chemistry*, McGraw-Hill Companies, 2008, pp. 543–666.

[129] A. Hofmann, “12 Spectroscopic techniques : I Spectrophotometric techniques,” in *Principles and Techniques of Biochemistry and Molecular Biology*, K. Wilson and J. Walker, Eds. 2010, pp. 477–521.

[130] B. Kalantar-zadeh, Kourosh; Fry, “Chapter 5 : Characterization Techniques for Nanomaterials,” in *Nanotechnology-Enabled Sensors*, 2008, pp. 211–281.

[131] V. Džimbeg-malčić, Ž. Barbarić-mikočević, and K. Itrić, “Kubelka-Munk Theory in Describing Optical Properties of Paper (1),” *Tech. Gaz.*, vol. 18, no. 1, pp. 117–124, 2011.

[132] U. P. A. Escobedo Morales, E. Sanchez Mora, A. Morales, E. Mora, and U. Pal, “Use of diffuse reflectance spectroscopy for optical characterization of un-supported nanostructures,” *Rev. Mex. Fis. S*, vol. 53, no. 5, pp. 18–22, 2007.

[133] "How Scanning Electron Microscopes Work - HowStuffWorks." [Online]. Available: http://science.howstuffworks.com/scanning-electron-microscope.htm. [Accessed: 25-Feb-2015].

[134] D. Stokes, "Principles of SEM," in *Principles and Practice of Variable Pressure : Environmental Scanning Electron Microscopy (VP-ESEM).*, Chichester, GBR: :John Wiley & Sons., 2009, pp. 17–62.

[135] "Operating a Scanning Electron Microscope - HowStuffWorks." [Online]. Available: http://science.howstuffworks.com/scanning-electron-microscope4.htm. [Accessed: 25-Feb-2015].

[136] R. F. Egerton, "Operating Principle of the SEM," in *Physical Principles of Electron Microscopy*, 2005, pp. 125–153.

[137] J. Ragai and N. Yacoub, "Synergistic Effect between TiO_2 , Zirconium and Carbon in the Photodegradation of Methyl Orange and Methylene Blue," *Adsorpt. Sci. Technol.*, vol. 31, no. 2/3, pp. 213–221, 2013.

[138] W. Khaodee, B. Jongsomjit, P. Praserthdam, S. Goto, and S. Assabumrungrat, "Impact of temperature ramping rate during calcination on characteristics of nano-ZrO_2 and its catalytic activity for isosynthesis," *J. Mol. Catal. A Chem.*, vol. 280, no. 1–2, pp. 35–42, 2008.

[139] D. F. Siqueira Petri, G. Wenz, P. Schunk, and T. Schimmel, "An Improved Method for the Assembly of Amino-Terminated Monolayers on SiO_2 and the Vapor Deposition of Gold Layers," *Langmuir*, vol. 15, no. 13, pp. 4520–4523, 1999.

[140] J. Catalán and C. Díaz, "Extending the Solvent Acidiy Scale to Highly Acidic Organic Solvents: The Unique Photophysical Behaviour of 3,6-Diethyltetrazine," *European J. Org. Chem.*, vol. 1999, pp. 885–891, 1999.

[141] Y. Harima, T. Fujita, Y. Kano, I. Imae, K. Komaguchi, Y. Ooyama, and J. Ohshita, "Lewis-acid sites of TiO_2 surface for adsorption of organic dye having pyridyl group as anchoring unit," *J. Phys. Chem. C*, vol. 117, pp. 16364–16370, 2013.

[142] L. M. Pastrana-Martínez, S. Morales-Torres, V. Likodimos, P. Falaras, J. L. Figueiredo, J. L. Faria, and A. M. T. Silva, "Role of oxygen functionalities on the synthesis of photocatalytically active graphene-TiO_2 composites," *Appl. Catal. B Environ.*, vol. 158–159, pp. 329–340, 2014.

[143] J. Catalán, H. Hopf, D. Klein, and M. Martus, "On the photophysics of polyenes. 1. Bathochromic shifts in their 1Ag → 1Bu electronic transitions caused by the polarizability of the medium," *J. Phys. Chem. A*, vol. 112, pp. 5653–5657, 2008.

[144] D. Zhao, G. Sheng, C. Chen, and X. Wang, "Enhanced photocatalytic degradation of methylene blue under visible irradiation on graphene@TiO_2 dyade structure," *Appl. Catal. B Environ.*, vol. 111–112, pp. 303–308, 2012.

[145] A. A. Ismail, T. A. Kandiel, and D. W. Bahnemann, "Novel (and better?) titania-based photocatalysts: Brookite nanorods and mesoporous structures," *J. Photochem. Photobiol. A Chem.*, vol. 216, no. 2–3, pp. 183–193, 2010.

[146] N. Murakami, T. A. Kamai, T. Tsubota, and T. Ohno, "Novel hydrothermal preparation of pure brookite-type titanium (IV) oxide nanocrystal under strong acidic conditions," *Catal. Commun.*, vol. 10, no. 6, pp. 963–966, 2009.

[147] X. Huang, L. Wang, J. Zhou, and N. Gao, "Photocatalytic decomposition of bromate ion by the UV/P25-Graphene processes," *Water Res.*, vol. 57, pp. 1–7, 2014.

[148] N. Katada, T. Tsubaki, and M. Niwa, "Measurements of number and strength distribution of Brønsted and Lewis acid sites on sulfated zirconia by ammonia IRMS-TPD method," *Appl. Catal. A Gen.*, vol. 340, pp. 76–86, 2008.

[149] V. Štengl, D. Popelková, and P. Vláčil, "TiO_2-graphene nanocomposite as high performace photocatalysts," *J. Phys. Chem. C*, vol. 115, no. 51, pp. 25209–25218, 2011.

[150] C. Basheer, "Application of titanium dioxide-graphene composite material for photocatalytic degradation of alkylphenols," *J. Chem.*, vol. 2013, pp. 1–10, 2013.

Appendix I

N_2 adsorption isotherms

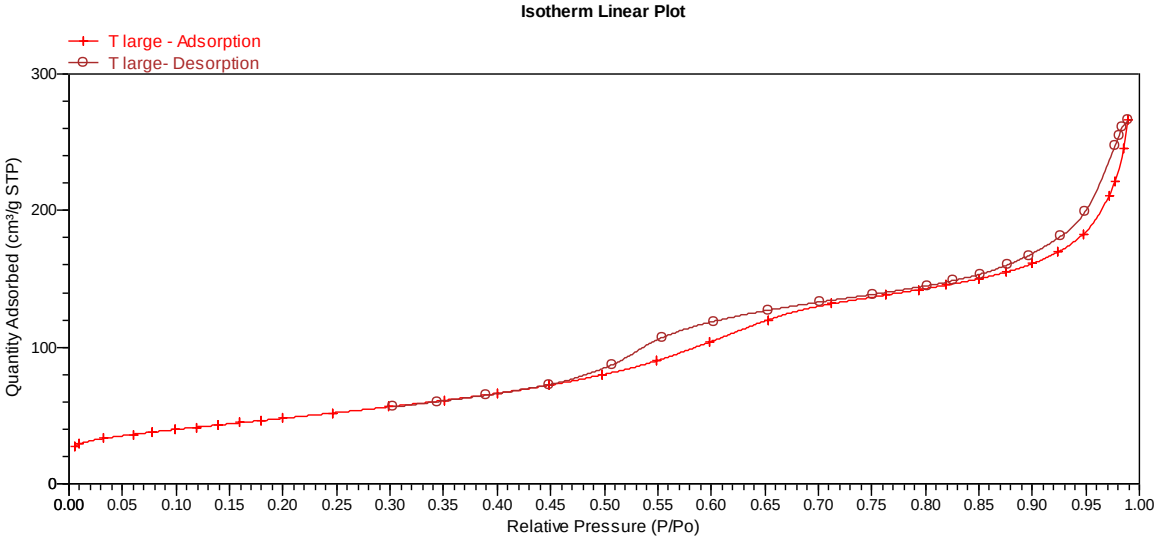

N_2 adsorption isotherm of TL blank sample

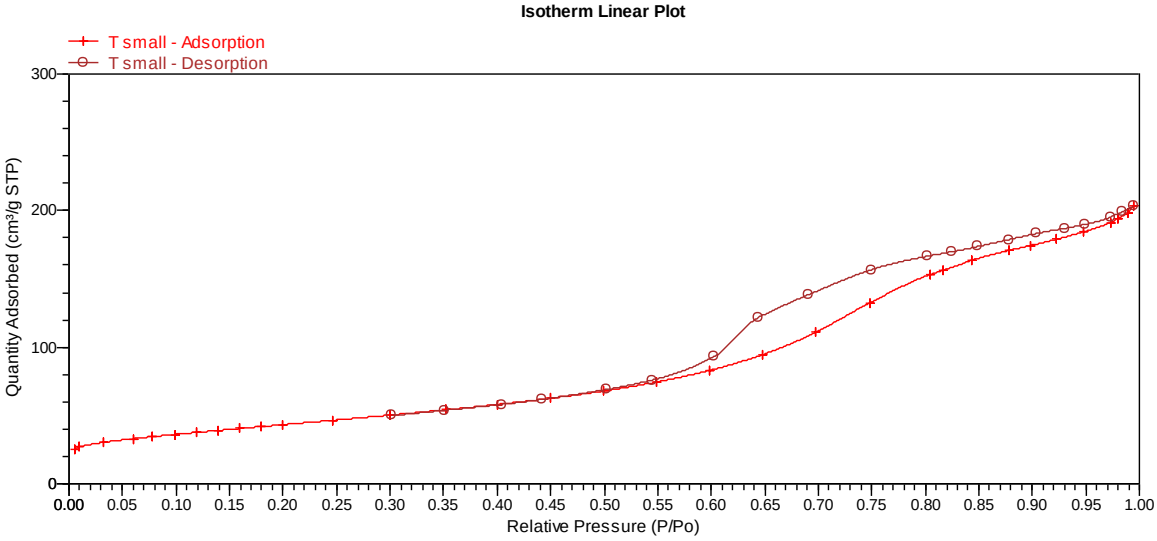

N_2 adsorption isotherm of TS blank sample

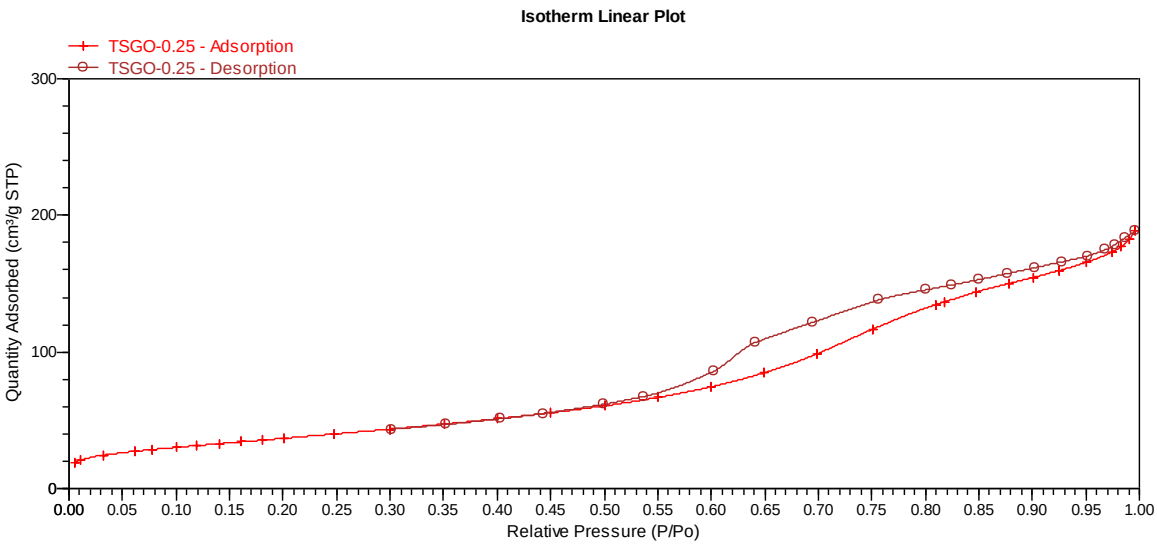

N_2 adsorption isotherm of TS-GO-0.25 sample

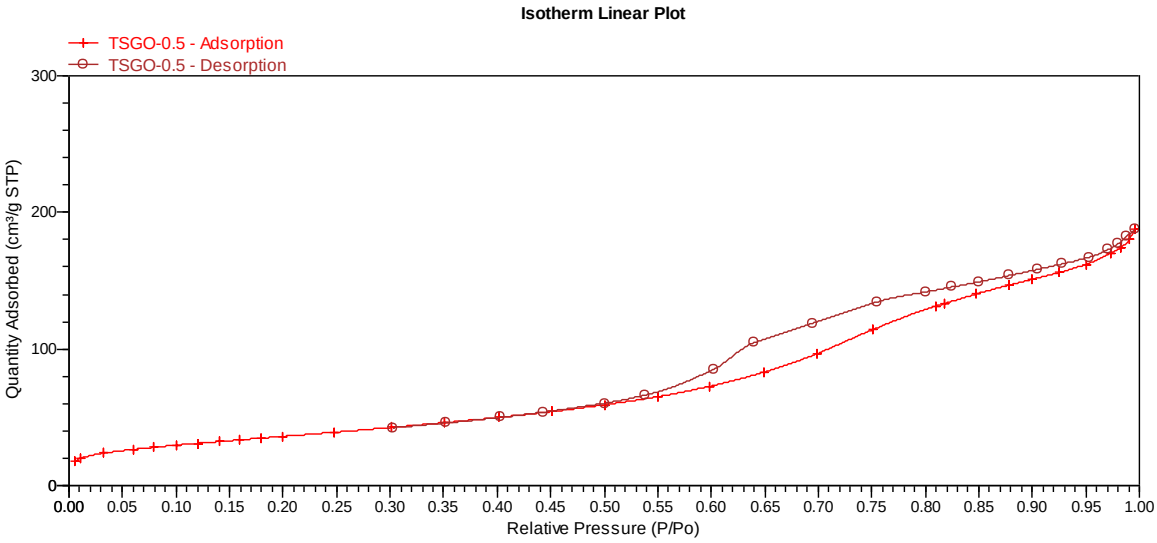

N_2 adsorption isotherm of TS-GO-0.50 sample

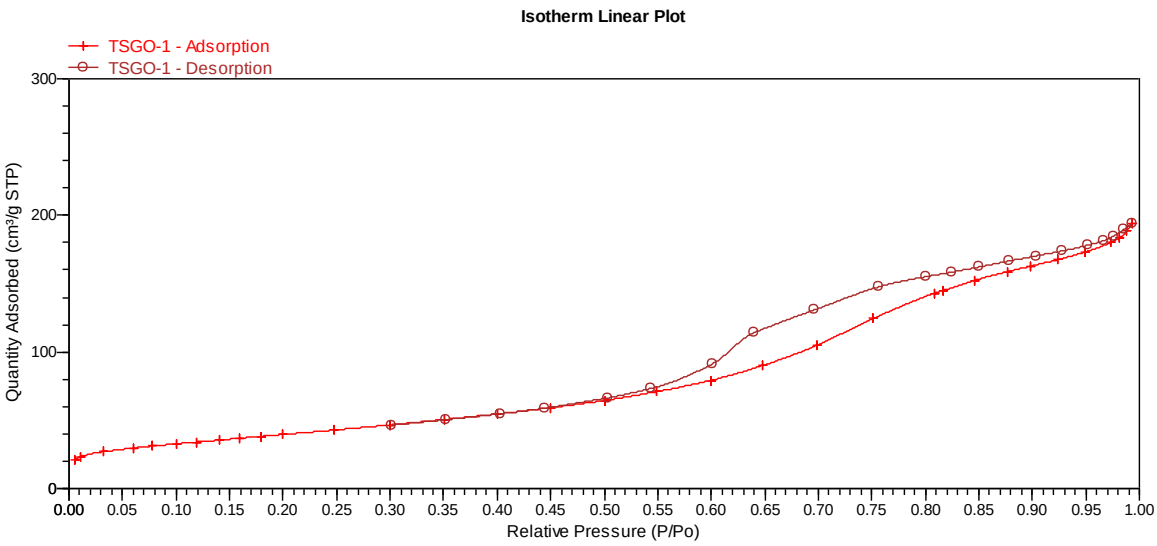

N_2 adsorption isotherm of TS-GO-1.00 sample

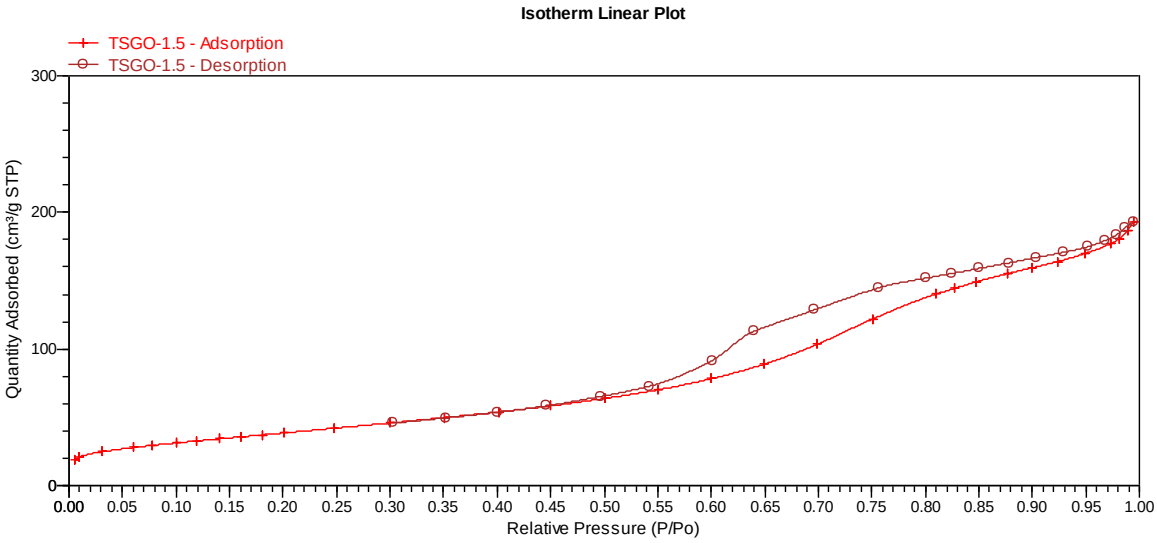

N_2 adsorption isotherm of TS-GO-1.50 sample

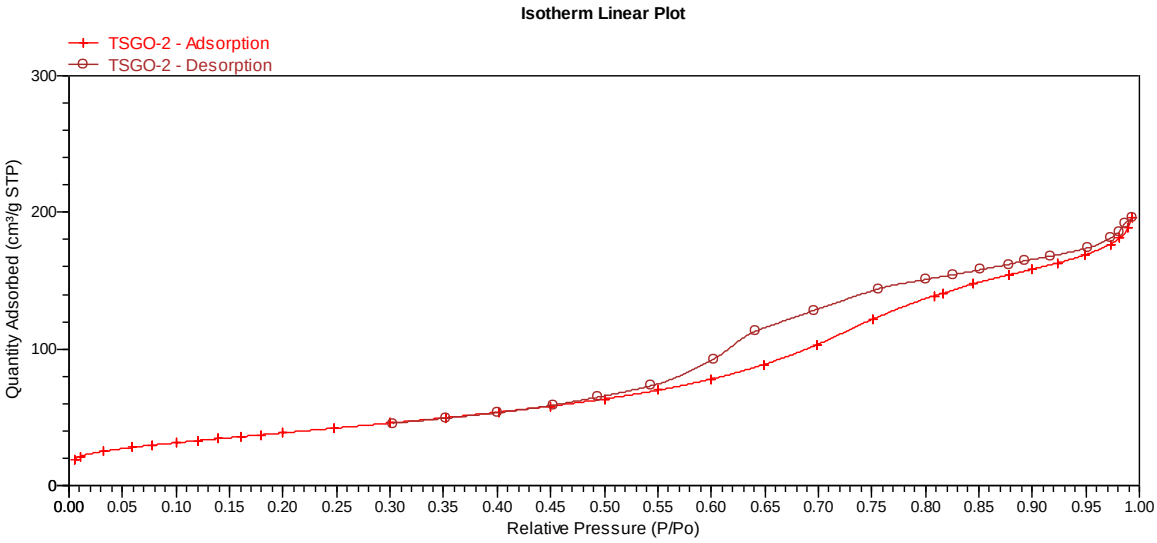

N_2 adsorption isotherm of TS-GO-2.00 sample

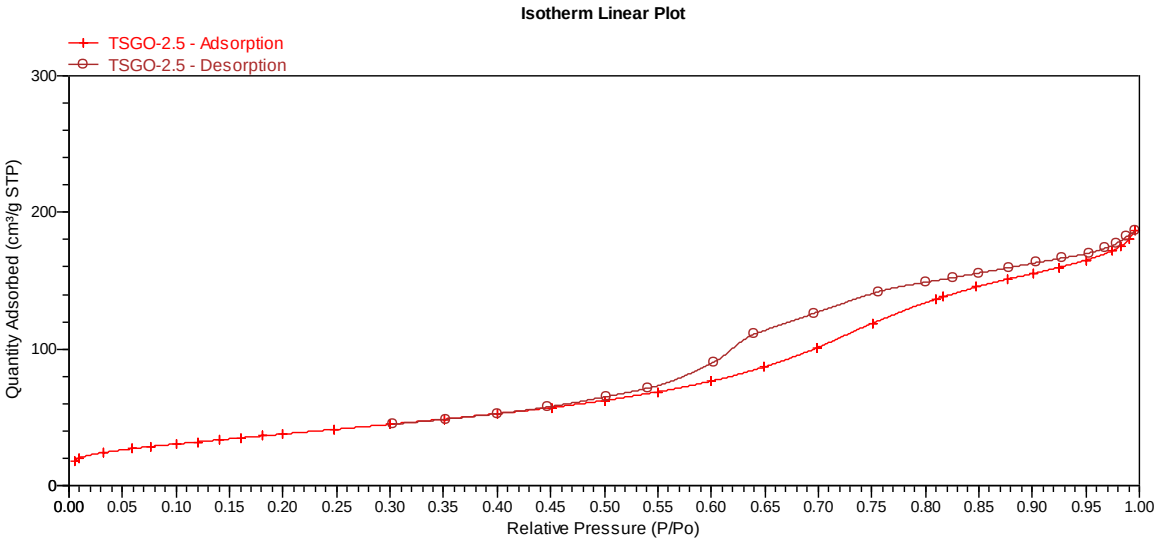

N_2 adsorption isotherm of TS-GO-2.50 sample

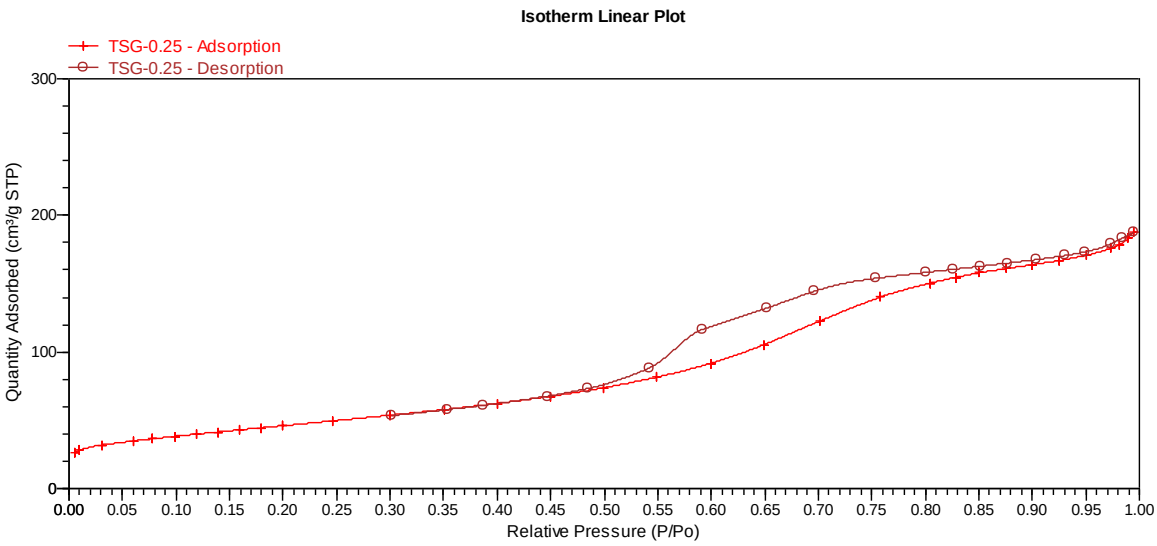

N_2 adsorption isotherm of TS-G-0.25 sample

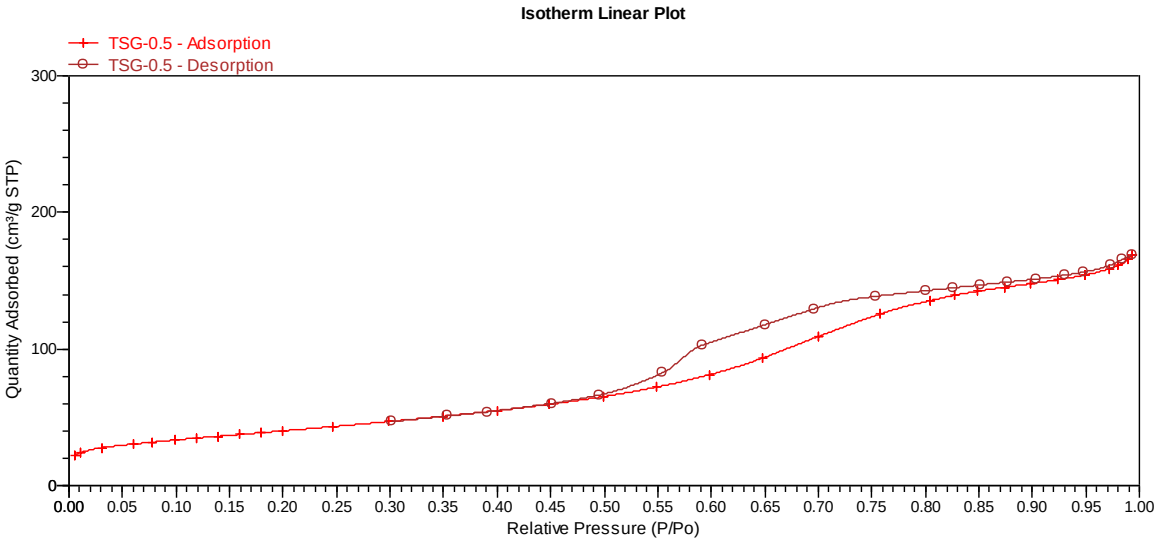

N_2 adsorption isotherm of TS-G-0.50 sample

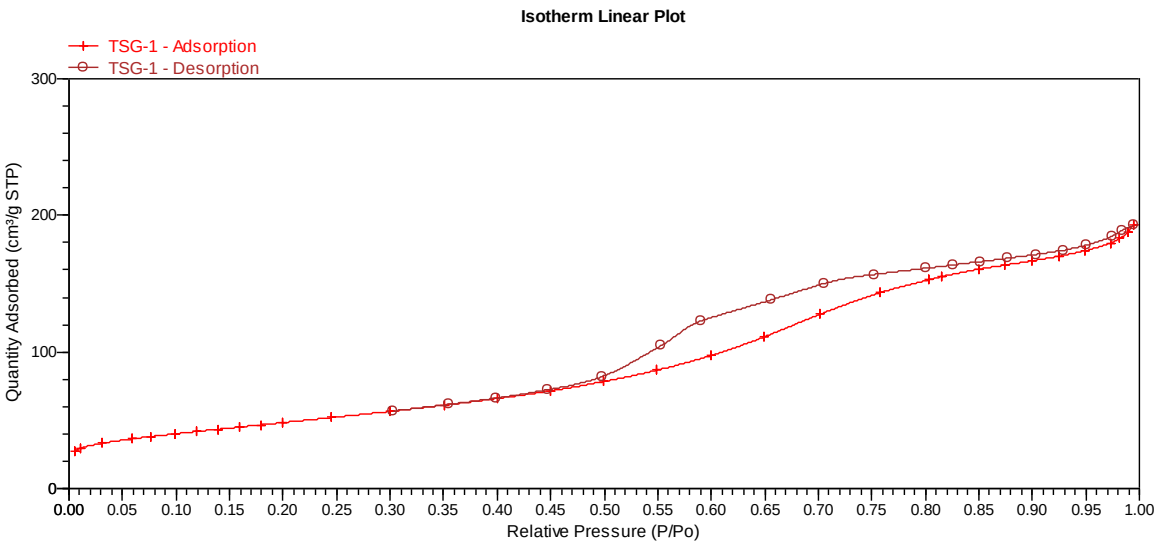

N_2 adsorption isotherm of TS-G-1.00 sample

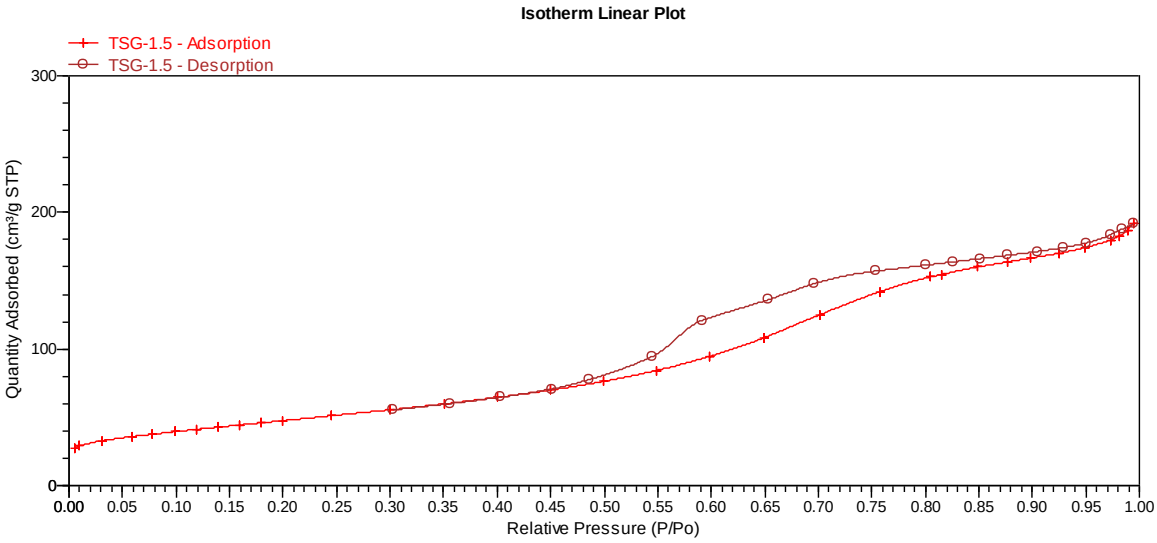

N_2 adsorption isotherm of TS-G-1.50 sample

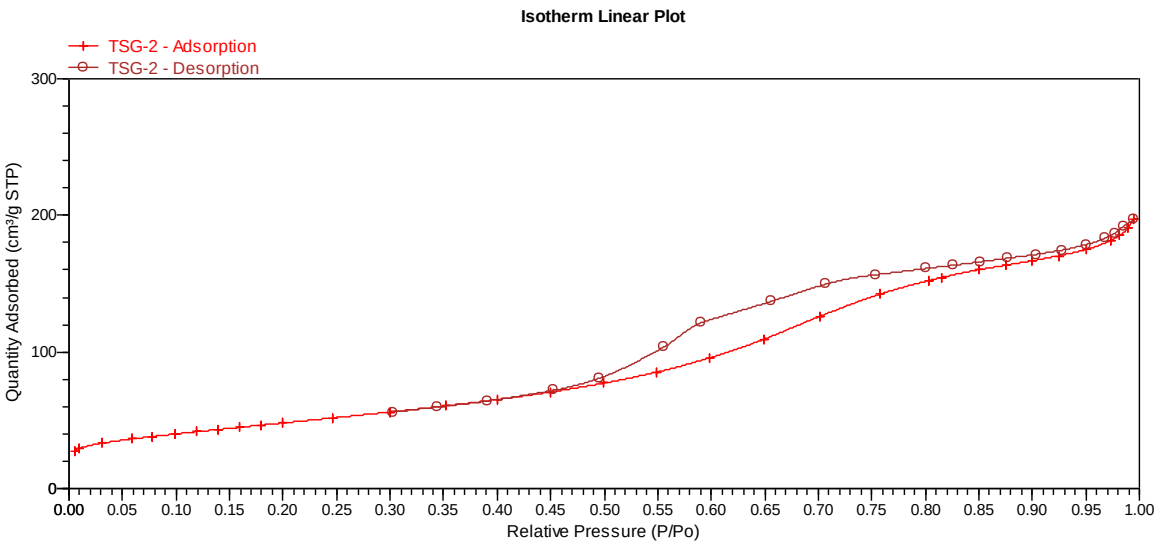

N_2 adsorption isotherm of TS-G-2.00 sample

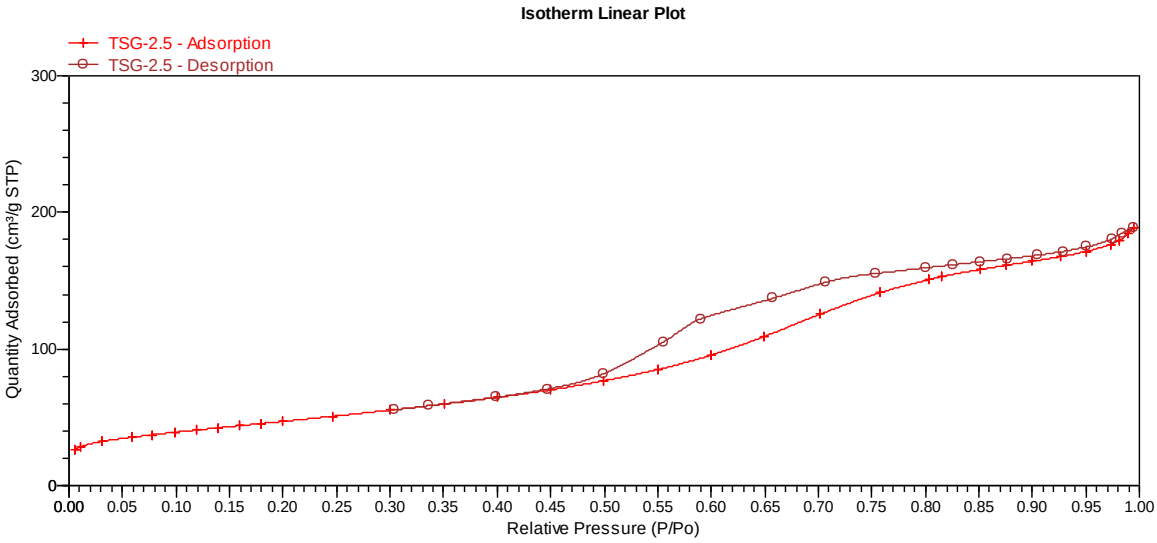

N_2 adsorption isotherm of TS-G-2.50 sample

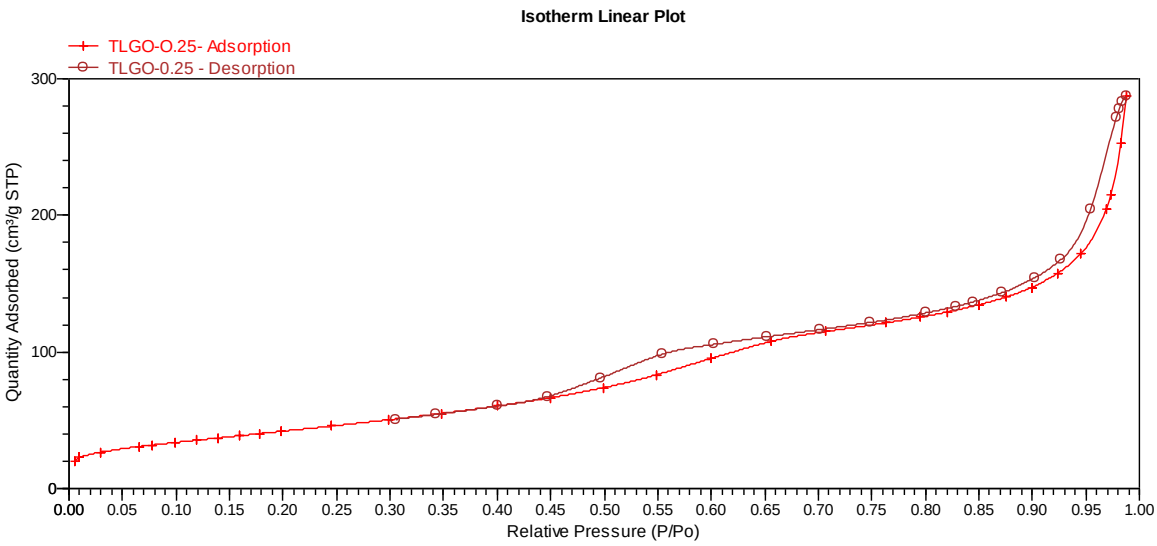

N_2 adsorption isotherm of TL-GO-0.25 sample

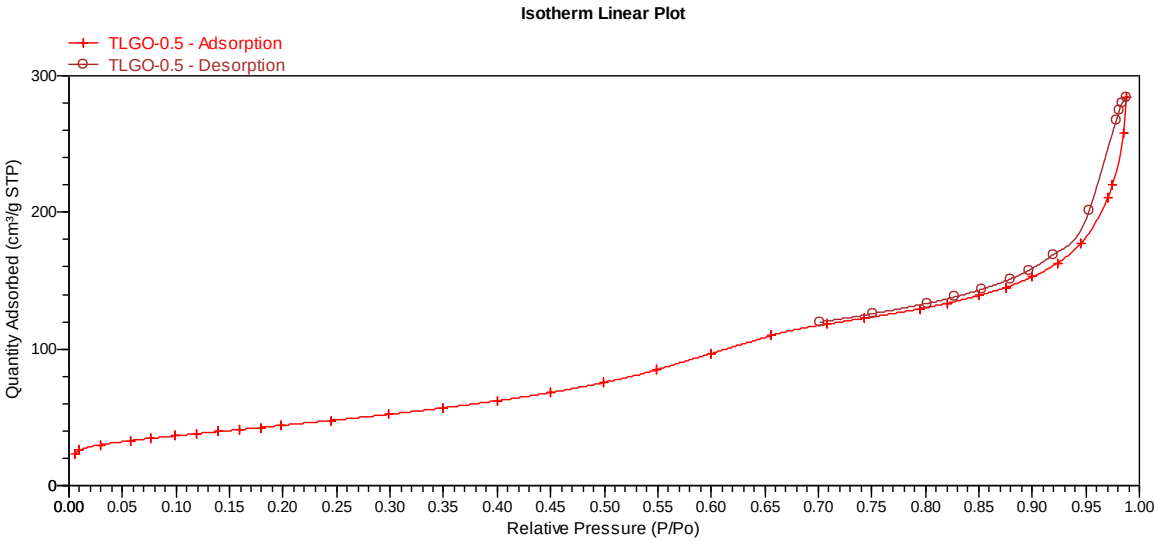

N_2 adsorption isotherm of TL-GO-0.50 sample

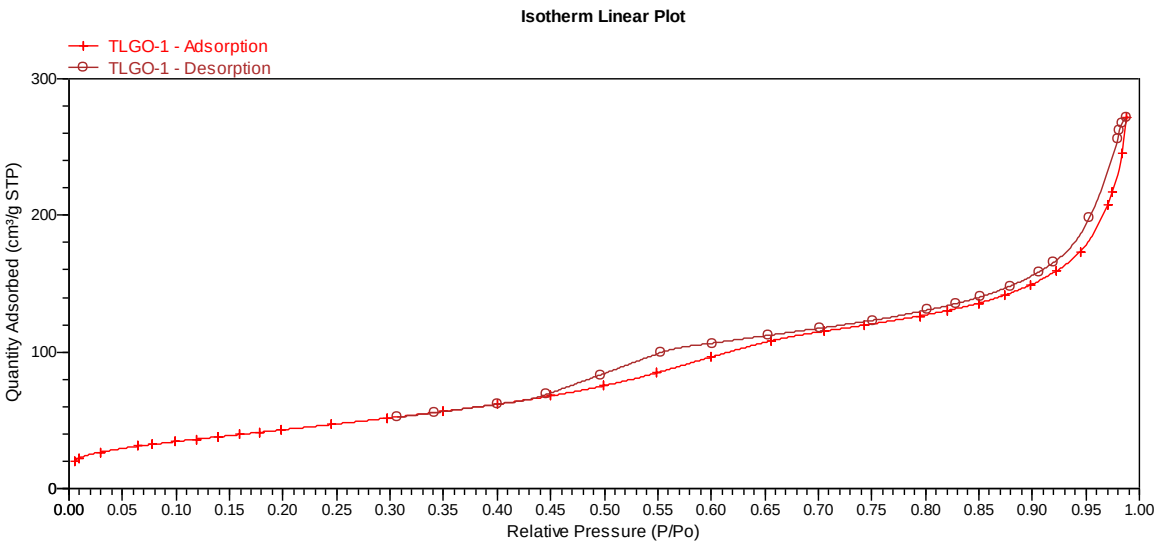

N_2 adsorption isotherm of TL-GO-1.00 sample

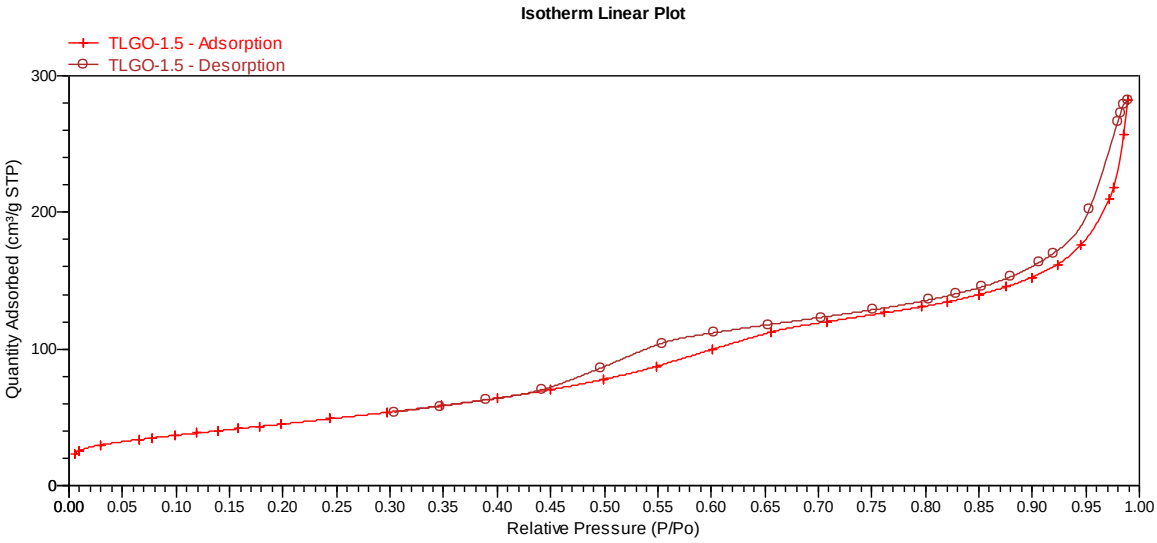

N_2 adsorption isotherm of TL-GO-1.50 sample

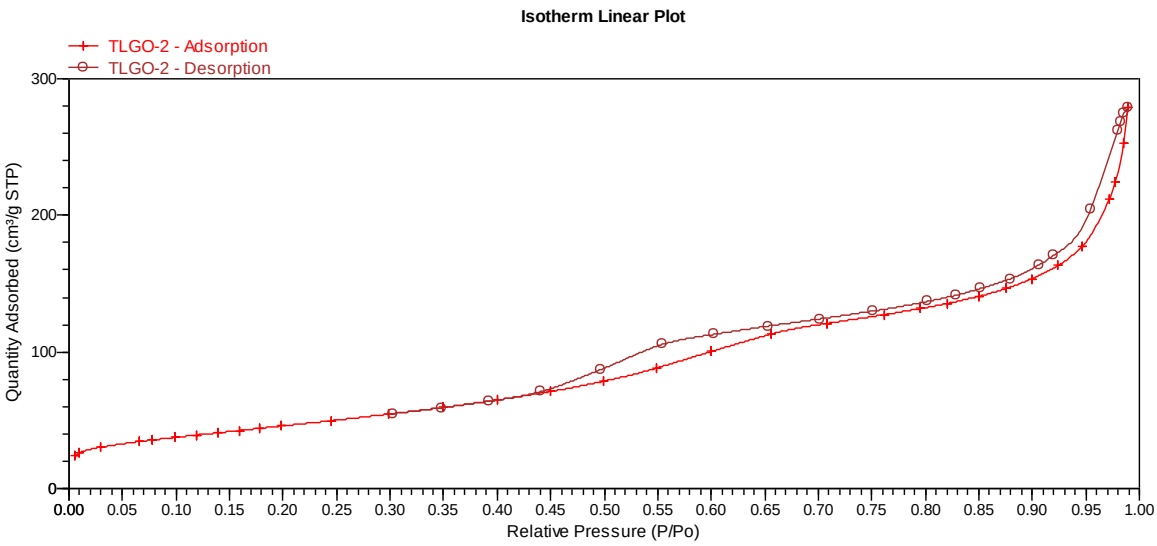

N_2 adsorption isotherm of TL-GO-2.00 sample

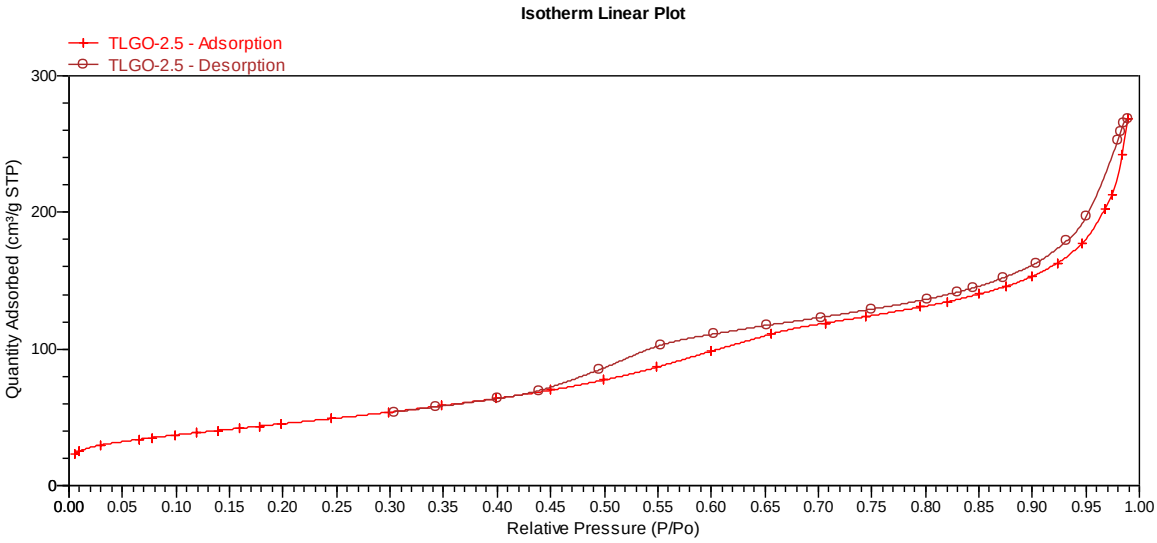

N_2 adsorption isotherm of TL-GO-2.50 sample

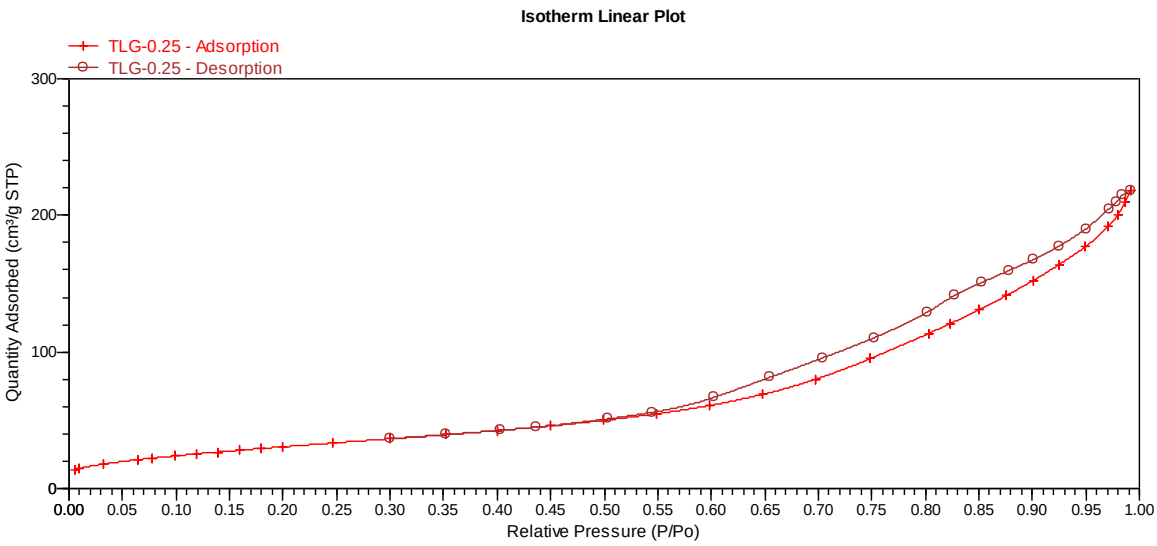

N_2 adsorption isotherm of TL-G-0.25 sample

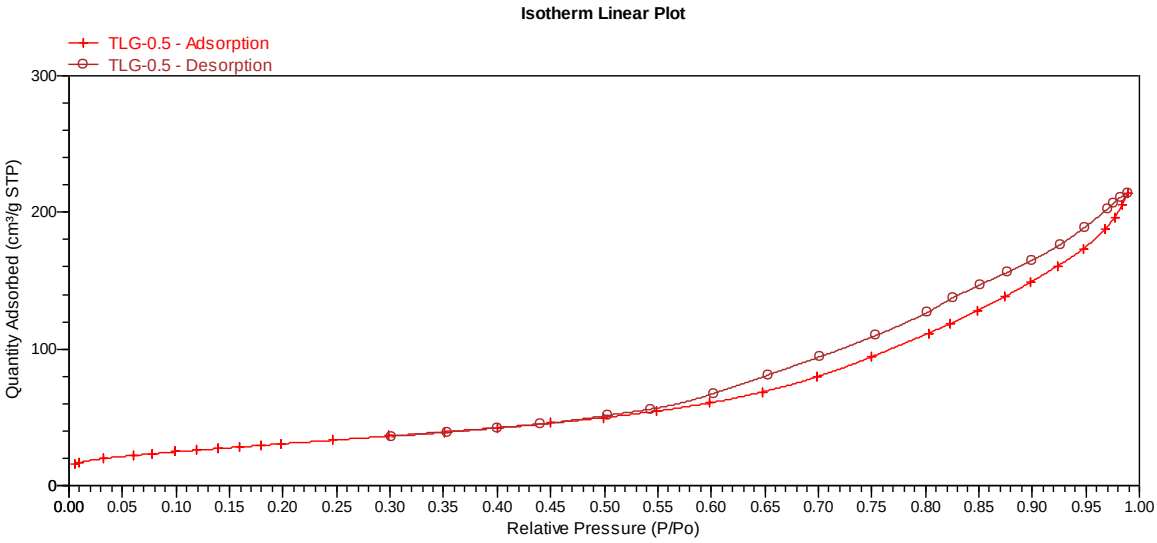

N_2 adsorption isotherm of TL-G-0.50 sample

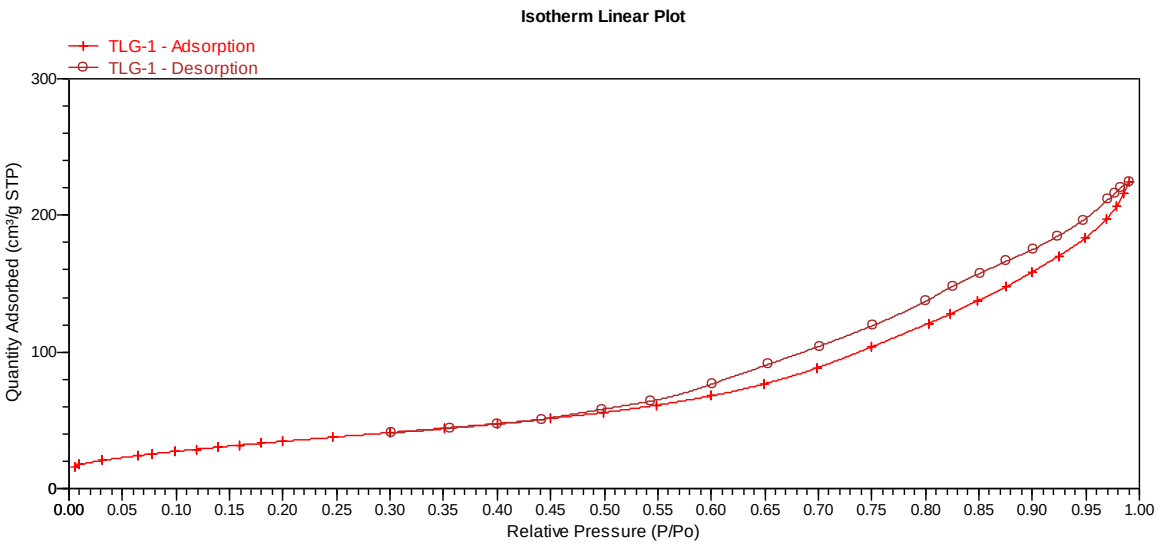

N_2 adsorption isotherm of TL-G-1.00 sample

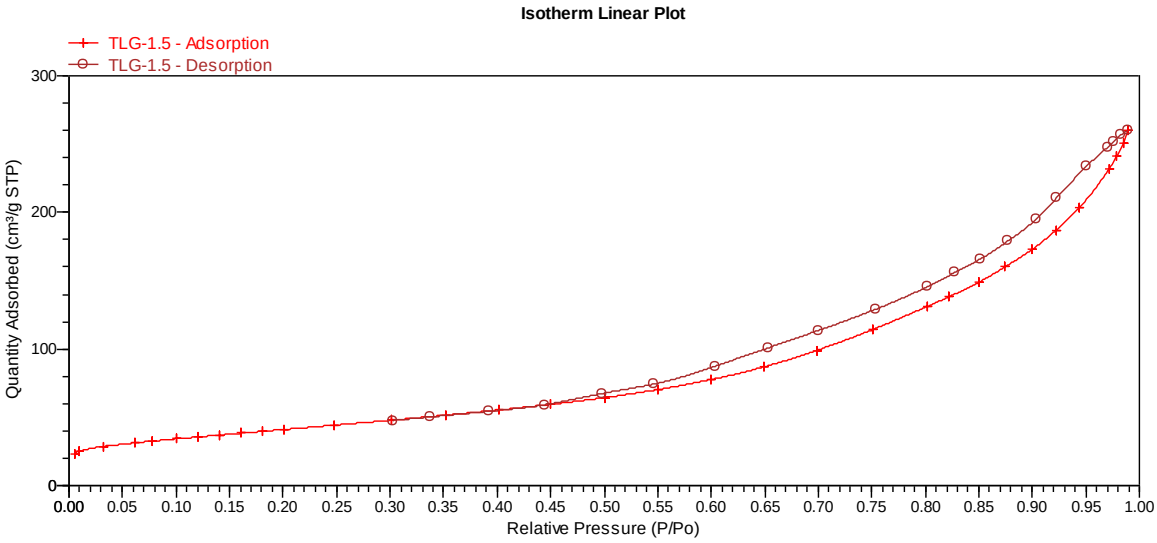

N_2 adsorption isotherm of TL-G-1.50 sample

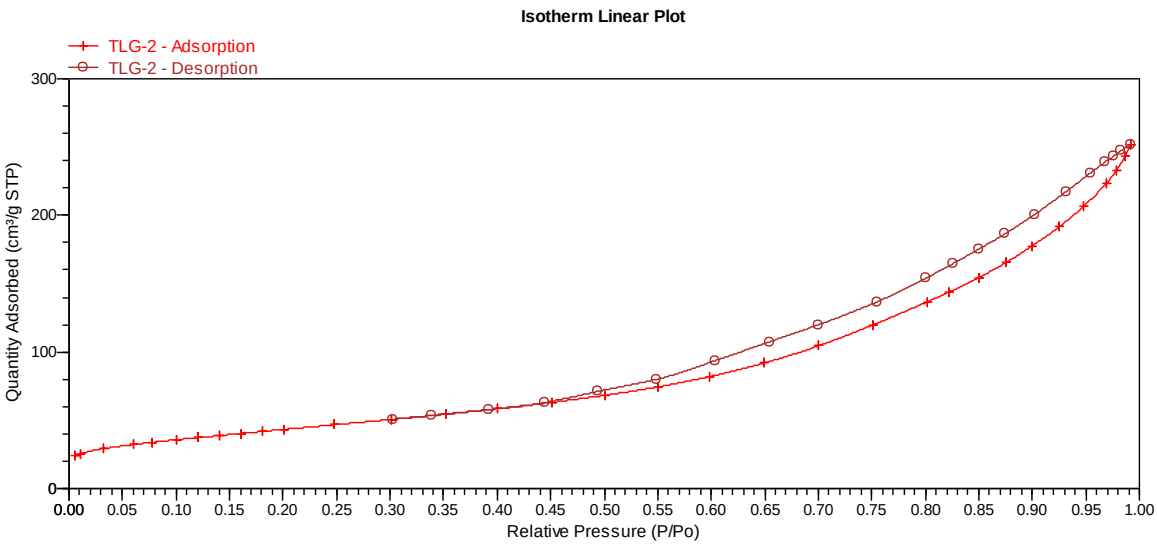

N_2 adsorption isotherm of TL-G-2.00 sample

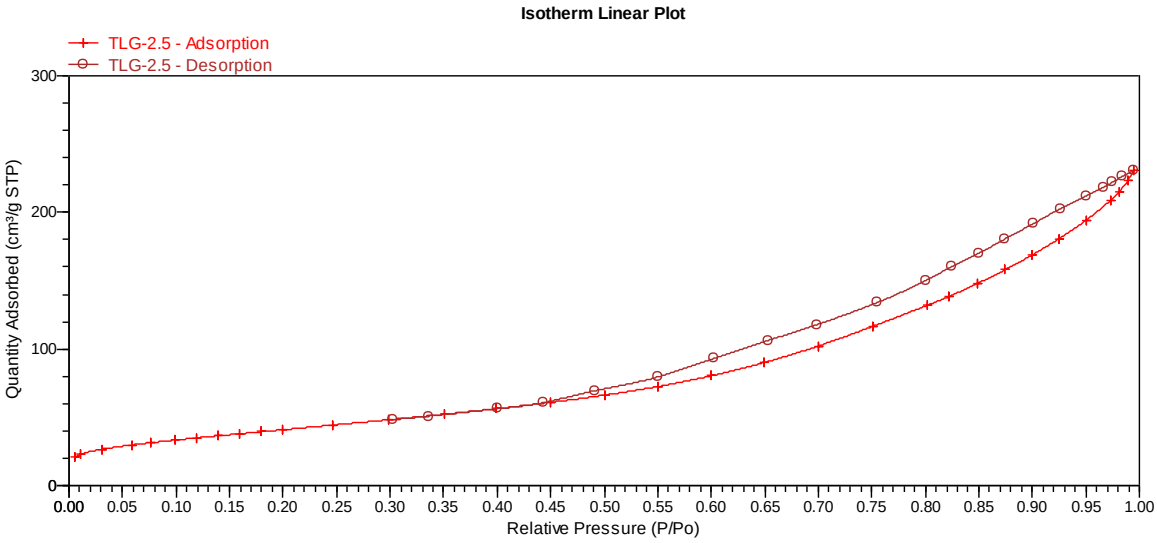

N_2 adsorption isotherm of TL-G-2.50 sample

Appendix II

Calibration Curve

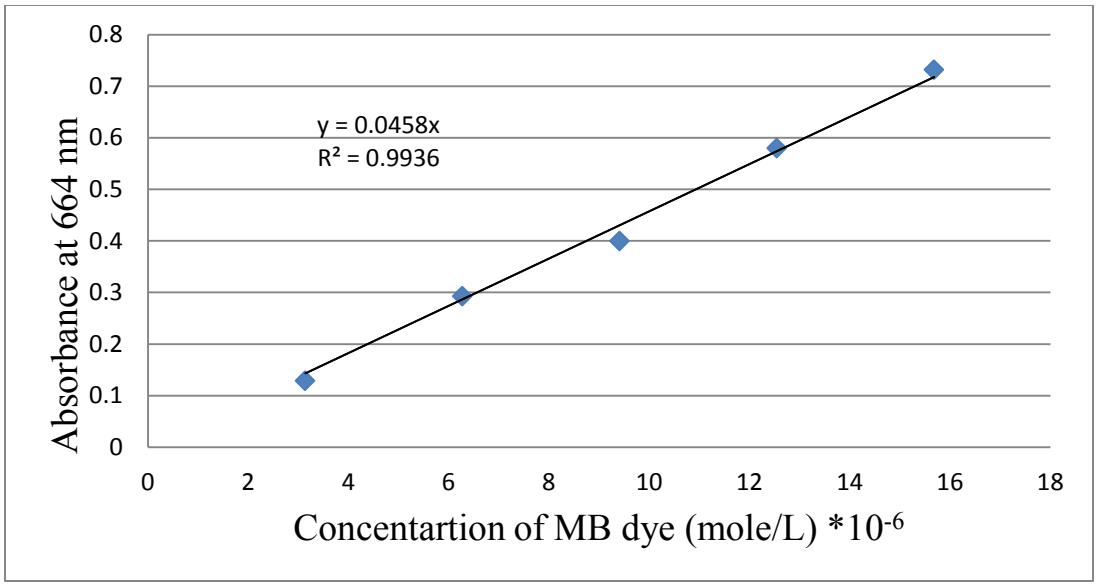

MB calibration curve